Ptychography Coherent Diffractive Imaging Systems for Extreme Ultraviolet and X-ray Sources

by

Charles Schrepferman Bevis

B.A., University of Colorado at Boulder, 2011

M.S., University of Colorado at Boulder, 2017

A thesis submitted to the

Faculty of the Graduate School of the

University of Colorado in partial fulfillment

of the requirements for the degree of

Doctor of Philosophy

Department of Physics

2020

Committee Members:

Margaret Murnane, Chair

Henry Kapteyn

Rafael Piestun

Sadegh Yazdi

Mathias Weber

Bevis, Charles Schrepferman (Ph.D., Physics)

Ptychography Coherent Diffractive Imaging Systems for Extreme Ultraviolet and X-ray Sources

Thesis directed by Prof. Margaret Murnane

Ptychography coherent diffractive imaging is a rapidly developing method for microscopic imaging with coherent X-ray and extreme ultraviolet sources. The technique, which shifts the role of image formation from a physical optic to a computational algorithm, provides a route toward photon efficient imaging systems with diffraction-limited resolution. When combined with high-energy coherent light sources, a microscope capable of probing the nanoworld with exquisite elemental and chemical sensitivity is realized. However, these systems come with concessions such as the large data volume required to form an image, long data acquisition times, and relatively complex image reconstruction methods.

This thesis focuses on the development and extension of ptychography coherent diffractive imaging to higher throughput modalities. This is demonstrated with the formulation of the multiple beam ptychography method that uses several beams to simultaneously probe different parts of a sample. This is first shown with beams of different wavelengths and later with different polarization states. The technique is then extended for beams with identical wavelengths and polarizations by controlling the aliasing of the measured signal.

Finally, an X-ray spectromicroscopy study of a highly heterogeneous meteoric grain is discussed. Ptychography coherent diffractive imaging is combined with scanning transmission X-ray microscopy and X-ray absorption spectroscopy to reveal the meteorite's mineralogical properties through chemical, elemental, and textural identification with a resolution more than an order of magnitude lower than previous similar studies.

Dedication

For my mom. I love ya mumzy, and I miss you every day.

Acknowledgements

My time at JILA and CU has given me the opportunity to collaborate with some of the brightest, kindest, and genuine people I've met in my life. None of which would be possible without my advisors Profs. Margaret Murnane and Henry Kapteyn. They gave me the support and advise to shape my scientific development over the past five years and the open and encouraging environment of their research group has been a wonderful place to develop my skills as a researcher and scientist. I have to thank the KM group, past and present, for all of the support, interesting insight, and spontaneous coffee breaks over the years. I'd like to thank the KM Imaging Team in no particular order: Elisabeth Shanblatt, Dennis Gardner, Daniel Adams, Giulia Mancini, Michael Tanksalvala, Robert Karl, Yuka Esashi, Bin Wang, Nicholas Jenkins, Peter Johnson, Christina Porter, Guan Gui, Zhe "Joe" Zhang, Chen-Ting Liao, Emma-Elizabeth Cating-Subramanian, Michael Gerrity, and Michael Hemmer. This thesis would not have happened without their collective mentoring, collaboration, laughs, hard work, and late nights in the depths of B1B19. There are too many to thank, but I want to mention Joshua Knobloch, Travis Frazer, Begoña Abad, Christian Gentry, Nathan Brooks, and Quynh Nguyen for the interesting conversations, collaborations, and friendships. Thanks to my collaborators Mike Lo, Arjun Rana, and John Miao at UCLA for their fruitful collaborations at the COSMIC beamline. The STROBE center has given me access to so many different opportunities I wouldn't have looked for and really strengthened my belief in the necessity and power of interdisciplinary collaboration. Thanks to Lauren Mason, Ellen Keister, Sarah Schreiner, and Tess Eidem for making them happen. Thank you to the NSF for their support through the Graduate Research Fellowship Program. Finally, thank you to my friends and family for the love and support. This PhD. thing was hard, and I couldn't have done it without all the encouragement to see it through to the end.

Contents

Chapter

Figures

Figure

Chapter 1

Introduction

The past decade has seen tremendous progress in the field of nanoscale imaging. While electron and atomic force microscopy continue to provide unprecedented resolution on the atomic scale, the short wavelengths and high brightness of coherent X-ray and extreme ultraviolet light sources make them an ideal probe for the nanoworld. With increased penetration depths and less stringent sample preparation requirements, X-ray and EUV imaging offers exquisite elemental and chemical contrast while probing a wide range of systems with length scales from of one to one hundred nanometers. Recent advances in coherent diffractive imaging (CDI) have enabled diffraction-limit resolution microscopy systems free of aberrations due to costly and lossy X-ray optics. This thesis focuses on the development of new imaging modalities for CDI systems, in particular the throughput and performance of ptychography CDI is investigated and improved.

This thesis is organized as follow. The remainder of chapter 6.1 provides a background and review of important concepts in EUV and X-ray CDI. Chapter 2 details the coherent, high energy light sources used in this thesis. Chapter 3 provides an introduction to the concepts and algorithms of CDI, ending with a discussion of ptychography CDI. In chapter 4, multiple mode ptychography is discussed, along with an extension to multiple beam ptychography. Chapter 5 offers an extension to multiple beam ptychography that permits large field of view imaging with identical probes. In chapter 6 work done on a newly commissioned X-ray microscopy beam line at the Advanced Light Source is discussed, where X-ray microscopy is used to infer the mineral composition of an Allende meteorite fragment with unprecedented resolution. This thesis concludes with chapter 7 with a

summary of ongoing and future work.

1.1 Introduction to Imaging with High Energy Light

1.1.1 Development of Microscopy

When thinking of a microscope, an image of a compound microscope commonly appears in one's head. In this configuration, the objective is used to magnify an image of the original object and the eyepiece is used by the observer to view the magnified image. Though the principles of magnification were known to the ancient Greeks, it would take more than sixteen hundred years before these ideas were organized into useful imaging systems such as the telescope and microscope [1][1] .

It was Robert Hooke who published the first scientific treatise on the subject of microscopy in 1665, *Micrographia*. Here, using both a single lens and compound microscope, Hooke described a study of the microscopic world, including several revolutionary scientific findings such as the first observation of a cell and microorganisms [3]. Hooke also offered detailed descriptions and illustrations of his microscopes. In addition, Hooke was the first scientist to suggest that engineering and controlling the light source was as crucial for the quality production of images. Figure 1.1 depicts Hooke's suggested light source paired with his compound microscope.

The desire to view ever smaller systems spurred interest and research into the theory of optics and light-matter interactions. Among the advancements to both the design and understanding of the microscope, came an exploration into the fundamental limits of the performance of such an imaging system.

An important advancement came in 1873 when Ernst Abbe formulated the diffraction limit of light, which placed a lower limit on the resolving power of a microscope at one half the illuminating wavelength [4]. Abbe's resolution criteria states that objects smaller than ∼200 nm cannot be resolved using conventional visible light-based imaging system.

[1] Contrary to popular belief, Galileo Galilei did not invent the telescope, but rather he created his first design based on a description he heard regarding a similar system built by a Dutch spectacle-maker [2].

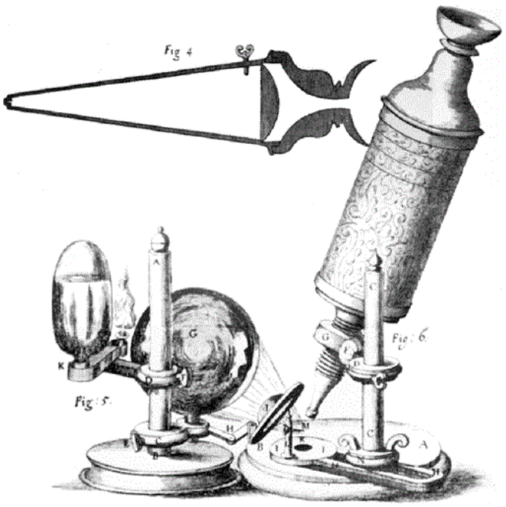

Figure 1.1: **Robert Hooke's Compound Microscope**. A detailed drawing of Robert Hooke's compound microscope with an artificial light source. This design allowed for ideal viewing conditions of the specimen regardless of ambient light. The drawing is from [3].

The drive to beat the diffraction limit has spawned a variety of super-resolution imaging techniques including evanescent near-field imaging [5], well controlled fluorophores in fluorescent microscopy [6, 7], and mulitphoton excitation techniques [8]. A brute-force method to lowering the resolution limit is to simply scale the wavelength of the illumination by a desired factor – much easier said than done. The imaging system with the highest resolving power to date is the electron microscope, which uses this philosophy.

These microscopes use electrons as an illumination source with de Broglie wavelengths $\lambda = h/p$, where h is Plank's constant and p is the electron's momentum [9]. The wavelength of these electrons are typically picometers and theoretically allows for picometer-scale imaging. In practice, this is usually reduced to Ångström levels due to aberrations in the electron imaging system [10].

1.1.2 X-ray and EUV Light

An important discovery in the field of light science came in 1893, when Wilhelm Róntgen discovered X-ray light. Róntgen noted that when accelerated electrons struck a thick target, they subsequently emitted rays that were invisible to the eye, but with a fluorescent screen, shadowgrams

of objects placed in their path could be recorded [11]. These "X-rays", as Róntgen called them, were high energy electromagnetic radiation produced by bremsstrahlung caused by the deceleration of electrons hitting a thick target [12].

The medical applications of these rays was almost immediately realized [13], with the application to material science and crystallography following in the next half-century [14–16]. The next revolution in X-ray light came in the late 1940's when the synchrotron light source was created. These sources use a finer control of the electron's acceleration to produce bright, high energy photons that can be made coherent through filtering [17].

In 1987, a third revolution in X-ray generation began with the discover and development of high harmonic generation light sources [18]. In the last 30 years, high harmonic generation has matured into an almost turn-key solution for a laboratory scale, high energy, coherent light source. This technique uses an extremely nonlinear process to up convert light of some driving frequency to a high order harmonic and is capable of producing bright, coherent flux at extreme ultraviolet (EUV) and X-ray wavelengths when properly phase matched [19–22].

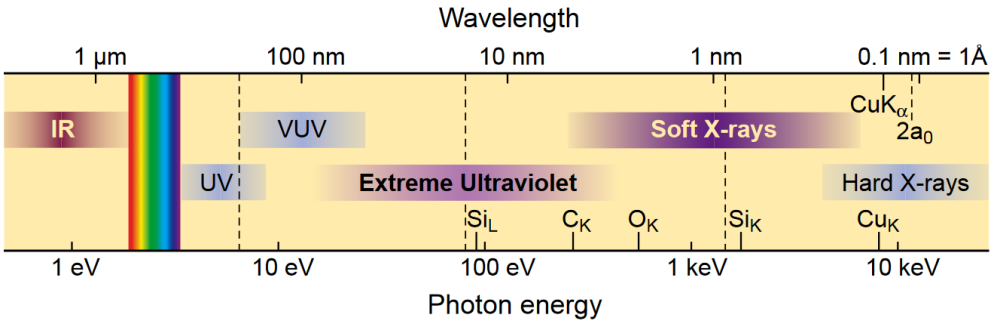

Figure 1.2: **The Electromagnetic Spectrum**. The spectrum ranges from the infrared (IR), visible, ultraviolet, extreme ultraviolet (EUV), soft X-ray, and hard X-ray. Adapted from [23].

Like all electromagnetic radiation, EUV and X-ray light is characterized by its wavelength (λ), or equivalently its wavenumber ($k = 2\pi/\lambda$), frequency ($f = c/\lambda$), or photon energy ($\hbar\omega$, with $\omega = 2\pi f$). The exact feature that is used to describe is light depends on the area of study and which feature is most directly related to the sample under investigation. For example, in imaging,

wavelength is often used as it provides an approximate reference for the physical length scale of the sample or performance of the system. For spectroscopic studies, it is more common to refer to the photon energy, where a particular energy structure of a sample may be of interest. EUV light contains light with wavelength from about 100 nm - 10 nm, with soft X-rays following with wavelengths from approximately 10 nm - 1 Å. The distinction between "hard" and "soft" X-rays is made to denote wavelengths that can and cannot penetrate air [14].

According to Abbe's resolution criteria, EUV and soft X-ray light should be able to natively study nanoscale systems if used as the source of a microscopy system. In addition, this region of the spectrum contains K and L absorption features of many elements, giving elemental and chemical contrast not present at other spectral regions [23].

1.1.3 X-ray and EUV Microscopy

This field of study is the marriage of scientific advancements outlined in the previous two sections. The shorter wavelength offers a lower resolution limit in these microscopes. Furthermore, the long penetration depth and lower energy of these microscopes is suitable for a wider array of sample sizes and requires less stringent sample preparation methods compared to electron microscopy. In order to exploit these properties for high resolution imaging, a method to manipulate the light source is needed. Unfortunately, conventional lenses cannot be fabricated for EUV and X-ray light. Luckily, there are refractive, reflective, and diffractive solutions to focus and form images with high energy light.

Refractive optics such as the compound refractive lens (Fig. 1.3(a)) have direct parallels to refractive lenses for visible light. Instead of a single lens, the compound lens consists of many discrete lenses which all impart a small deflection to the incident beam [25, 26]. These optics have proven effective for focusing high energy X-rays that are not strongly absorbed, but are still challenging to use with EUV and soft X-ray light.

A Fresnel zone plate (Fig. 1.3(b)) is a popular choice in X-ray microscopy and acts as a diffraction-based analogue to a refractive lens. These elements work by carefully designing the

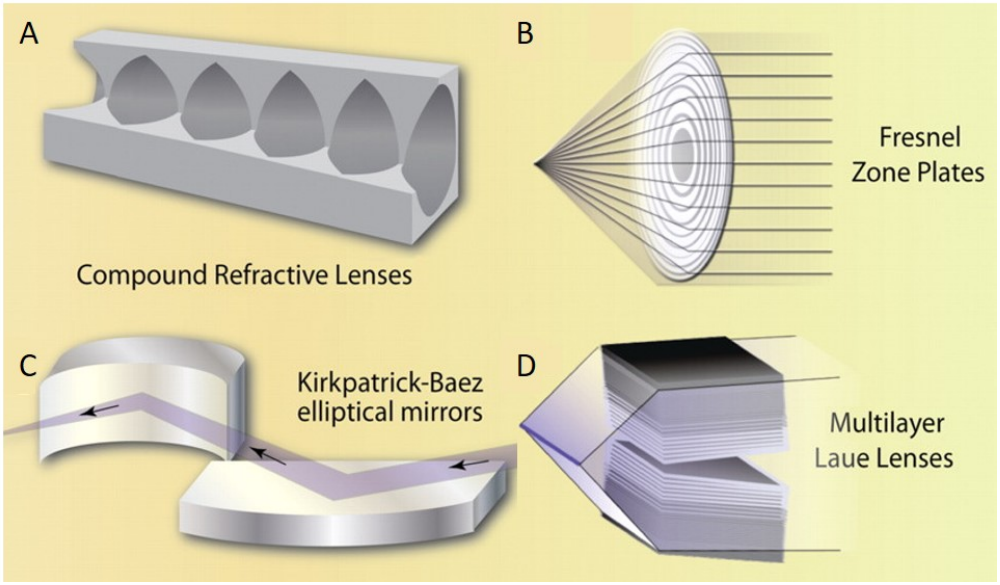

Figure 1.3: **Focusing Techniques for X-ray Light**. (a) A compound lens consists of many small, discrete lenses in series, each providing a small deflection to the incident light. (b) The Fresnel zone plate is a diffractive optical element that focuses light by carefully controlling the interference of the transmitted beam. (c) Kirkpatrick-Baez mirrors are two curved mirrors set at 90° relative to each other. Light is focused in each direction by bouncing of each mirror. They are used in a glancing incidence geometry to maintain high efficiency. (d) The Laue lens is the one dimensional analogue to the Fresnel zone plate. This vertically symmetric geometry allows for higher manufacturing tolerances and therefore tighter focusing. Adapted from [24].

structure of the optic such that transmitted X-rays constructively interfere at only one location, effectively focusing the beam [27]. This is done through patterning alternating regions of transparent and opaque concentric rings, which selectively block light that would destructively interfere at the focal point. Though easy to align and compact, their resolution is limited by the fabrication quality of the outer-most zone. This presents a difficult manufacturing problem for high resolution imaging systems, where resolutions less than 30 nm are needed. Nonetheless, high quality zone plates can be used for X-ray microscopy systems [28].

The Laue lens can be thought of as a one dimensional zone plate (Fig. 1.3(d)) and is the diffractive analogue of a cylindrical lens [29]. The Laue lens was created to circumvent the fabrication challenges associated with zone plate. By moving to a vertically symmetric geometry, the lens can be made via sputtering methods, allowing for finer layer thickness and therefore a

tighter focus [30]. Two Laue lenses can be used in succession to create a uniform, tight focal spot.

Reflective optical elements, such as the Kirpatrick-Baez mirrors (Fig 1.3(c)) are among the oldest solutions for manipulating X-ray light. The system consists of two parabolic or elliptical mirrors oriented 90° with respect to each other. X-rays are directed onto the mirrors at a glancing incidence to maintain high reflectivity, and independently focused in each direction. This configuration has been used for imaging, but resolution is limited due to aberrations [31].

These elements or a combination there of are used to build different types of X-ray microscopy systems. For example, a zone plate can be used in place of a lens to build a conventional imaging system for X-ray sources, so long as the source is coherent. This type of microscope forms a direct image on a detector. On the other hand, some of these optics are designed to only focusing light. These optics are still useful for imaging, when operating in a point-scanning modality. Scanning transmission X-ray microscopy (STXM) is one such method where a beam is tightly focused and scanned across the sample, building up an image point-by-point [32, 33]. Though these X-ray microscope designs are appropriate for many applications, they are inherently limited by the fabrication quality of these components.

An imaging method that avoids this reliance on optic fabrication quality is coherent diffractive imaging (CDI). This technique transfers the task of image formation from a physical optic to a computational algorithm that solves for what a sample must look like given a measurement of its scatter pattern and additional knowledge about the experimental setup. Because there are no optics between the sample and detector, it is capable a achieving diffraction-limited resolution as well as being the most photon-efficient type of EUV or X-ray imaging [34]. Furthermore, the technique provides both phase and amplitude contrast, allowing for a wide range of sample to be imaged. CDI has matured into a well-developed technology in EUV and X-ray imaging over the last twenty years, taking on many specialized configurations to probe different aspects of a sample, see Fig 1.4. Work is this thesis is focused on expanding these modalities to higher throughput, higher resolution configurations.

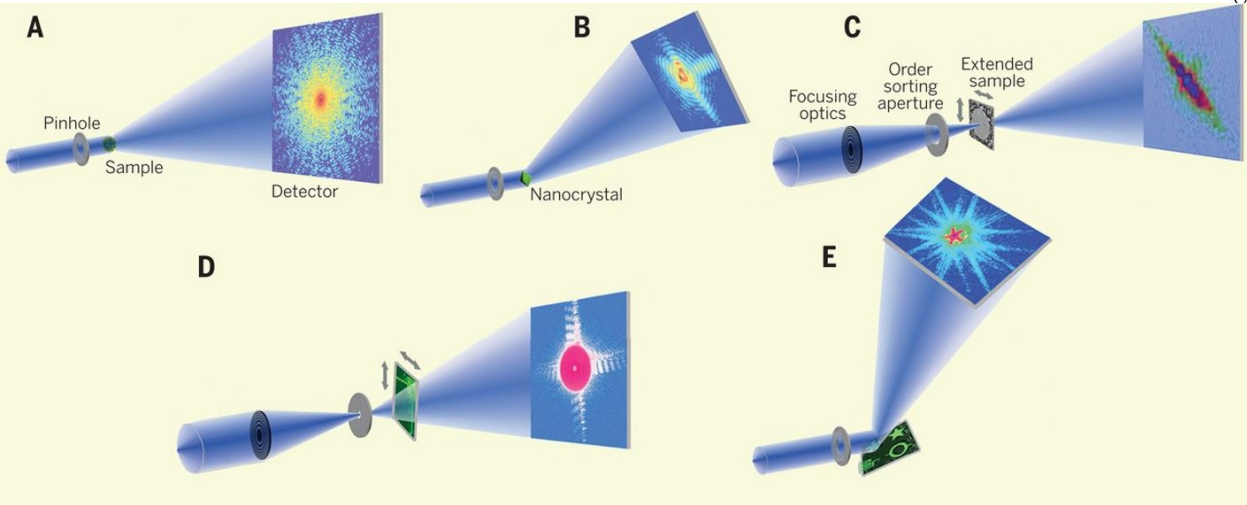

Figure 1.4: **Different CDI Experimental Configurations**. (a) Plane-wave CDI: A coherent plane wave illuminates a sample and the far-field diffraction pattern is measured. (b) Bragg CDI: the diffraction pattern is acquired at the Bragg angle from a nanocrystal. (c) Ptychography CDI: a localized probe is scanned over an extended sample and a series of diffraction patterns are collected from overlapping positions. (d) Fresnel CDI: a sample is positioned slightly out of focus of a coherent probe and the Fresnel diffraction pattern is measured by a detector. (e) Reflection CDI: a coherent probe is reflected off the surface of a sample and the reflected diffraction is measured on a detector. Modified from [35].

1.2 The Physics of Diffraction

To understand the mechanics of CDI, it is important to understand the behavior of light as it propagates through an imaging system. In this case, the imaging system is simply the interaction of an illuminating probe with a sample and propagation of that light through free-space to a detector. This section briefly reviews the theory of of wave propagation and diffraction.

The complete theory of diffraction physics requires an understanding of electromagnetism, quantum mechanics, and field theory. However, for the work discussed in this thesis and the field of CDI, a purely classical treatment based on the wave theory of light will suffice. Emphasis is placed on topics stemming from Fourier optics, a subfield of optics on which much of the physical mathematical modeling of CDI is based. The derivations presented here are largely adapted from [12, 36, 37]. The eager student is directed to these sources for deeper understanding and a more detailed (and perhaps coherent) treatment.

1.2.1 The Wave Equation of Light

As with any good derivation in classical electromagnetism, this one starts with Maxwell's equations. This collection of four relationship between the properties of the electric and magnetic field describe the complete theory of classical electromagnetism. Since light is electromagnetic radiation, insight into its behavior is gleaned by observing and manipulating these relations. Maxwell's four equations are:

$$\text{Gauss's Law: } \nabla \cdot \boldsymbol{D} = \rho \tag{1.1}$$

$$\text{Gauss's Law for Magnetism: } \nabla \cdot \boldsymbol{B} = 0 \tag{1.2}$$

$$\text{Faraday's Law: } \nabla \times \boldsymbol{E} = -\frac{\partial \boldsymbol{B}}{\partial t} \tag{1.3}$$

$$\text{Ampère's Law: } \nabla \times \boldsymbol{H} = \boldsymbol{J} + \frac{\partial \boldsymbol{D}}{\partial t} \tag{1.4}$$

where ∇ is the three dimensional gradient operator, $\boldsymbol{D}$ is the electric displacement, $\boldsymbol{E}$ is the electric field, $\boldsymbol{H}$ is the magnetizing field, $\boldsymbol{B}$ is the magnetic field, ρ is the free charge, and $\boldsymbol{J}$ is the free current. Here, the bold notation $\boldsymbol{E}$ denotes a vector quantity with components $[E_x, E_y, E_z]$.

It is now assumed that the electric and magnetic fields are propagating inside a dielectric medium – more specifically, a linear, isotropic, homogeneous dielectric medium – and that there is no free charge ($\rho = \boldsymbol{J} = 0$) in the region of interest. In linear dielectric materials, a linear dependence exists that relates $\boldsymbol{D}$ to $\boldsymbol{E}$ and $\boldsymbol{B}$ to $\boldsymbol{H}$.

$$\boldsymbol{D} = \epsilon \boldsymbol{E} \tag{1.5}$$

$$\boldsymbol{B} = \mu \boldsymbol{H} \tag{1.6}$$

where ϵ is the permittivity and μ is the permeability of the material.

With the foundations in place, the wave equation is derived by first taking the curl of Eqn. 1.3 (Faraday's Law).

$$\nabla \times \nabla \times \boldsymbol{E} = -\nabla \times \frac{\partial \boldsymbol{B}}{\partial t} \tag{1.7}$$

Recalling the vector identity $\nabla \times \nabla \times \boldsymbol{Q} = \nabla (\nabla \cdot \boldsymbol{Q}) - \nabla^2 \boldsymbol{Q}$, Eqn. 1.7 is rewritten as

$$\nabla (\nabla \cdot \boldsymbol{E}) - \nabla^2 \boldsymbol{E} = -\nabla \times \frac{\partial \boldsymbol{B}}{\partial t}. \tag{1.8}$$

Using Eqn. 1.1 (Gauss's Law) and rearranging the time derivative on curl operators on the right hand side gives

$$\nabla^2 \boldsymbol{E} = \frac{\partial (\nabla \times \boldsymbol{B})}{\partial t}. \tag{1.9}$$

Finally, an application of Eqn.: 1.4 (Ampère's Law) rewritten in terms of $\boldsymbol{E}$ and $\boldsymbol{B}$ using Eqns. 1.5 and 1.6 gives the relation

$$\nabla^2 \boldsymbol{E} = \mu\epsilon \frac{\partial^2 \boldsymbol{E}}{\partial t^2}. \tag{1.10}$$

Drawing from outside knowledge, a few strategic definitions are introduced. The refractive index of the medium is defined as

$$n = \sqrt{\frac{\mu\epsilon}{\mu_0 \epsilon_0}}, \tag{1.11}$$

with μ_0, ϵ_0 the vacuum permeability and permittivity, respectively. Furthermore, the speed of light in vacuum is defined as

$$c = \frac{1}{\sqrt{\mu_0 \epsilon_0}} = 299\ 792\ 458 \text{ m/s}. \tag{1.12}$$

Using these definitions, the wave equation for electromagnetism is written in the familiar form

$$\nabla^2 \boldsymbol{E} = \frac{n^2}{c^2} \frac{\partial^2 \boldsymbol{E}}{\partial t^2}, \tag{1.13}$$

where c/n is interpreted as the speed of wave propagation within the dielectric medium.

An nearly identical derivation for the wave equation for magnetism is carried out by taking the curl of Eqn. 1.4 and following similar steps. Work done in this thesis follows from application, approximations, and manipulations of Eqn. 1.13.

1.2.2 The Helmholtz Equation

Eqn. 1.13 is simplified by the application of a separable ansatz. In this case, the assertion is made that the wave equation is separable in space $\boldsymbol{r} = [x, y, z]$ and time (t). Beginning with a

monochromatic solution, it is assumed the solution can be written as

$$\boldsymbol{E}(\boldsymbol{r},t) = \boldsymbol{E}(\boldsymbol{r})e^{-i(\omega t+\phi)}, \tag{1.14}$$

where ω is the frequency of the wave, and ϕ is some time independent, constant phase offset. Dropping this into 1.13 gives

$$\nabla^2\boldsymbol{E}(\boldsymbol{r})e^{-i(\omega t+\phi)} = -\frac{n^2\omega^2}{c^2}\boldsymbol{E}(\boldsymbol{r})e^{-i(\omega t+\phi)}. \tag{1.15}$$

Canceling the common factor gives the familiar formulation of the Helmholtz equation

$$\nabla^2\boldsymbol{E}(\boldsymbol{r}) + n^2k^2\boldsymbol{E}(\boldsymbol{r}) = 0, \tag{1.16}$$

with the wave number $k \equiv \omega/c$. Furthermore, the periodicity of the phase element in Eqn. **??** implies a temporal oscillation period of $T = 2\pi/\omega$ and it follows that the spatial distance of one oscillation defines a wavelength $\lambda = 2\pi/k$.

Given the symmetry and separability of Eqn. 1.16, this vector equation is separable into distinct scalar equations over each component of $\boldsymbol{E}(\boldsymbol{r})$, providing a relation that describes the spatial evolution of a monochromatic stationary field through a homogeneous medium. For a polychromatic wave, a solution is obtained by spectrally decomposing into monochromatic components

$$\boldsymbol{E}(\boldsymbol{r},t) = \frac{1}{\sqrt{2\pi}}\int_0^\infty \boldsymbol{E}_\omega(\boldsymbol{r})e^{-i\omega t}d\omega \tag{1.17}$$

where $\boldsymbol{E}_\omega(\boldsymbol{r})$ is the spatial component of pure wave with a single frequency ω.

1.2.3 Angular Spectrum Solution to the Helmholtz Equation

The standard and most sought after solution in the field of diffraction is the calculation of a field at some arbitrary point is space, given a the field distribution at some other known location. This is a colloquial definition of a "propagation" problem. Typically, this problem is formulated as a boundary-value problem for Eqn. 1.16. The problem is usually set up by assuming that sources of radiation exist in some lower half space $z < 0$ and the spatial distribution of some monochromatic

field $\varphi_\omega(\boldsymbol{r})$ is known at $z = 0$. Given this, find the spatial distribution $\varphi_\omega(\boldsymbol{r})$ anywhere in the upper half space $z > 0$.

A practical first approach is to search for potential solutions on planes with $z = \delta z > 0$, where any solution is a propagated field from the known distribution at the boundary $z = 0$. In this formulation, the coordinate system is selected such that the direction of propagation is along the z-axis, $\hat{z}$, often aligned with the direction of the optical axis.

The solution to this problem is usually found through the Kirchhoff or Rayleigh-Sommerfeld diffraction integrals. This treatment is formulated to produce the the field $\varphi_\omega(\boldsymbol{r}_{p_0})$ at a point p_0 in the upper half space, $z > 0$, given the field on a surface S – and its normal derivative in the case of the Kirchhoff formulation – enclosing p_0. With an application of Green's Theorem and an appropriate choice of Green's function, these integrals are produce a relation between the field at planes with $z > 0$ to the field at the boundary plane, $z = 0$. A different approach is considered here where a solution is found by considering the lateral Fourier decomposition of the wave.

Before beginning this derivation, it is convenient to examine a very general solution to the Helmholtz equation, a time-independent plane wave

$$p(\boldsymbol{r}) = e^{i\boldsymbol{k}\cdot\boldsymbol{r}}, \tag{1.18}$$

with $\boldsymbol{k} = \frac{2\pi}{\lambda}[f_x, f_y, f_z]$. The components f_α are spatial frequencies, a normalized version of the wave number commonly used in imaging science with $f = k/2\pi = 1/\lambda$. The components of the wave vector $\boldsymbol{k}$ define the direction of propagation, with the components interrelated through

$$f_z = \frac{1}{\lambda}\sqrt{1 - (f_x)^2 - (f_y)^2}. \tag{1.19}$$

With these relations, in a fixed plane at $z = 0$, a complex exponential $\exp[i2\pi(f_x x + f_y y)]$ is interpreted as a plane wave who's propagation direction in completely defined using Eqn.: 1.19.

Consider now the typical propagation problem, where a solution to Eqn. 1.16, $\psi(x, y; 0)$, is given at the plane $z = 0$. From this, the field at some other plane $\psi(x, y; z_1)$ is sought. The field $\psi(x, y; z)$ can be spectrally decomposed in the lateral dimensions $\boldsymbol{x} = [x, y]$, where the field and

decomposition are related via a Fourier transform

$$\psi(x,y;z) = \frac{1}{2\pi}\int \tilde{\psi}(f_x,f_y;z)e^{i2\pi(f_x x+f_y y)}df_x df_y, \tag{1.20}$$

where $\tilde{\psi}(f_x,f_y;z)$ is the two dimensional Fourier transform of $\psi(x,y;z)$ over the lateral dimensions (x,y). A notational convention is also introduced here. When considering the field in a fixed (x,y) plane, z is constant and is separated by a semicolon from other variables.

Inserting Eqn. 1.20 into Eqn. 1.16 gives the expression

$$\frac{1}{2\pi}\int \partial_z^2\tilde{\psi}(f_x,f_y;z) + \left(\frac{2\pi n}{\lambda}\right)^2\left[1-\lambda^2(f_x^2+f_y^2)\right]\tilde{\psi}(f_x,f_y;z)df_x df_y = 0. \tag{1.21}$$

For this integral to be zero for all functions, the integrand must vanish. So the above expression is equivalent to the differential equation

$$\partial_z^2\tilde{\psi}(f_x,f_y;z) = -\left(\frac{2\pi n}{\lambda}\right)^2\left[1-\lambda^2(f_x^2+f_y^2)\right]\tilde{\psi}(f_x,f_y;z). \tag{1.22}$$

The simple solution to Eqn. 1.22 is

$$\tilde{\psi}(f_x,f_y;z) = \tilde{\psi}(f_x,f_y;0)e^{\frac{i2\pi n}{\lambda}\sqrt{1-\lambda^2(f_x^2+f_y^2)}z}. \tag{1.23}$$

There are two different cases of this solution to consider. If $\lambda^2(f_x^2+f_y^2) > 1$ the argument under the square root becomes complex and the exponential term in Eqn. 1.23 becomes real and decays to zero within a distance of a few wavelengths. This solution is known as an evanescent wave and must only be considered for propagation on the length scale of the wavelength. For $\lambda^2(f_x^2+f_y^2) < 1$ the exponential oscillates and the effect of propagation over some z distance is understood as a change of relative phases of the components of the lateral spectral decomposition. Since each plane wave component propagates at a different angle, each travels a different distance between the two planes, which results in relative phase delays. Each component is a plane wave propagating in a unique angular direction defined by $\boldsymbol{k}$ so the lateral decomposition in Eqn. 1.20 is often referred to as the *angular spectrum*. Inserting Eqn. 1.23 into Eqn. 1.20 gives

$$\psi(x,y;z) = \frac{1}{2\pi}\int \tilde{\psi}(f_x,f_y;0)e^{\frac{i2\pi n}{\lambda}\sqrt{1-\lambda^2(f_x^2+f_y^2)}z}e^{i2\pi(f_x x+f_y y)}df_x df_y, \tag{1.24}$$

which provides the field $\psi(x, y; z)$ given the angular spectrum of the field in some other plane $\tilde{\psi}(f_x, f_y; 0)$. It should be noted that Eqn. 1.24 describes a relative relation. Meaning once the field is know in some plane z_0, it can be calculated in any other plane z_1 by finding the relative distance $\Delta z = z_1 - z_0$. For practical and implementation purposes, this relation is often written to relate a field at two different z-planes using Fourier transforms

$$\psi(x, y; z_1) = \mathcal{F}_\perp^{-1} \left\{ \mathcal{F}_\perp \left\{ \psi(x, y; z_0) \right\} \mathcal{H}(f_x, f_y; \Delta z) \right\}, \tag{1.25}$$

with $\mathcal{F}_\perp$ and $\mathcal{F}_\perp^{-1}$ representing the forward and inverse Fourier transform over the lateral dimensions (x, y) and (f_x, f_y), respectively, and where

$$\mathcal{H}(f_x, f_y; \Delta z) = e^{\frac{i2\pi n}{\lambda}\sqrt{1-\lambda^2(f_x^2+f_y^2)}\Delta z}. \tag{1.26}$$

The quantity $\mathcal{H}$ is referred to as the "free space transfer function" or "free space propagator", but is equally valid in homogeneous media with constant n.

1.2.4 The Fresnel Approximation

While Eqn. 1.25 provides an exact solution to the propagation of a general monochromatic electric field between two parallel planes, there are situations where approximations can be leveraged to simplify the relation. Because of the wavelengths and experimental geometries commonly used in CDI systems, the Fresnel – or sometimes the paraxial or small-angle – approximation is often valid. In this regime, it is assumed that the lateral extent of the field at plane $z = z_0$ and the diffraction pattern in plane $z = z_1$ are small compared to $\Delta z = z_1 - z_0$. Or in terms of spatial frequencies, $(f_x^2 + f_y^2) \ll 1/\lambda^2$.

In this situation, the propagating plane waves in the angular spectrum are restricted to those that move at small angles relative to the optical axis. If this condition is met, then a binomial approximation can be made in the exponential in Eqn. 1.26

$$\sqrt{1 - \lambda^2(f_x^2 + f_y^2)} \approx 1 - \frac{\lambda^2}{2}\left(f_x^2 + f_y^2\right). \tag{1.27}$$

Substituting the expansion into the free space propagator then gives

$$\begin{aligned}\mathcal{H}(f_x, f_y; \Delta z) &\approx e^{\frac{i2\pi n\Delta z}{\lambda}\left(1-\frac{\lambda^2}{2}\left(f_x^2+f_y^2\right)\right)} \\ &\approx e^{\frac{i2\pi n\Delta z}{\lambda}} e^{-i\pi n\lambda\Delta z\left(f_x^2+f_y^2\right)}.\end{aligned}$$

It is seen above that within the Fresnel approximation, the spatial phase dispersion is approximated as a quadratic phase dispersion. The propagated field under the Fresnel approximation is then

$$\psi(x, y; z_1) = e^{\frac{i2\pi n\Delta z}{\lambda}} \mathcal{F}_\perp^{-1}\left\{\mathcal{F}_\perp\left\{\psi(x, y; z_0)\right\} e^{-i\pi n\lambda\Delta z\left(f_x^2+f_y^2\right)}\right\}. \tag{1.28}$$

Fresnel propagation can be reformulated into an expression that only requires a single Fourier transform. To see this, the convolution theorem is applied to Eqn. 1.28

$$\begin{aligned}\psi(x, y; z_1) &= e^{\frac{i2\pi n\Delta z}{\lambda}} \mathcal{F}_\perp^{-1}\left\{\mathcal{F}_\perp\left\{\psi(x, y; z_0)\right\} \mathcal{F}_\perp\left\{\mathcal{F}_\perp^{-1}\left\{e^{-i\pi n\lambda\Delta z\left(f_x^2+f_y^2\right)}\right\}\right\}\right\}. \\ &= \psi(x, y; z_0) \otimes \mathcal{D}(x, y; \Delta z)),\end{aligned} \tag{1.29}$$

with the Fresnel propagation operator

$$\mathcal{D}(x, y; \Delta z)) = e^{\frac{i2\pi n\Delta z}{\lambda}} \mathcal{F}_\perp^{-1}\left\{e^{-i\pi n\lambda\Delta z\left(f_x^2+f_y^2\right)}\right\}. \tag{1.30}$$

Considering the limiting form of the Fresnel integrals gives an explicit form of $\mathcal{D}(x, y; \Delta z)$ [38]:

$$\mathcal{D}(x, y; \Delta z) = \frac{1}{i\lambda\Delta z} e^{\frac{i2\pi n\Delta z}{\lambda}} e^{\frac{-i\pi n}{\lambda\Delta z}\left(x^2+y^2\right)}. \tag{1.31}$$

Looking now at the explicit form of the convolution integral in Eqn. 1.29

$$\psi(x, y; z_1) = \frac{e^{\frac{i2\pi n\Delta z}{\lambda}}}{i\lambda\Delta z} \iint \psi(\xi, \eta; z_0) e^{\frac{-i\pi n}{\lambda\Delta z}\left((x-\xi)^2+(y-\eta)^2\right)} d\xi d\eta. \tag{1.32}$$

Expanding the last exponential inside the integrand and partially factoring it outside the integral gives

$$\psi(x, y; z_1) = \frac{e^{\frac{i2\pi n\Delta z}{\lambda}}}{i\lambda\Delta z} e^{\frac{i\pi n}{\lambda\Delta z}(x^2+y^2)} \iint \left[\psi(\xi, \eta; z_0) e^{\frac{i\pi n}{\lambda\Delta z}(\xi^2+\eta^2)}\right] e^{\frac{-i2\pi n}{\lambda\Delta z}(x\xi+y\eta)} d\xi d\eta. \tag{1.33}$$

Aside from multiplicative factors, the above expression is recognized as a Fourier transform of the field at $z = z_0$ multiplied by a quadratic phase factor. Written in terms of the Fourier transform operator

$$\psi(x, y; z_1) = \frac{e^{\frac{i2\pi n\Delta z}{\lambda}}}{i\lambda\Delta z} e^{\frac{i\pi n}{\lambda\Delta z}(x^2+y^2)} \mathcal{F}\left\{\psi(\xi, \eta; z_0) e^{\frac{i\pi n}{\lambda\Delta z}(\xi^2+\eta^2)}\right\}, \tag{1.34}$$

where the Fourier transform has conjugate variables (ξ, η) and $(\frac{x}{\lambda \Delta z}, \frac{y}{\lambda \Delta z})$. For the work detailed in this thesis, Eqn. 1.34 is used for the propagation of light. Though Eqn. 1.28 and 1.34 are analytically equivalent, they present different advantages when implemented numerically. Specifically, Eqn. 1.28 is better suited for small propagation distances Δz, while Eqn. 1.34 is better suited for larger distances. The reason for this is that small Δz in Eqn. 1.34 results in a steep phase curvature in the parabolic phase term, which becomes difficult to adequately sample while being computationally tractable. And similarly for Eqn. 1.28 and large Δz.

1.2.5 The Fraunhofer Approximation

A final useful approximation when considering wave propagation is the Fraunhofer – or far-field – approximation. In this limit the field propagation expression has yet another simplification, reducing propagation to a single Fourier transform. When the propagation distance Δz becomes very large relative to the aperture size

$$\Delta z \gg \frac{\pi(\xi^2 + \eta^2)_{max}}{\lambda}, \tag{1.35}$$

then the quadratic phase can be ignored and Eqn. 1.34 reduces to

$$\psi(x, y; z_1) = \frac{e^{\frac{i2\pi\Delta z}{\lambda}}}{i\lambda\Delta z} e^{\frac{i\pi}{\lambda\Delta z}(x^2+y^2)} \mathcal{F}\left\{\psi(\xi, \eta; z_0)\right\}. \tag{1.36}$$

Up to multiplicative phase factors, the far-field diffraction pattern is simply the Fourier transform of a field evaluated at frequencies

$$\begin{aligned} f_x &= x/\lambda\Delta z \\ f_y &= y/\lambda\Delta z. \end{aligned} \tag{1.37}$$

When numerically implementing this propagation, care must be taken to correctly setup and spatial and frequency grids in each plane. Fortunately the resolution and maximum extend of the grids are related through the usual Fourier conjugate relation such that if the grid at z_0 is known, then the grids at z_1 are easily computed. Defining the grid spacing $d\xi$ in plane z_0 and maximal extent ξ_{max}, then the frequency element resolution and grid extent is simply $df = 1/\xi_{max}$ and $f_{max} = 1/d\xi$, respectively. Thus, a straightforward procedure to convert from $\xi \to f \to x$.

1.2.6 The Fresnel Number and the Validity of Propagation Approximations

There are several different ways to treat wave propagation depending on system geometry. The question remains how to determine which regime is appropriate for a given situation. One convenient method is the dimensionless quantity Fresnel Number

$$F_N = \frac{a^2}{\lambda \Delta z}, \tag{1.38}$$

where a is a characteristic size such as aperture diameter in the initial field at $z = z_0$. With this criteria, three different regimes are defined:

$$\begin{aligned} &F_N \ll 1\text{: Fraunhofer Regime} \\ &F_N \sim 1\text{: Fresnel Regime} \\ &F_N \gg 1\text{: Spectrum of Plane Waves Propagation.} \end{aligned} \tag{1.39}$$

With this as a broad guide, the value of F_N can be used as a general guide to determine which method is appropriate for propagation.

1.2.7 The Born Approximation

The theory of diffraction is formulated here using the language of scattering physics. A monochromatic light field scattered by an object is considered, and the scattering event is assumed to be elastic – meaning the frequency of the incident light ω is assumed to be unchanged during the scattering process. This derivation is largely derived from [37, 39]. To begin, the Helmholtz equation is written with explicit spatial dependence with $n \to n(\boldsymbol{r})$,

$$\nabla^2 \psi(\boldsymbol{r}) + n^2(\boldsymbol{r}) k^2 \psi(\boldsymbol{r}) = 0. \tag{1.40}$$

This is rewritten as an inhomogeneous equation

$$\nabla^2 \psi(\boldsymbol{r}) + k^2 \psi(\boldsymbol{r}) = -k^2 (n^2(\boldsymbol{r}) - 1) \psi(\boldsymbol{r}). \tag{1.41}$$

The scattering potential $f(\boldsymbol{r})$ is now introduced and is defined as $f(\boldsymbol{r}) = k^2(n^2(\boldsymbol{r}) - 1)$. An important assumption of this method is that there is a single scattering event caused by a single

scattering potential. An ansatz for the solution is made where the field at all locations is written as the sum of the incident wave $\psi_i(\boldsymbol{r})$ and the scattered wave $\psi_s(\boldsymbol{r})$,

$$\psi(\boldsymbol{r}) = \psi_i(\boldsymbol{r}) + \psi_s(\boldsymbol{r}). \tag{1.42}$$

Inserting this into Eqn. 1.41 yields

$$\left[\nabla^2 + k^2\right] \psi_s(\boldsymbol{r}) = -f(\boldsymbol{r})\psi(\boldsymbol{r}), \tag{1.43}$$

where the fact that $\psi_i(\boldsymbol{r})$ satisfies the homogeneous Helmholtz equation is used.

Solving this is relation requires the use of Green's functions and Green's first theorem [12]. A Green's function, denoted as $G(\boldsymbol{r}, \boldsymbol{r}')$, is an impulse response from a point source located at location $\boldsymbol{r}'$ observed at location $\boldsymbol{r}$. For the system considered here, the Green's function needed is

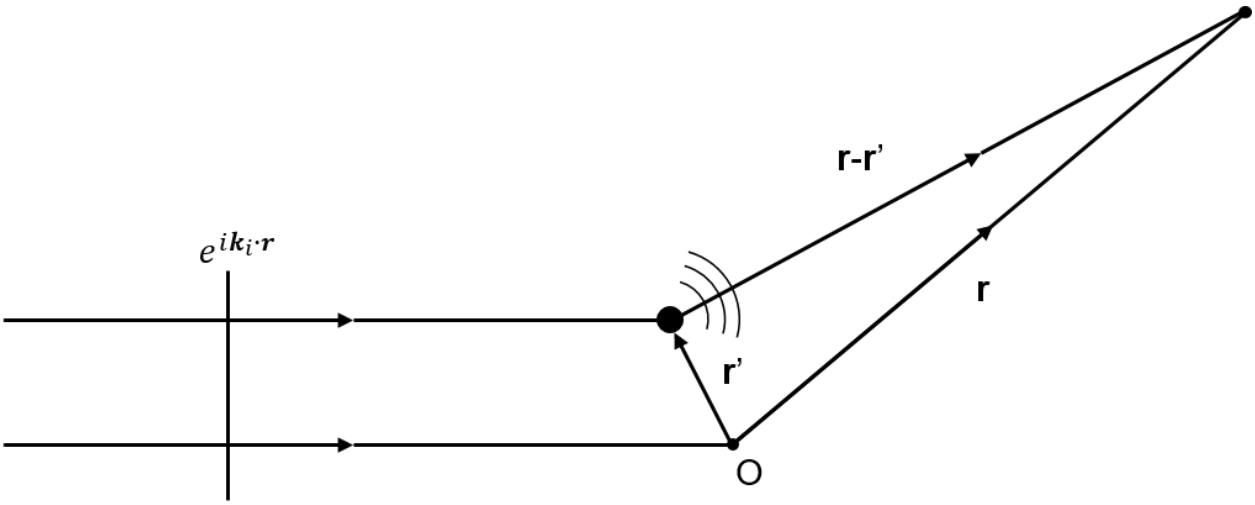

Figure 1.5: **Coordinate System of a Scattering Event**. An incident plane wave $e^{i\boldsymbol{k}_i\cdot\boldsymbol{r}}$ scatters from an object located at position $\boldsymbol{r}'$ from origin O. The response is observed at position $\boldsymbol{r}$. Adapted from [39].

the well-known out-going free space impulse response for the Helmholtz equation, a spherical wave

$$G(\boldsymbol{r}, \boldsymbol{r}') = \frac{e^{ik|\boldsymbol{r}-\boldsymbol{r}'|}}{|\boldsymbol{r}-\boldsymbol{r}'|}. \tag{1.44}$$

With this, a solution to Eqn. 1.43 is found such that the scattered wave is written as

$$\psi_s(\boldsymbol{r}) = \int f(\boldsymbol{r}')\frac{e^{ik|\boldsymbol{r}-\boldsymbol{r}'|}}{|\boldsymbol{r}-\boldsymbol{r}'|}\psi(\boldsymbol{r})d^3\boldsymbol{r}'. \tag{1.45}$$

This expression is starting to look tractable, however the wave inside the integral is the total wave and thus depends on knowledge of the scattered wave on the left hand side. To move forward, a few assumption and approximation must be made. First, it is assumed that the scattering potential is weak such that $\psi_s(\boldsymbol{r}) \ll \psi_i(\boldsymbol{r})$. Second, it is assumed that the incident wave field is a simple plane wave and can be written $\psi_i(\boldsymbol{r}) = e^{i\boldsymbol{k}_0 \cdot \boldsymbol{r}}$, with $\boldsymbol{k}_0$ the incident wave vector. Now, the total wave field can be replaced with just the incident field

$$\psi_s(\boldsymbol{r}) = \int f(\boldsymbol{r}') \frac{e^{ik|\boldsymbol{r}-\boldsymbol{r}'|}}{|\boldsymbol{r}-\boldsymbol{r}'|} e^{i\boldsymbol{k}_0 \cdot \boldsymbol{r}'} d^3\boldsymbol{r}'. \tag{1.46}$$

Finally, the observation point is taken to be sufficiently far away that the spatial extent of the scatterer can be neglected, or $|\boldsymbol{r}| \gg |\boldsymbol{r}'|$. Then the approximation $|\boldsymbol{r}-\boldsymbol{r}'| \approx r - \hat{\boldsymbol{r}} \cdot \boldsymbol{r}'$ holds with $\hat{\boldsymbol{r}}$ the unit vector in the $\boldsymbol{r}$ direction. With this, the scattered wave vector $\boldsymbol{k} = k_0 \hat{\boldsymbol{r}}$ is defined and a change of variables into momentum transfer space is performed with momentum transfer

$$\boldsymbol{q} = \boldsymbol{k} - \boldsymbol{k}_0. \tag{1.47}$$

The scatter field is then

$$\psi_s(\boldsymbol{r}) = \int f(\boldsymbol{r}') \frac{e^{ik_0 r - \boldsymbol{k} \cdot \boldsymbol{r}'}}{r} e^{i(\boldsymbol{k} \cdot \boldsymbol{r}' - \boldsymbol{q} \cdot \boldsymbol{r}')} d^3\boldsymbol{r}', \tag{1.48}$$

where the less stringent approximation $|\boldsymbol{r}-\boldsymbol{r}'| \approx r$ is made in the denominator of the integrand. Continuing to simplify

$$\begin{aligned} \psi_s(\boldsymbol{r}) &= \int f(\boldsymbol{r}') \frac{e^{ik_0 r - i\boldsymbol{k} \cdot \boldsymbol{r}'}}{r} e^{i(\boldsymbol{k} \cdot \boldsymbol{r}' - \boldsymbol{q} \cdot \boldsymbol{r}')} d^3\boldsymbol{r}' \\ &= \frac{e^{ik_0 r}}{r} \int f(\boldsymbol{r}') e^{i\boldsymbol{q} \cdot \boldsymbol{r}'} d^3\boldsymbol{r}' \\ &= \frac{e^{ik_0 r}}{r} \tilde{f}(\boldsymbol{q}), \end{aligned} \tag{1.49}$$

where it is seen that the scattered wave $\psi_s(\boldsymbol{r})$ is equal to the three dimensional Fourier transform of the scattering potential $f(\boldsymbol{r})$. The implication being that if light scattered from an object is observed or recorded as a diffraction pattern, then the object's spatial distribution can be recovered by a simple Fourier transform.

1.2.8 The Ewald Sphere, Far-field Diffraction, and the Born Approximation

With the approximations made in section 1.2.7, the momentum transfer was introduced as a convenient coordinate space to formulate the scattered wave generated by a given scattering potential. Because only elastic scattering is considered, $|\boldsymbol{k}| = |\boldsymbol{k}_0| = 2\pi/\lambda$, then Eqn. 1.47 implies that all possible $\boldsymbol{q}$ are confined to a two dimensional spherical shell embedded in a three dimensional space, the so-called Ewald sphere.

The Ewald sphere has radius $2\pi/\lambda$ and the incident and scattered wave vectors $\boldsymbol{k}_0$ and $\boldsymbol{k}$ pointing out from the center of the sphere. Typically, a coordinate system is chosen such that the incident wave vector is simply $\boldsymbol{k}_0 = k\hat{\boldsymbol{z}}$. If a detector is placed a distance z from the scatterer such that z is much larger than the sample dimensions, a relation between the detector plane coordinates $[x, y]$ and momentum transfer coordinates $[q_x, q_y, q_z]$ is derived through similar triangles, shown in Fig. 1.6. Notably, the transverse components of $\boldsymbol{q}$ and $\boldsymbol{k}$ are equivalent:

$$\begin{aligned} q_x &= k_x = k\frac{x}{\sqrt{x^2+y^2+z^2}} \\ q_y &= k_y = k\frac{y}{\sqrt{x^2+y^2+z^2}} \\ q_z &= k\left(\frac{z}{\sqrt{x^2+y^2+z^2}} - 1\right). \end{aligned} \tag{1.50}$$

Fig. 1.6 shows that there is a relation between the accessible parts of the Ewald sphere and the experiment geometry through the angle θ. The larger the angle θ, the more information of the Fourier distribution of the sample is captured on the detector. The information captured at larger angles corresponds to higher spatial frequency information about the sample, so the achievable resolution of a scattering experiment is directly linked to θ. This is parameterized through the numerical aperture (NA) of an imaging system and is simply defined by the detector size and experiment geometry for a lensless imaging system. For an experiment with detector size $2D$ and object-to-detector distance z, the NA is defined by

$$\mathrm{NA} = \sin\theta = \frac{D}{\sqrt{D^2+z^2}}. \tag{1.51}$$

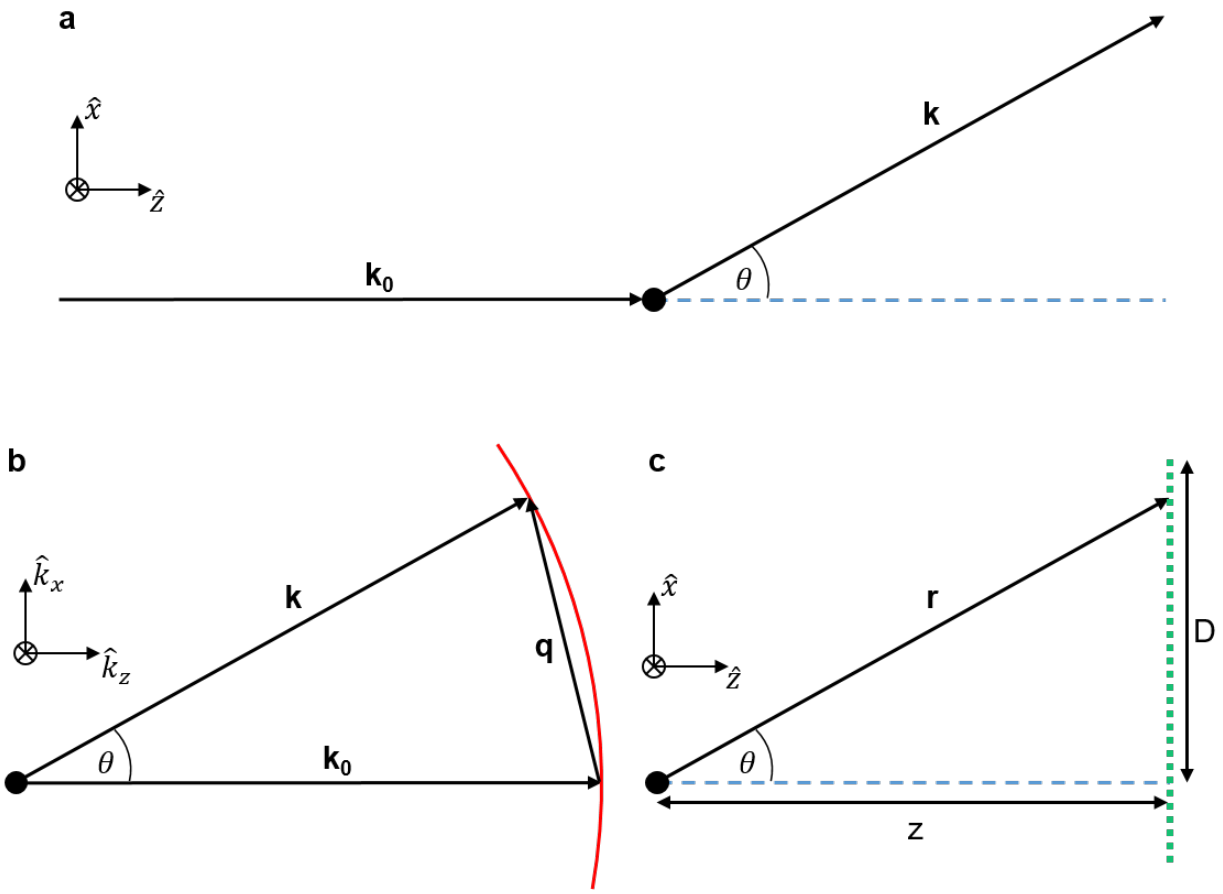

Figure 1.6: **Geometry of a Scattering Experiment**. (a) An incident plane wave with wave vector $\boldsymbol{k}_0 = k\hat{\boldsymbol{z}}$ scatters with an element and produces scattering vector $\boldsymbol{k}$ that makes angle θ with the optical axis. (b) The experimental geometry viewed in frequency space. Note that the scattering experiment is completely described by the momentum transfer vector q, which is restricted to values that lie on the Ewald sphere surface (red arc). (c) If a detector (green dotted line) with spatial extent D is placed a distance z that is much larger than the extent of the scatterer, then the detector coordinates $[x, y]$ and $z\hat{\boldsymbol{z}}$ form a triangle that is mathematically similar to the one defined by the components of scattering vector $[k_x, k_y]$ and k_z. The experiment geometry defines the NA of the system and along with the wavelength λ sets the spatial resolution limit of the experiment. At small angle, or large Ewald sphere radius, $q_z \approx 0$ and $\boldsymbol{q}$ is confined to a plane. Figure adapted from [40].

In the small angle approximation, the Ewald sphere is approximated as a plane and the

coordinate relations simply to

$$\begin{aligned} q_x &\approx k\frac{x}{z} \\ q_y &\approx k\frac{y}{z} \\ q_z &\approx 0. \end{aligned} \tag{1.52}$$

If the experiment is configured to have a high NA, the curvature of the Ewald sphere cannot be ignored and the scattered wave should no longer be described using only two dimensions. The curvature will result in a distortion in the higher spatial frequencies due to the projection of the Ewald sphere on to a two dimensional flat plane. The situation is further complicated if a system is configured with a non-normal incidence sample-beam geometry, where effects of conical diffraction nonsymmetrically distort the recorded diffraction pattern. This poses problems for the practical implementation of wave propagation methods that often rely on the fast Fourier transform (FFT) algorithm, which requires that the input signal is sampled on a linear grid. Fortunately, this nonlinear signal can be interpolated back to a linear grid spacing using a procedure called tilted plane correction (TPC) [41–43].

1.3 The Refractive Index and Contrast Generation

The first interpretation of the refractive index (n) that is often learned is that it is the ratio of the speed of a wave a it travels through a vacuum (c) to its speed inside a material (v), with $n = c/v$. While true, this definition glosses over some of the more subtle aspects of the index, most importantly that its value is dependent on the wavelength of light λ. When considering EUV and X-ray wavelengths, the value of the refractive index is often very close to 1. In this regime, it is common to write the refractive index as a continuous function of both space $\boldsymbol{r} = [x, y, z]$ and wavelength λ [23]:

$$n(\boldsymbol{r}, \lambda) = 1 - \delta(\boldsymbol{r}, \lambda) - i\beta(\boldsymbol{r}, \lambda). \tag{1.53}$$

The real and imaginary parts of the index describe the dispersive and absorptive components of a light-matter interaction and are given by

$$\delta = \frac{n_a\left(\boldsymbol{r}\right) r_e \lambda^2}{2\pi} f_1\left(\lambda\right) \tag{1.54}$$

$$\beta = \frac{n_a\left(\boldsymbol{r}\right) r_e \lambda^2}{2\pi} f_2\left(\lambda\right), \tag{1.55}$$

with n_a the spatially dependent atomic number density and r_e is the classical electron radius. f_1 and f_2 are called the atomic scattering factors and are measures of the scattering power of individual atoms as a function of wavelength. They are semi-empirical quantities that can be calculated and found in look-up tables for energies far from absorption features [44]. Close to absorption edges, the value of f_1 and f_2 depending strongly on local conditions of the atoms in a material so it is usually more accurate to rely on measured values instead of calculated predictions [45].

The monochromatic wave $\psi(\boldsymbol{r})$ exiting an object with refractive index distribution $n(\boldsymbol{r})$ may be parameterized using only two dimension with $\boldsymbol{r} = [x, y, z] = [\boldsymbol{x}, z]$ as

$$\psi(\boldsymbol{x}) = O(\boldsymbol{x})P(\boldsymbol{x}), \tag{1.56}$$

where $O(\boldsymbol{x})$ is the complex object transmission function and $P(\boldsymbol{r})$ is the wave incident on the sample propagating along the z-axis. This formulation is known as the the projection approximation and it is valid if the incident wave is sufficiently constant over the thickness of the object along the direction of propagation. For an in depth study on the validity of the approximation, see [46–48].

Under this assumption, the complex object transmission function can be written

$$O(\boldsymbol{x}) = A(\boldsymbol{x})e^{i\phi(\boldsymbol{x})}. \tag{1.57}$$

and contains information directly related to the absorption (imaginary) and phase shifting (real) parts of the complex refractive index through

$$A(\boldsymbol{x}) = e^{-\frac{2\pi}{\lambda}\int_0^T \beta(\boldsymbol{x},z)dz} \tag{1.58}$$

and

$$\phi(\boldsymbol{x}) = \frac{2\pi}{\lambda}\int_0^T \delta(\boldsymbol{x}, z)dz, \tag{1.59}$$

with T the object thickness along the axis of propagation. In CDI systems, this exit wave is propagated to a detector where a diffraction pattern is recorded. If the initial exit wave is retrieved, then a map of the spatially varying refractive index is obtained and material information about the sample is recovered.

1.4 Relevant Concepts in Microscopy

In this section some important concepts in imaging and microscopy are reviewed that are relevant to the work done in this thesis.

1.4.1 Amplitude and Phase Information

As detailed in section 1.3, light can be treated as complex field with

$$\psi(\boldsymbol{x}) = A(\boldsymbol{x})\, e^{i\phi(\boldsymbol{x})}, \tag{1.60}$$

where the amplitude $A(\boldsymbol{x})$ and phase $\phi(\boldsymbol{x})$ are both real. When this field is directly measured on a detector, only the intensity I is observed with

$$I = |\psi(\boldsymbol{x})|^2 = A(\boldsymbol{x})^2 . \tag{1.61}$$

If the field possesses $A(\boldsymbol{x}) = 1$, then the wave appears uniform when detected, no matter the structure of the phase. Fortunately, as a field propagates, amplitude and phase content begin to mix, meaning that a measurement of the intensity of the field in a different plane could give information about its phase structure elsewhere, the simplest example of this being interference fringes.

The amplitude of a wave field scattered from a sample often contains information about sample absorption while the phase carries information about structure. Together, they paint a complete picture about a sample's elemental and chemical composition as well as thickness and density.

There are a variety of microscopy technique that are developed specifically to measure phase information. Zernike phase contrast microscopy uses wave plates to convert phase difference pro-

duced by scattering from a sample into amplitude contrast in the formed image [49]. Holography uses an interferometric technique to simultaneously record both amplitude and phase information about a sample by interfering a scattered wave with a known reference beam [36]. Chapter 3 details how coherent diffractive imaging can be used to recover both phase and amplitude of a sample.

1.4.2 Resolution

Resolution is often the first characteristic thought about when investigating an imaging system. Ernst Abbe arrived at his resolution criteria by applying concepts of Fourier analysis to the problem of image formation. Abbe considered an object to be composed of a series of sinusoidal components with varying frequency and angle, and an image is formed by the interference between the diffraction from these different components [4].

When illuminated, the sinusoids produce diffraction orders propagating at different angles proportional to their frequency. Abbe contended that the a sinusoid component was detectable if the first order diffraction was collected by the imaging system. Abbe formulated this analysis into a resolution criteria that depends on the geometry of an imaging system

$$\delta r = \frac{\lambda}{2\mathrm{NA}} \tag{1.62}$$

where δr is the smallest resolvable feature in an image, λ is the illuminating wavelength, and NA is the numerical aperture of a system. The NA is define by the maximum angle subsumed by the system aperture and the refractive index $\mathrm{NA} = n \sin\theta$. Imaging system that reach this performance are said to have "diffraction-limited" resolution.

The Rayleigh and Sparrow criteria have also been used to quantify resolution, differing from Abbe's definition through a numeric factor added to right hand side of Eqn. 1.62, (1.22 in the case of Rayleigh, and 0.94 for Sparrow) [50]. Spatial frequency analysis of an imaging system allows for further definitions using the frequency response of the system [36].

Typically, the resolution of a microscope is thought of as being system dependent. Meaning that images produced with a system will have some resolution and that resolution is dependent on

the configuration of the microscope. For diffractive imaging systems, such as the ones discussed in this thesis, this is not entirely accurate. Though the resolution limit is very much set by the system geometry (i.e. Eqn. 1.62) the actual resolution of an image depends on the scattering power of a sample. If the sample cannot efficiently scatter to the maximum acceptance angle of the NA, then the resolution is limited by the sample, not the system.

1.4.3 Coherent vs. Incoherent Scattering

The particular character of coherent scattering is important for coherent diffractive imaging. To illustrate why, consider an inhomogeneous scattering medium, for this example: a collection of nanoparticles, illuminated by a beam of light, with its diffraction pattern measured in the far-field. There are three important length scales in this problem, the illumination wavelength λ, the average distance between nanoparticles d, and the size of the illuminated area a [40].

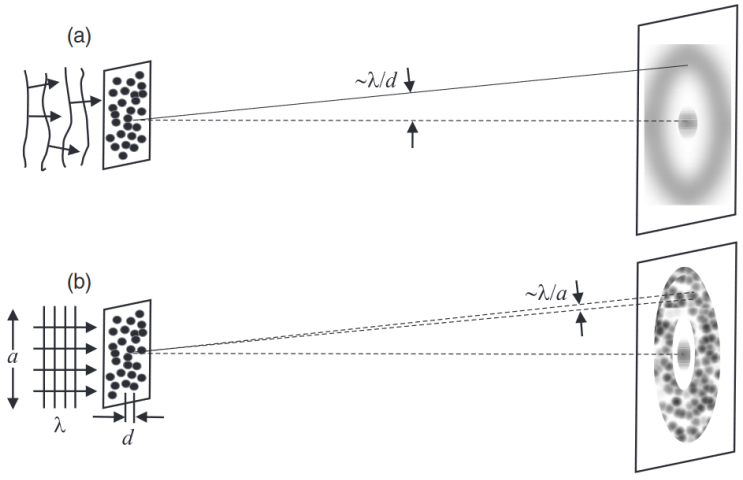

Figure 1.7: **Incoherent vs. Coherent Scatter**. Diffraction from a collection of nanoparticles with inter particle distance d and illumination width a. (a) Under incoherent illumination, a continuous diffraction ring is observed. (b) With coherent illumination, a speckled diffraction pattern unique to the particular particle configuration is produced. Figure reproduced from [40].

If the illumination is incoherent (Fig. 1.7(a)), then the recorded diffraction pattern exhibits a maximum intensity at angle $\sim \lambda/d$. This results from the diffraction pattern representing an average over the many different wavefronts incident on the sample and can equivalently be thought

of as an average over many different particle ensembles. Varying a will not change the diffraction pattern, only the area over which the incoherent wavefronts are averaged.

When coherent illumination is used (Fig. 1.7(b)), a similar dependence is observed, but finer features with angular width $\sim \lambda/a$ appear – the speckle. These arise from interference between wavefronts scattered from different particles. If a single particle position changes, all interferences are affected, and the speckle pattern changes.

With this picture, it is understood that diffraction from coherent illumination reflects a *particular* realization of the system, whereas incoherent illumination provides an average over an *ensemble* of slightly different system configurations. It follows that from the coherent scatter pattern, an object's unique structure may be recovered. Details of how to perform this inversion are discussed in chapter 3.

Chapter 2

Coherent Radiation Sources

Coherent sources of X-ray and EUV light fall generally into two categories: facility scale sources and tabletop sources. Facility scale sources such as free electron lasers (FEL) and synchrotron sources leverage relativistically accelerated electrons to generate high brightness and high energy radiation that can be configured to emit over a very broad spectral bandwidth [51]. Through filtering, these sources can be made spatially coherent. However, as a user facility these sources are often very large – sometimes the size of several buildings – and have limited availability for users, as well as a high cost of operation and maintenance. These sources are best for studies requiring a hight flux and high energy light source.

Tabletop sources, on the other hand, tend be far cheaper and readily installable in research and industrial settings. This gives greater access and allows for rapid prototyping and greater customization for the specific needs of an experiment. Tabletop sources such as X-ray lasers and and high harmonic generation systems tend to have lower flux and spectral bandwidth, but research into these sources is rapidly closing the gaps with their facility-scale counterparts. Work in this thesis focused on HHG and synchrotron light sources, a more detailed discussion of these sources is presented here.

2.1 Synchrotron Radiation

The synchrotron light source grew out of early efforts from high-energy physicists to construct particle accelerators to study high-energy and nuclear physical phenomena [52, 53]. As accelera-

tor technology continued to develop and the understanding and benefits of coherent light sources became apparent, synchrotron particle accelerators were developed to specifically act as a high brilliance electromagnetic radiation sources [54]. A diagram of the Advanced Light Source (ALS) at the Lawrence Berkeley National Lab – where work in this thesis was carried out – is depicted in Fig. 2.1, showing a schematic layout of the components of a synchrotron radiation source.

A synchrotron generates radiation by accelerating electrons to extremely high, relativistic speeds through a curved trajectory. An electron gun produces electrons that travel into a linear accelerator that accelerates the electrons using a series of radio frequency cavities. The electron beam (current) is inserted into a booster ring which increases the electron energy using a series of bending magnets similar to the larger storage ring.

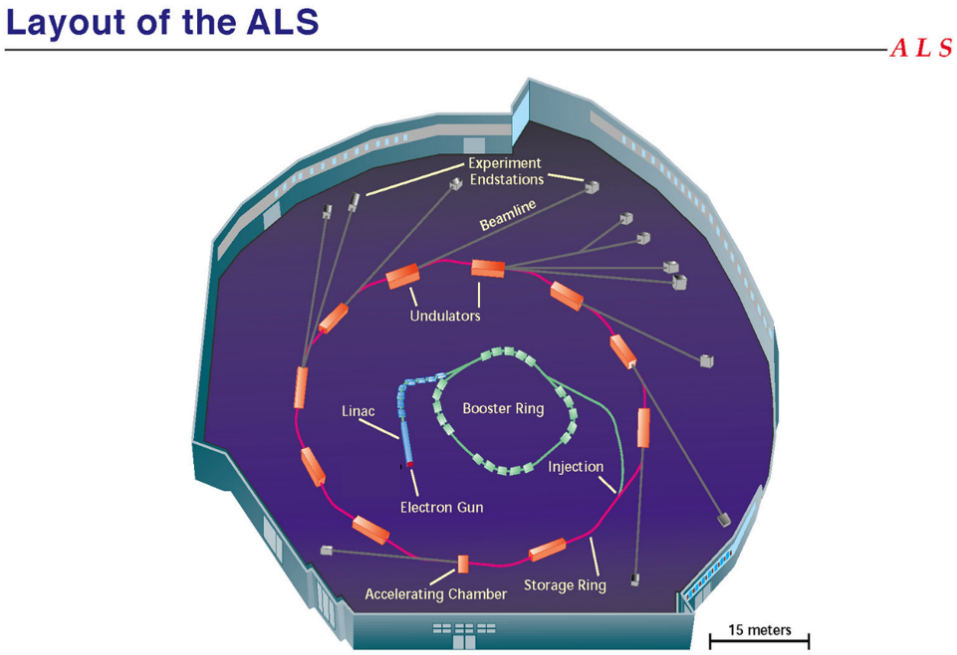

Figure 2.1: **The Layout of the Advanced Light Source**. A diagram of the Advanced Light Source, a third generation synchrotron light source. A series of three accelerators (linear accelerator, booster ring, and storage ring) accelerate electrons to 1.9 GeV. Synchrotron radiation is produced in bending magnets and undulators. Beam lines tap into the radiation and direct the light into experiment end stations. Image from [55].

Once the electrons are accelerated, they are inserted into the storage ring, which maintains a

high current and electron energy using bending magnets to confine the electrons' path. Beam lines are setup around the storage ring to tap into the radiation produced by the accelerating electrons. Synchrotron sources are not continuous, rather electrons bunches are created at the nodes of the accelerating radio-frequency field. The brilliance and spectrum of the synchrotron is altered and enhanced through the placement of insertion devices in the storage ring [23].

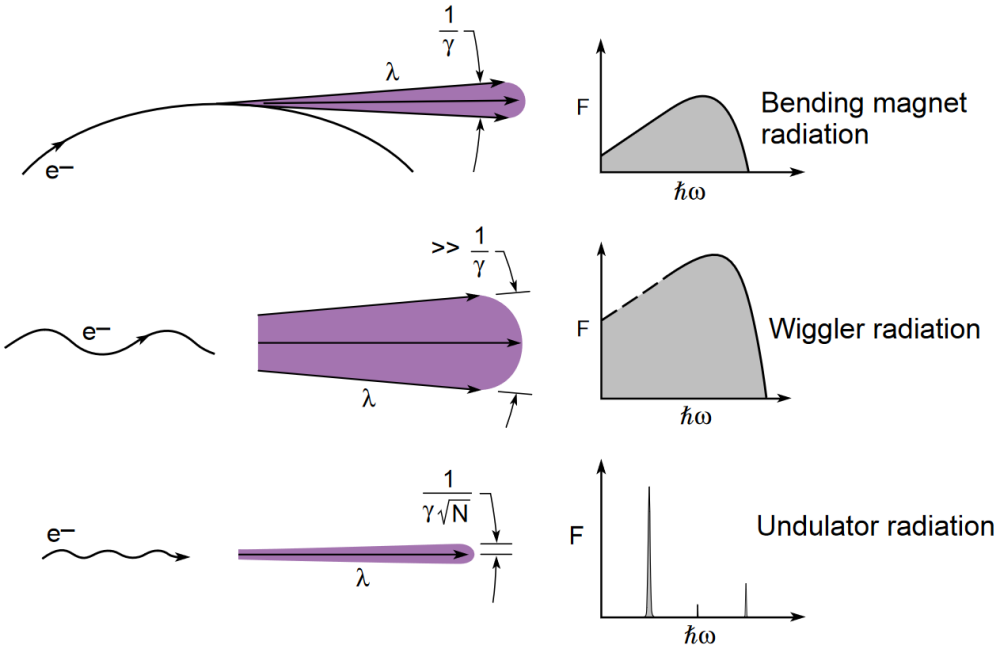

Figure 2.2: **Types of Synchrotron Radiation**. Synchrotron radiation is produced with three types of devices. Bending magnets, used to confine the electron trajectory to a closed path, are the earliest device and produce radiation in with a broad spectrum. Wiggler and Undulators are periodic magnetic arrays that cause deviations in the electron path. These deviation result in increased acceleration and therefore radiation flux. These devices differ primarily in the strength of their magnetic field, which can be set to produce a bright but highly divergent beam with a broad spectrum (wiggler), or a more collimated and narrow band emission (undulator). Reproduced from [23].

An insertion device is a periodic magnetic structure that causes the electron path to transversely oscillate. Wigglers and undulators are similar insertion devices, that deviate only in the strength and period of their magnetic structure. Wigglers use a much higher magnetic field that causes a significant deviation in the electron beam, generating more synchrotron radiation at the expense of poor beam divergence. Undulators use a weaker magnetic field to produce smaller oscil-

lations in the electron beam. These smaller oscillations allow the radiation bursts from successive oscillations to interference, producing a much more narrow-band radiation spectrum with a smaller divergence [56]. A schematic of the different types of synchrotron radiation is shown in Fig. 2.2.

2.2 High Harmonic Generation

High harmonic generation (HHG) is an extremely nonlinear process where an intense, ultrafast burst of coherent light of some fundamental frequency is upconverted to a higher frequency harmonic [18, 57]. The polarization and coherence properties of the input light is preserved in the simplest geometry while the pulse duration is actually reduced. However, it is possible to tune the coherence and polarization properties using selection rules or molecular targets [58–60]. The technique provides a compact and flexible way to produce coherent light in the VUV to hard X-ray regimes when properly phase matched [19–22, 61, 62] and is driving a revolution in uncovering new understanding of interactions in quantum materials [61, 63–66], nanoscale transport [67, 68], and coherent imaging [69–71].

2.2.1 The Three-Step Model

The three-step model is an elegant, simplified solution to the problem of HHG [72–74]. The model is semi-classical, ignoring many details of the fully quantum mechanical description of the process. Nonetheless, the model provides an intuition into the HHG process and accurately predicts a number of important features.

The three-step model is formulated by considering the interaction of a single atom with an ultrafast laser pulse. The three-step model process, depicted in Fig. 2.4, is as follows:

(1) An electron is ionized by the extremely strong electric field of the laser pulse. The ionization is a result of the suppression of the Coulomb field at the peak of the intense field of the pulse.

(2) The electron is accelerated away from the parent atom, driven by the upcycle of the laser's

electric field. On the down cycle, the electron's acceleration reverses and it is driven back toward the parent ion, gaining momentum and kinetic energy.

(3) The electron arrives back at the parent ion where there is a finite probability of recombination that produces a photon releasing the energy accumulated by the free electron.

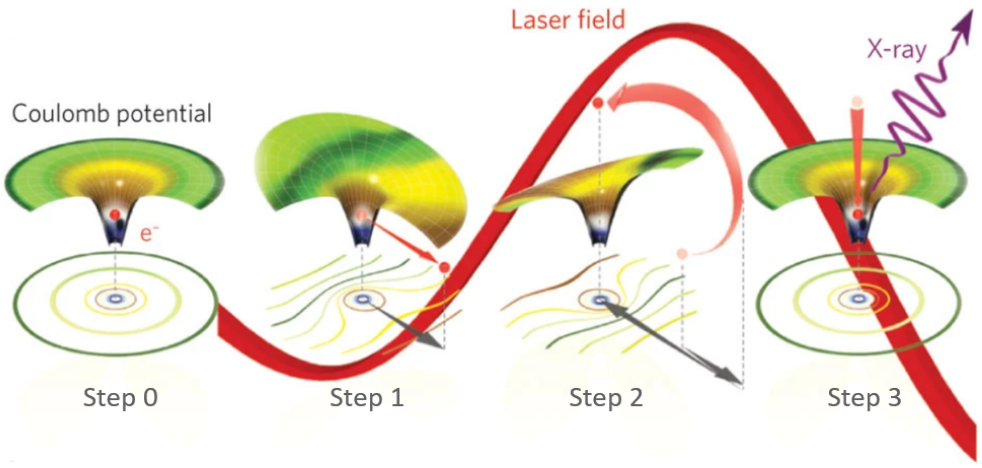

Figure 2.3: **The Three-Step Model**. Step 0: The ground state before the atom interacts with laser field. Step 1: The strong laser field causes an electron to tunnel ionize into the continuum. Step 2: The free electron is accelerated by the external field, gaining energy. Step 3: The free electron is driven back to its parent ion where it recombines, releasing its excess energy as a high energy photon. Adapted from [75].

The energy of the emitted photon depends on both the ionization potential of the parent atom as well as the amount of kinetic energy gain while in the continuum. This energy is understood by considering the kinematic equations of motion of a free electron driven by an oscillating electric field. Depending on which part of the external field cycle the electron is ionized at, the particle will have differing amounts of kinetic energy when it recombines with the parent ion. By considering all the different cycle points where ionization can occur, the maximum kinetic energy is found to be $E_k^{max} = 3.17U_p$. Where U_p is the ponderomotive energy, the energy the electron experiences in an oscillating external field – sometimes called the cycle-averaged "quiver" energy – is given by [72]

$$U_p = \frac{e^2}{c\epsilon_0 m_e}\frac{\lambda^2}{4\pi^2 c^2}\frac{I}{4}, \tag{2.1}$$

where e is the electron charge, m_e is the electron mass, λ is the driving laser wavelength, and I is the driving laser peak intensity. The maximum photon energy, or "cutoff energy", is given by the sum of the ionization potential of the parent atom I_p and the maximum kinetic energy [72, 74]

$$h\omega_{cutoff} \approx I_p + 3.17Up \propto I\lambda^2. \tag{2.2}$$

Eqn. 2.2 reveals an interesting feature of HHG: longer wavelength driving lasers can produce higher energy photons during HHG. This can be understood by again considering the kinematics of a free electron in an oscillating external field. The longer the wavelength of the driving laser, the longer the electron is accelerated. This higher energy comes at the expense of HHG flux, as many of the fundamental energy photons are required to create one high energy photon.

With the three-step model giving an intuitive understand of the HHG process, it is seen that with a sufficiently strong laser field, HHG is a fairly robust method for producing EUV light. Indeed, HHG has been demonstrated with many different media, including solid [76] and plasma [77] targets, as well as a diluted gas [78] and gas-filled waveguides [79]. However, only the single emitter picture has been considered. To get bright, high energy EUV light, a coherent summation of many single emitters is needed.

2.2.2 Phase Matching

With the intuitive understanding of the HHG process through the three-step model, attention must now be placed on how to generate bright, coherent beams of EUV light. In order to buildup the the emission from many single emitters, their emission must constructively interfere at the macroscopic level. This process is called phase matching and refers to matching the dispersion of the HHG EUV light with the driving laser field within the generating medium. Many different media and techniques have been investigated for phase matching, the discussion here is restricted to phase matching in a gas-filled capillary waveguide [19, 80], which was the HHG method used for the work in this thesis. Due to the large difference in the EUV and fundamental field wavelengths, there is an inherent dispersion mismatch that must be compensated. This is done by adjusting the

properties of the generating medium by varying experimental parameters [19, 81, 82].

The phase matching condition is a statement that the phase velocity $v_p = w/k$ of the fundamental field must be matched with the EUV harmonics. For the q^{th} harmonic order and driving laser with wave number k_L, the phase matching condition is

$$\Delta k = k_q - qk_L = 0. \tag{2.3}$$

Inside a gas-filled capillary waveguide, this dispersion mismatch has three primary contributions and is written as [19, 80]:

$$\Delta k \approx \underbrace{q\frac{\mu_{11}^2\lambda_L}{4\pi a^2}}_{\text{geometric}} - \underbrace{q\frac{2\pi P(1-\eta)}{\lambda_L}(\Delta\delta + n_2)}_{\text{atoms}} + \underbrace{qP\eta N_a r_e \lambda_L}_{\text{free electrons}}. \tag{2.4}$$

Here q is the harmonic order, μ_{11} is the mode factor – a geometric constant from the waveguide coupling [83] – that is the first zero of a Bessel function of the first kind, λ_L is the fundamental laser wavelength, a is the radius of the waveguide, P is the pressure inside the waveguide, η is the ionization fraction, r_e is the classical electron radius, N_a is the number density of atoms/atm, $\Delta\delta$ is the difference in the indices of refraction of the gas for the two wavelengths of light, and $n_2 = \tilde{n}_2 I_L$ is the nonlinear index of refraction at λ_L.

The first term is a geometric dispersion term arising from the propagation of the fundamental wavelength through the waveguide. This term results in phase shifts in the laser as a function of propagation distance, and affect the relative phases of the emitted harmonics. The second term describes the phase of the neutral atoms, including contributions from both dispersion and the nonlinear refractive index. The third term is the dispersion from electrons as a result of the atom's ionization by the intense laser pulse. Note that both the neutral atom and the free electron dispersion terms depend on the pressure inside the capillary P, while the geometric and free electron terms provide positive dispersion and the neutral atom term is negative. This indicates that the pressure inside the waveguide is a convenient experimental knob to tweak to achieve phase matching.

Using the phase matching condition $\Delta k = 0$ with Eqn. 2.4, the phase matching pressure is

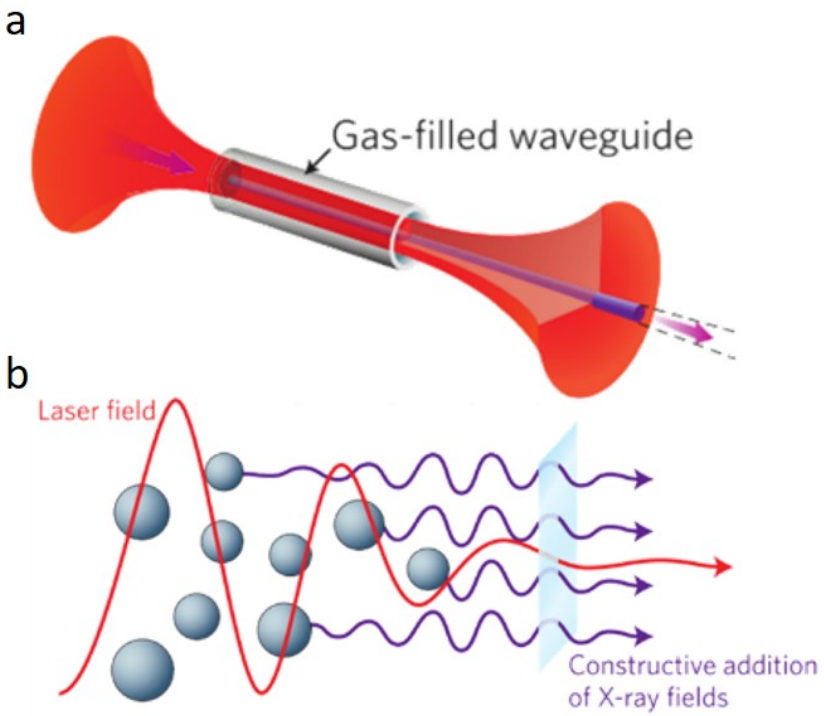

Figure 2.4: **Phase Matching in a Gas-filled Waveguide**. (a) HHG in a gas-filled capillary waveguide. An intense, ultrafast IR pulse is focused into a waveguide triggering the three-step model and harmonic generation. When properly phase matched, bright, coherent EUV light is emitted collinearly with the driving laser, but with a different divergence. (b) A diagram of properly phase matched HHG, showing the coherent addition of EUV photon emission. Adapted from [75].

found

$$P \approx \frac{\mu_{11}^2 \lambda_L^2}{4\pi a^2} \frac{1}{2\pi(1-\eta)(\Delta\delta + n_2) - \eta N_a r_e \lambda_L^2}. \tag{2.5}$$

From Eqn. 2.5, there are some values of the ionization fraction which results in a nonphysical pressure for phase matching. This occurs when the denominator goes to zero. Solving for this point gives the critical ionization level [79]

$$\eta_c = \frac{1}{1 - \frac{N_a r_e \lambda_L^2}{2\pi(\Delta\delta + n_2)}}, \tag{2.6}$$

which sets an upper limit on the the intensity of the driving laser light that can be used for HHG, as a higher intensity leads to a larger η. Recalling Eqn. 2.2, it is seen that the cutoff energy of the HHG process cannot be driven higher by simply increasing the intensity of the laser field, as

the ionization will prevent phase matching above η_c. Therefore, to obtain higher energy photons through HHG, longer wavelength high intensity laser systems are needed to drive the process.

Chapter 3

Ptychography Coherent Diffractive Imaging

3.1 Introduction

Coherent diffractive imaging (CDI) is a broad assortment of imaging techniques that seek to produce a real space image of a specimen using only measurements from the specimen's scatter pattern. These techniques use phase retrieval, a method that transfers the task of image formation from physical optics – i.e. lenses – to a computational algorithm that solves for the phase of an object given its measured diffraction intensity and additional *a priori* information about experimental constraints.

Without the need for image forming optics, CDI has exploded in popularity in the X-ray and EUV microscopy communities where quality, high power image forming optics are difficult to fabricate. Since its first demonstration using coherent X-rays in 1999 [84, 85], CDI has found wide applications across varied fields such as material science [86–88], semiconductor science [89, 90], biological science [91, 92], and many more [35, 93]. With the added benefits of diffraction-limited resolution and phase-contrast sensitivity, CDI is an instrumental tool driving the nanoscale microscopy revolution of the last decade. This chapter discusses the formulation of the phase retrieval problem and its solution as through iterative optimization.

3.2 The Phase Problem

The phase of light is not directly measurable. In so many words, that is the *phase problem*. Indeed, when light is collected on any detector – the eye, photographic paper, or charge-coupled

devices (CCD) – only the intensity of the wave is measured, leaving the phase information to be observed through interferometric techniques. More formally, given a light wave with complex scalar amplitude $\psi = Ae^{i\phi}$ with A and ϕ real, then an intensity-based detector will measure

$$I = |\psi|^2 = A^2, \tag{3.1}$$

and the phase information is lost on detection. This is unfortunate as according to Eqns. 1.36 and 1.34, the wave at the detector plane and directly behind the object – the exit surface wave (ESW) – are related through simple Fourier transform relationships. If the phase of the measured diffraction is recovered, then together with the measured intensity, the ESW is found through a simple inverse Fourier transform. This task is known as *phase retrieval*.

Mathematically, half of the information carried in the diffracted wave is lost during the intensity measurement. To account for this, additional constraints must be enforced on the system to uniquely determine the object. Usually, this is done with known or previously measured aspects of the system geometry or a priori information about the sample. The phase retrieval problem can then be thought of as an optimization to find an ESW that both produces the measures intensity and satisfies the additional constraints.

3.3 Coherence

As the name suggests, CDI requires a certain degree of spatial and temporal coherence. Coherence is a measure of how well correlated a wave is with itself in both space and time. More formally, a coherent wave has a fixed phase relationship between space and time such that if the wave is measured at spatial point x_1 and temporal point t, then at some different place x_2 and different time $t + \tau$ the wave can be perfectly predicted. For a wave $\psi(x, t)$, the mutual coherence function is defined to be the correlation between between the wave at points x_1 and x_2 and time separation τ.

$$\Gamma(x_1, x_2, \tau) = \langle \psi(x_1, t)\psi^*(x_2, t + \tau) \rangle_T \,, \tag{3.2}$$

with $\langle\cdot\rangle_T$ represents the ensemble average over time period T. Typically this function is normalized to give the complex coherence factor

$$\gamma(x_1, x_2, \tau) = \frac{\Gamma(x_1, x_2, \tau)}{\sqrt{\Gamma(x_1, x_1, 0)\Gamma(x_2, x_2, 0)}} = \frac{\Gamma(x_1, x_2, \tau)}{\sqrt{I(x_1)I(x_2)}} \tag{3.3}$$

where $I(x)$ is the intensity of the field at point x. The modulus of 3.3 gives the ratio of coherent intensity to total intensity and is a measure of the coherence properties of the wave field, with $|\gamma| = 1$ being fully coherent and $|\gamma| = 0$ being fully incoherent [37]. In practice, it is often useful to find the distinct length and time scales over which the degree of coherence is high for a given source, these will set physical limits on the CDI experiment geometry and attainable resolution.

3.3.1 Transverse Coherence Length

Transverse coherence, also referred to as spatial coherence, is the distance $|x_1 - x_2|$ for which γ falls to 0. In a CDI experiment, the probing illumination area must be fully spatially coherent in order for the object and diffraction pattern to be related through a Fourier transform.

A good measure for spatial coherence is interference fringe visibility in the diffraction from an object illuminated by a light source. The simplest form being a Young's double slit experiment, which is used to construct a relation between experimental geometry and transverse coherence. Consider the Young's double slit experiment shown in Fig. 3.1. In this setup, a source of width a is placed a distance R before a screen with two slits separated by distance d. The diffraction from the two slits is viewed on a screen placed a distance L away. The transverse coherence length can be quantified as the slit separation d for which the visibility of the fringes in the diffraction goes to zero. This means that the minima of the diffraction pattern produced by illuminating the double slit with a point source on the optical axis coincides with the maxima of the diffraction produced by the double slits illuminated by a point on the edge of the extended source [40]. In the small angle approximation, the angle of the m^{th} maximum for on axis illumination is given as $\theta_{max} = m\lambda/d$ and the m^{th} minimum occurs at $\theta_{min} = (m + 1/2)\lambda/d$ for illumination on the optical axis[94]. When the point source is shifted a distance $a/2$ off the optical axis, the location of the

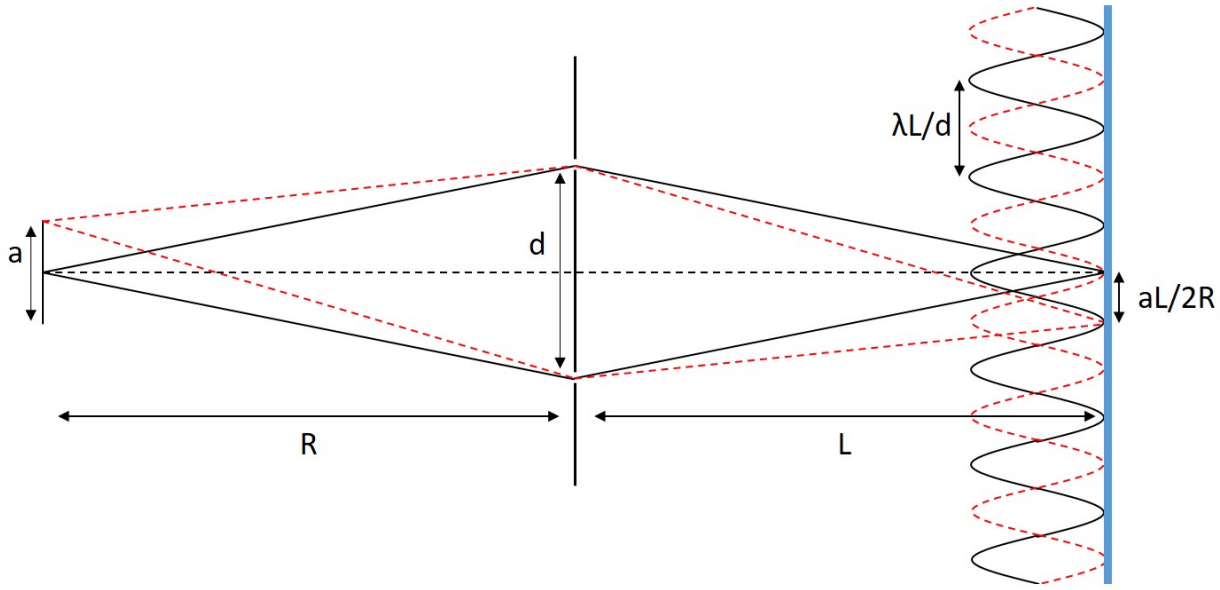

Figure 3.1: **Spatial Coherence Measurement**. A simple geometry to measure transverse coherence length of an extended light source. The interference fringes produced from a illumination on the optical axis (solid black lines) and on the edge of the source of size a (red dashed lines). The slit distance d for which the fringes are exactly out of phase corresponds to the transverse coherence length of the system L. Reproduced from [40].

extrema are shifted by an angle $\Delta\theta = a/(2R)$. Equating the maxima of the on-axis illumination with the minima of the off-axis source gives the relation $\lambda/(2d) = a/(2R)$. Solving for d then gives the transverse coherence length $L = d = \lambda R/a$. In practice, an extended source may be asymmetric so a transverse coherence length in the horizontal and vertical direction with source dimension a_h by a_v are given by

$$L_h = \lambda R/a_h, \qquad L_v = \lambda R/a_v. \tag{3.4}$$

In terms of a CDI system, the slit separation used in the example above can be thought of as the width of the object – or illumination in the case of ptychography– D. The interference fringes considered are thought to arise from two point source emitter on either side of the object. With this context, it can be seen that the transverse coherence length of the source must be greater than D to ensure the visibility of the interference effects that the imaging technique relies on [95].

3.3.2 Longitudinal Coherence Length

The longitudinal coherence length, or temporal coherence, is a measure of the coherence of a wave along its direction of propagation. More formally, it is the self-correlation of the wave at a fixed point, but at two different times. The coherence time T_c is the time over which the phase of the wave can be predicted given its measurement at some earlier point. This time can be converted to a longitudinal coherence length through a factor of the speed of light, $L_l = cT_c$. To derive a relation for L_l, consider two waves, one with wavelength λ and the other with wavelength $\lambda + \Delta\lambda$. These waves depart from the same point in space and time and propagate. L_l is defined as the distance the waves propagate until they are exactly out of phase, see Fig. 3.2 [40].

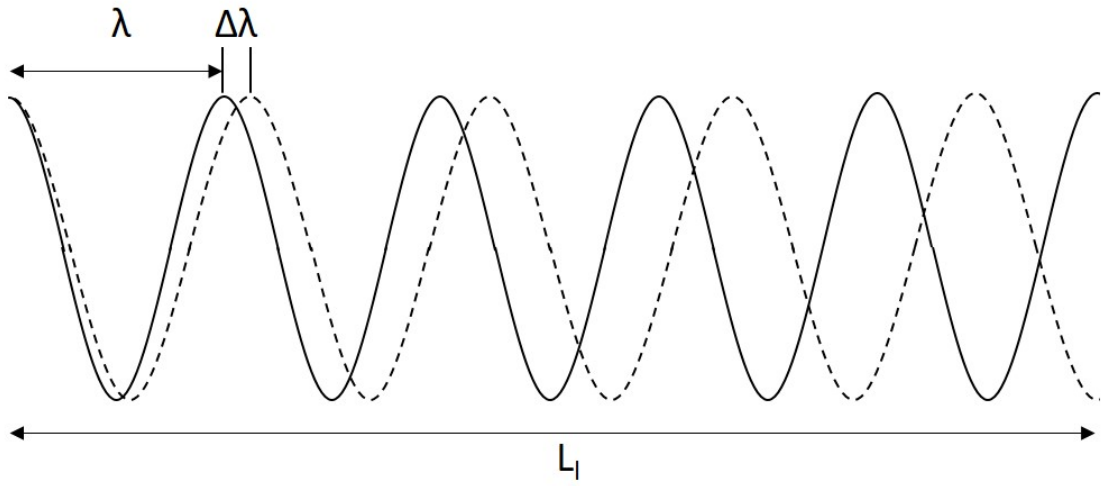

Figure 3.2: **Longitudinal Coherence Measurement**. Two waves with wavelengths λ and $\lambda+\Delta\lambda$ originate from the same point in space and time. After propagating the longitudinal coherence length L_l, the waves are exactly π out of phase. Reproduced from [40].

After this distance, the first wave has made N oscillations, and the second wave must have made $N - 1/2$ oscillations. If the waves are in antiphase, then $N\lambda = (N - 1/2)(\lambda + \Delta\lambda)$. Solving for N and recalling that $L_l = N\lambda$, the coherence length is found to be

$$L_l = \frac{1}{2}\frac{\lambda^2}{\Delta\lambda}. \tag{3.5}$$

Note that the exact pre-factor is dependent on the spectral density of the source [96].

The longitudinal coherence has an interesting effect on CDI system: it limits the attainable resolution. For waves scattered at an angle θ from either end of an object with width D, the path length difference between the two waves is given by $\Delta d_{path} = D \sin\theta$. In order to have coherent interference $L_l > \Delta d_{path}$. Recalling the relations from section 1.2.8 gives

$$\frac{\lambda^2}{\Delta\lambda} > D \sin\theta \approx D\frac{q}{k}. \tag{3.6}$$

If the largest detectable momentum transfer is considered, q_{max}, a relationship between source fractional bandwidth and real space resolution δx can be found using $\delta x = 2\pi/q_{max}$

$$\frac{\Delta\lambda}{\lambda} < \frac{\delta x}{D}. \tag{3.7}$$

Unless the above relation is satisfied, there will not be coherent interference at the edge of the measured diffraction pattern.

Similarly, when using a pulsed light source, the temporal coherence is limited to the pulse duration τ_p. The path length distance has an associated time delay $\Delta t_{path} = \Delta d_{path}/c$. If $\Delta t_{path} > \tau_p$, then even if the pulse is coherent throughout its duration, the pulse does not exist long enough to get the required interference and the diffraction pattern will be blurred. Following a similar process to the one outlined above, the maximum resolution (i.e. highest angle scatter) that can be collected for a given object size D and pulse duration is $\delta x = \lambda D/\tau_p c$.

3.4 Sampling

The use of pixelated detectors and digital imaging processing for CDI data acquisition and image reconstruction means that continuous functions and mathematical operations must be adequately represented through discrete arrays. As such, care must be taken when selecting the sampling interval such that the original continuous function is accurately represented by discrete points on a finite grid. The condition for this is the Shannon-Nyquist sampling theorem, which states that in order to reproduced a continuous waveform from discrete samples, it must be sampled at an interval twice that of the highest frequency present in the waveform [97].

3.4.1 Some implications of a theorem due to Shannon

When taking the discrete Fourier decomposition of a discretized function with N samples and sample spacing δx, the sampling rate in reciprocal frequency space δf is given through the relation

$$\delta x \, \delta f = \frac{1}{N}. \tag{3.8}$$

With the transform centered on the gird, the largest frequency f_{max} contained in the decomposition is then

$$f_{max} = \frac{N}{2}\delta f = \frac{1}{2\delta x}. \tag{3.9}$$

This means that if a wave form contains frequencies such that $f > f_{max}$, then that information is aliased down to lower frequencies where it adds additional power to lower frequency Fourier components. This is a consequence of the periodic boundary conditions assumed by the discrete Fourier transform. In order to properly sample a function, it must be bandwidth-limited such that any content with $f > f_{max}$ is zero.

The Nyquist frequency f_{Ny} is defined as the cut-off frequency for a function's bandwidth with $f_{Ny} \leqslant f_{max}$. Using Eqn. 3.9, a minimum sampling rate is found to be twice the Nyquist frequency $\delta x \leqslant 1/(2f_{Ny})$ [98].

In Sayre's seminal works on CDI, the idea is proposed that the phase problem could be solved through adequate sampling of an object's diffraction pattern. In his brief article "Some implications of a theorem due to Shannon", Sayre considers a function $o(x)$ which is only nonzero over a finite size a in real space [99]. To determine the required sampling rate to uniquely determine the Fourier transform of $o(x)$, Sayre considered a the real space analogue of twice the Nyquist frequency. Accordingly, the Fourier transform $\tilde{o}(f)$ must be sampled at a rate $\delta f = 1/a$. However, in a diffraction experiment, $|\tilde{o}(f)|^2$ is measured which corresponds to the Fourier transform of function's autocorrelation $o(x) \star o(x)$. The width of a function's autocorrelation is twice that of the function itself, so the measured diffraction must be sampled at $\delta f \geqslant 1/2a$ to uniquely record the intensity. Initially, this idea was proposed as a method for crystallography, but did not receive

much attention as the diffraction patterns are composed of distinct peaks with spacings $\delta f = 1/a$. However, the idea was later expanded to noncrystalline samples, with the characteristic dimension a reinterpreted as the localized sample or illumination width [100].

3.4.2 Sampling and Experimental Geometry

Consider now a diffraction pattern recorded with a pixelated detector of size $N_x \times N_y$ with pixel area $p_x \times p_y$ positioned a distance z from the object scattering the light. Using Eqn. 1.52, it is seen that the frequency sampling interval is determined by the experimental geometry with

$$\begin{aligned} \delta f_x &= \frac{p_x}{\lambda z}, \\ \delta f_y &= \frac{p_y}{\lambda z}. \end{aligned} \tag{3.10}$$

Through the discrete Fourier transform, a relation between the object sampling interval and the detector plane frequency content is established. Using Eqn. 3.8 the object sampling rates are

$$\begin{aligned} \delta x &= \frac{\lambda z}{N_y p_y}, \\ \delta y &= \frac{\lambda z}{N_y p_y}. \end{aligned} \tag{3.11}$$

It is now assumed that the object is represented by a function $o(x, y)$ with finite extent $D_x \times D_y$. Then to sample the diffraction pattern intensity without aliasing

$$\begin{aligned} \delta f_x &\leqslant \frac{1}{2D_x}, \\ \delta f_y &\leqslant \frac{1}{2D_x}. \end{aligned} \tag{3.12}$$

Equating Eqn. 3.10 and 3.12 gives the dimensionless quantity

$$\sigma_{x,y} \equiv \frac{\lambda z}{p_{x,y} D_{x,y}} \geqslant 2. \tag{3.13}$$

σ is referred to as the oversampling and the condition that it be greater than two is actually just the Nyquist sampling condition for the autocorrelation of the object. The condition that $\sigma \geqslant 2$ is generally required for CDI experiments [84, 101–103]. Because the diffraction pattern is the measurement of interest, not the intensity of the diffraction pattern, it is common to refer to a

diffraction pattern as "oversampled" in an experiment. Recalling the diffraction-limited resolution of an imaging system is given by $\lambda/2\text{NA}$ with NA inversely proportional to z, it is clear that there is a trade off between resolving power and oversampling when designing a CDI system.

An important implication of the sampling requirements in CDI is a restriction on the experimental geometry. For example, taking $\sigma = 2$ and rearranging Eqn. 3.13, a maximum extent on the localized object or probe illumination is found in terms of the other experimental parameters

$$D_{x,y} \leqslant \frac{\lambda z}{2p_{x,y}}. \tag{3.14}$$

3.5 Iterative Phase Retrieval in CDI

Over the past 70 years, the initial ideas of phase retrieval have been adapted and expanded into a formulation as a non-convex optimization problem [104] . The algorithms in modern phase retrieval problems typically take the form of iterative projections (or reflections) onto constraint sets in reciprocal spaces where some knowledge about the object is known and enforced. This process continues iteratively until come convergence criteria is met – i.e. some residual error metric is below a preset threshold or the algorithm has run for a pre-defined number of iterations. A brief introduction and overview of these algorithms is given here. For a more in-depth analysis the reader is referred to [105, 106].

3.5.1 Constraint Sets and Generalized Projections

When formulating a phase retrieval algorithm, it is useful to understand the spaces and sets typically involved. Consider an image with N complex-valued pixels. This image can be represented as a complex vector $\boldsymbol{\nu}$ in an N-dimensional Euclidean space V_N. The Fourier transform of this vector $\tilde{\boldsymbol{\nu}}$ is also contained with V_N as the dimensionality of $\boldsymbol{\nu}$ is preserved under the Fourier transform. The Fourier transform acts as a rotation within V_N with the magnitude of $\boldsymbol{\nu}$ preserved due to Parseval's Theorem [98].

Within this space, constraint sets in both real and reciprocal space are expressed as the set of all points contained in V_N where the image satisfies the corresponding constraint. In CDI,

one of these constraint sets C_A is known as the amplitude constraint or Fourier constraint and consists of the set of all images whose Fourier magnitude is equivalent to the one measured during the experiment. The real space constraint can vary depending on the algorithm in use, examples include the non-negativety of real space image pixel value [107], constraints on the image histogram [104], or most commonly the support or isolation constraint [100]. The support constraint C_S is simply a statement that the object is band-limited and thus has been Nyquist sampled in reciprocal space. Formally, the support constraint is a statement what all pixel values are zero outside some defined support region D.

Within this formalism, the phase retrieval problem is cast as finding the image vector $\hat{\boldsymbol{\nu}}$ that is an element of the union between C_A and C_S. The solution is found by starting with a random guess and iteratively projecting between the constraint sets, see Fig. 3.3. For the problem to be uniquely solvable, the constraint sets must intersect at only one point. In practice this is rarely the case due to noisy measurements and other experimental uncertainties.

The generalized projections are mappings from a general image vector ν on to a vector contained in one of the constraint sets ς such that $|\nu - \varsigma|$ is minimized [108]. Practically, this simply means that the vector ν is mapped to the closest point in the constrain set C when a projection is applied. The projection operation for the support constraint is applied to the real space representation of ν and is given by

$$\Pi_S \{\nu_x\} = \begin{cases} \nu_x \, , \, x \in D \\ \\ 0, \text{ else.} \end{cases} \tag{3.15}$$

Practically, this projection amounts to setting the values of ν to zero outside some defined support D.

The projection onto the amplitude constraint set C_A is best performed in Fourier space. Given the measured Fourier intensity values I, the amplitude projection is given by $\Pi_A \{\nu\} =$

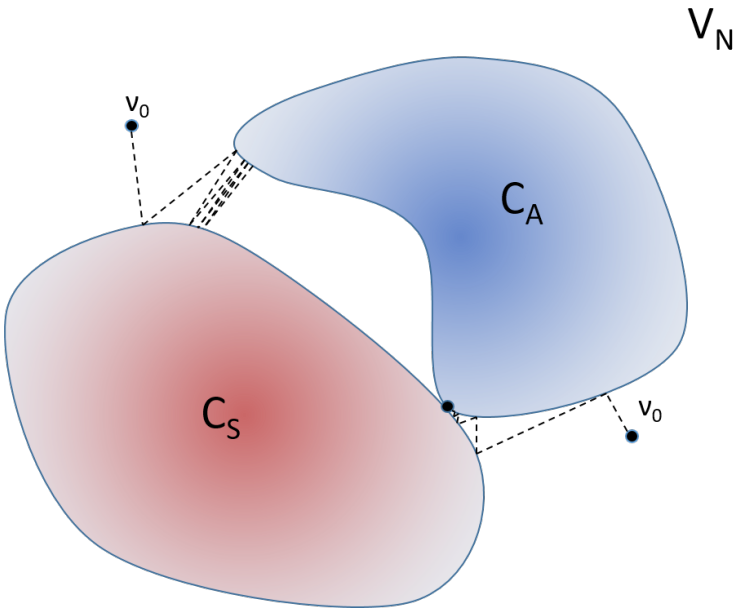

Figure 3.3: **Generalized Projection Algorithm**. A representation of a generalized projection phase retrieval algorithm. An image vector ν_0 is initialized an some point in V_N and iterative projections on to the Fourier amplitude constraint set C_A and the finite support constraint set C_S are performed until convergence. It can be seen that the convergence behavior depends on where the algorithm is initialized.

$\mathcal{F}^{-1}\{P_A\{\mathcal{F}\{\nu\}\}\}$ with

$$P_A\{\tilde{\nu}\} = \begin{cases} \sqrt{I}\frac{\tilde{\nu}}{|\tilde{\nu}|}\,, \nu \neq 0 \\ \sqrt{I}\,, \text{else.} \end{cases} \tag{3.16}$$

This operation replaces the Fourier amplitude of the vector ν with that of the measured values $\sqrt{I}$ while preserving the updated phase values of $\tilde{\nu}$. Issues with the convergence of these algorithms largely stem from this projection operation, which can be multivalued when $\tilde{\nu} = 0$. This is seen when the projection is view in the complex plane in Fig. 3.4. The measured amplitude defines a circle in this plane and projections for nonzero ν are defined by picking the closest point on this circle to ν. However if $\nu = 0$, the all points on the circle are equally distant and the projection is multivalued. The nonuniqueness of this projection is a result of the nonconvexity of the amplitude constraint and makes analyzing the convergence behavior of these algorithms difficult to predict [105, 106]. This is illustrated in Fig. 3.3 where the convergence of the algorithm is seen to depend

on the initialization.

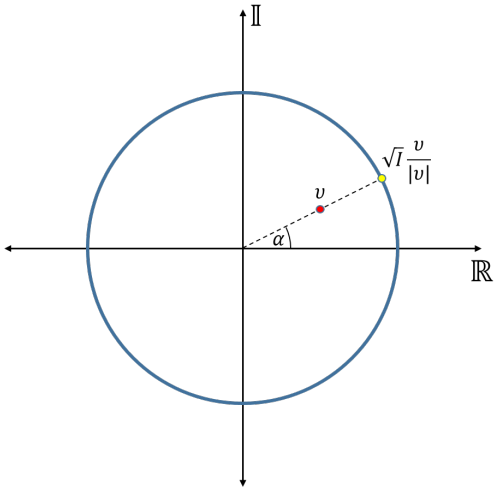

Figure 3.4: **The Fourier Amplitude Projection**. The measured Fourier amplitudes $\sqrt{I}$ define a circle in the complex plane. The projection operation on the vector ν projects it to the closest point on the circle, while preserving its phase defined by angle α. If $\nu = 0$ then the projection operation is not well defined. Adapted from [106].

3.5.2 Phase Retrieval Algorithms

The first algorithm for diffractive imaging was created by Gerchberg and Saxon (GS) [109] and actually predates the early formative conceptual work on CDI and sampling [100, 110]. Still, the GS algorithm provides the general structure that nearly all phase retrieval algorithms still follow, which involves the iterative projection between constraints in reciprocal spaces. The most common algorithms for phase retrieval only differ in their choice of the real space update function using the generalized projection. It is useful to understand the workings of these algorithms in building toward more complicated phase retrieval schemes used in this thesis.

The general flow of a single diffraction pattern phase retrieval algorithm is shown in Fig. 3.5 and requires the following steps:

(1) Initialize an guess for the two dimensional image reconstruction $g_0(\boldsymbol{x})$.

(2) Propagate $g_k(\boldsymbol{x})$ the detector plane via a Fourier transform to get $\tilde{g}_k(\boldsymbol{f})$.

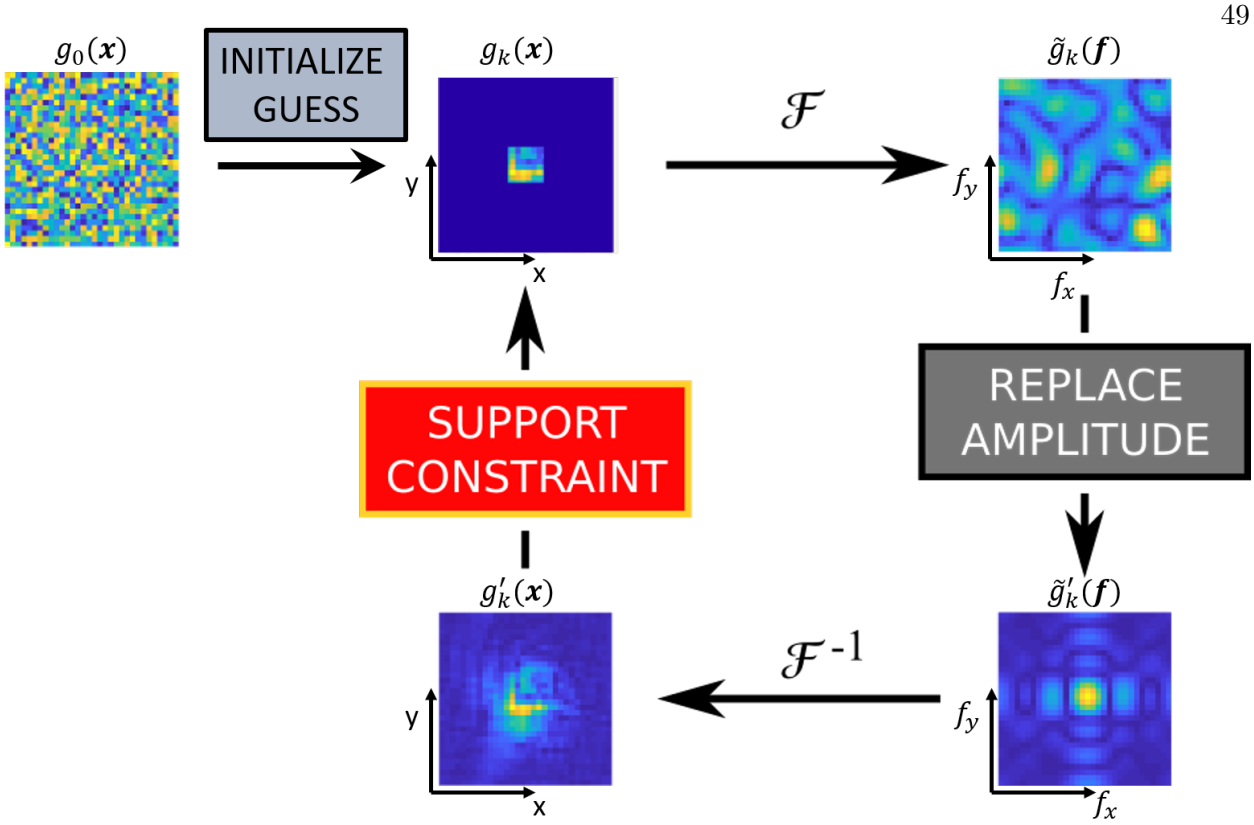

Figure 3.5: **The Error Reduction Algorithm**. The phase of an exit-surface wave is recovered by iteratively enforcing constraints in the object plane (real space) and detector plane (Fourier space). After a random guess is initialized, the wave is numerically propagated to the detector plane where the amplitude of the wave's Fourier transform is forced to match that of the measured data. The updated wave is then propagated back to the object plane where the finite support constraint is enforced, meaning the wave is isolated and of finite extent. This process is repeated until the algorithm converges to a solution. Note that if the support constraint is replaced with some more general real space update condition, then this diagram generalizes to many different phase retrieval algorithms.

(3) Apply the amplitude constraint to find $\tilde{g}'_k(\boldsymbol{f}) = P_A\{\tilde{g}_k(\boldsymbol{f})\}$.

(4) Propagate back to the object plane to obtain $g'_k(\boldsymbol{x})$.

(5) Update the object guess using the algorithm's object update rule to calculate $g_{k+1}(\boldsymbol{x})$.

(6) Repeat (2)-(5) until a suitable solution is found.

The progress of the algorithm is usually monitored using some type of error metric. The

exact metric can vary, but typical choices include a Fourier error

$$\mathcal{E}_F = \frac{\sum \left| |\tilde{g}_k(\boldsymbol{f})| - \sqrt{I} \right|}{\sum \sqrt{I}}, \tag{3.17}$$

where the relative error between the Fourier amplitude of the k^{th} object guess is compared against the measured value. As the algorithm progresses this error metric should, overall, decrease in value. Another useful metric to track is the convergence of the algorithm

$$\mathcal{E}_C = \sum |g_k(\boldsymbol{x})| - |g_{k+1}(\boldsymbol{x})| . \tag{3.18}$$

This metric tracks the relative change in the reconstruction between iteration and gives insight into whether the algorithm has converged or stagnated.

The GS algorithm uses a direct intensity measurement in both the object (real space) and detector (Fourier space) planes. Meaning an amplitude projection is performed in both real and Fourier space. The real space intensity measurement is often difficult to obtain in X-ray and EUV microscopy, but is quite simple in electron microscopy and relatively easy in visible imaging. As such, the GS algorithm has found widespread use for phase-contrast imaging and is still widely used today. It is most interesting here as a precursor for more common phase retrieval algorithms used in CDI.

The error-reduction (ER) algorithm was designed by Fienup, who generalized the GS algorithm by including real space constraints like non-negativity and finite support [107, 111]. While these constraints are implicitly enforced with the real space intensity measurement in GS, removing it was the pivotal step that allowed an object to be reconstructed from only a measurement of its scatter pattern. The object update in ER takes the form $g_{k+1}(\boldsymbol{x}) = \Pi_S\{g_k'(\boldsymbol{x})\}$. This algorithm is easy to implement, but is known to stagnate in local minima during optimization.

One of the most widely used CDI algorithms is Fienup's hybrid input-output (HIO). In his tests, it was determined this algorithm had the best convergence behavior [107]. The object update

rule in HIO is given as

$$g_{k+1}(\boldsymbol{x}) = \begin{cases} g_k^{'}(\boldsymbol{x}), \boldsymbol{x} \in D \\ g_k(\boldsymbol{x}) - \beta g_k^{'}(\boldsymbol{x}), \text{ else,} \end{cases} \tag{3.19}$$

where β is a relation parameter with value $[0.5, 1]$ with $\beta \geqslant 0.9$ a common choice [107, 112].

Since the development of these algorithms, improvements have been made to help their convergence and overcome limitations. One such method is the iterative refinement of the support region – colloquially know as the shrinkwrap algorithm – that was shown to improve convergence speed [112]. Relaxing the requirement for an isolated object to satisfy the finite support constraint were implemented by tightly focusing the illuminating light [113, 114] or masking the illumination close to the sample [115, 116], at the expense of a required known curvature in the illumination and a reduction in flux. Further research into the nature of the algorithms brought improved convergence performance and reconstruction quality with the introduction of more complex operations such as generalized reflections and proximal mappings [117–119].

3.6 Ptychography CDI

The ER and HIO algorithms all require a single diffraction pattern measurement, while GS requires two. While these offer some advantage in terms of required data and relatively low complexity in implementation, it comes at the cost of robustness. These algorithms are prone to stagnation when searching for the optimal solution and there are known ambiguities that are inherent to the algorithms themselves [110, 120]. Many of these issues are overcome if multiple diffraction pattern measurements are used to reconstruct a single image. This scanning modality for CDI is known as ptychography and it has quickly grown to be one of the most wide spread imaging methods in X-ray and EUV microscopy. For an in depth review of the theory and history of the technique, interested readers are referred to [121, 122].

3.6.1 Background

Like single diffraction pattern CDI, ptychography also has its roots in crystallography. The idea was first proposed by Hoppe in 1969, where is was thought that if the Bragg peaks from crystalline diffraction are made to interfere, then information about their relative phases can be learned [123]. However, the Bragg peaks are highly localized in the standard implementation of crystallography so instead of using the usual plane wave illumination, Hoppe suggested that a finite coherent illumination be used instead. By the convolution theorem, the resulting Bragg peaks in the far-field diffraction are convolved with the Fourier transform of the finite illumination. By choosing an appropriate size for the illumination, the interference of neighboring peaks is observed. By recording a second diffraction pattern with the illumination slightly shifted, a unique solution for the phases is recovered. The name "ptychography" was later introduced from the Greek word "ptycho" meaning "to fold" [124–126]. In German, the word for "convolution", "faltung", is the same as "to fold". Ptychography is thus translated as "convolutional imaging".

Initially, the idea received little attention and only a few proof-of-principle studies were performed [127]. The next important milestone was the creation of the Wigner distribution deconvolution method which was the first ptychographic method to reconstruct non-crystalline samples [128]. The technique was successfully implemented with an optical [129] and electron microscope [130], and later using a scanning transmission X-ray microscope [131, 132]. Despite this success, the reconstructed resolution was limited by the relative translation between adjacent positions. So scanning a large field of view with high resolution quickly becomes intractable.

Ptychography CDI began its rapid rise is popularity with the advent of the first ptychographic phase retrieval algorithms [133, 134]. These algorithms are structurally very similar to HIO with several recorded diffraction patterns, however a new and very powerful real space constraint was introduced: the overlap constraint. This novel constraint essentially states that regions of an object illuminated by several different, but overlapping, illumination scan positions must be consistent. Meaning that the object update at different illumination positions are no longer independent. Each

object update benefits from the refinement provided by adjacent position updates, leading to faster algorithm convergence and an increased robustness to noise. Performance was further increased by reformulating the object update function via a gradient-descent optimization routine [135]. This algorithm now known as the "Ptychographic Iterative Engine" (PIE), and its extended form (ePIE) is one of the most popular implementations of ptychography CDI.

Initially, these algorithms required that the illumination function be known *a priori*, but this limitation was subsequently lifted when it was realized that the data redundancy of a ptychographic dataset allowed for the blind deconvolution of the sample transmission function from the illumination [136–138]. This was a key extension that allowed ptychography to become a real alternative to other X-ray microscopy techniques as precise illumination characterization is difficult at these wavelengths.

Since its inception, several improvements have been introduced to the basic ptychography algorithm. Similar to single diffraction pattern CDI, the introduction of advanced optimization routines have seen increased performance and convergence [139–143]. Fermat spiral scanning patterns are now standard to combat the known "raster grid pathology" [137, 144]. Methods for refining the scan grid positions during image reconstruction alleviate some of the strict requirements of system mechanical stability [145, 146]. Continuous scanning modes allow for multiple scan position to be multiplexed into a single diffraction measurement, reducing data volume [147–151]. The illumination of a ptychography microscope can be carefully engineered to allow for the entire dataset to be captured in a single exposure, though at the cost of a reduced spatial resolution [152, 153]. The coherence requirements of ptychography have also been relaxed to allow for hyperspectral and multimode imaging, this will be discussed in detail in chapter 4.

By exploiting the high amount of data redundancy in the ptychography dataset, low frequency information lost when recording data with a beam block can be recovered [154]. Similarly, the resolution of a ptychographic reconstruction can be enhanced by computationally increasing the NA of the recorded diffraction [155]. Even the strict oversampling requirement, a necessary condition in all other forms of CDI, can be relaxed in ptychography [156, 157].

Ptychography is used to study three dimensional systems by combining the technique with tomography [91, 158–160] and by incorporating multiple scattering effects into the reconstruction algorithm [48, 90, 161–163]. Recently these two method have been combined for improved reconstruction quality [164, 165]. Finally, ptychographic CDI has been implemented in a reflection mode for high-resolution surface microscopy [41–43, 69, 166].

3.6.2 The Ptychography Dataset

The dataset for ptychography consists of N diffraction patterns I_n collected by scanning a finite illumination function, $P(\boldsymbol{x})$ – the "probe" function – across an object transmission function $O(\boldsymbol{x})$, previously discussed in section 1.3. Diffraction is recorded at scan positions $\boldsymbol{x}_n = [x_n, y_n]$. The diffraction patterns are given as

$$I_n = \left|\mathcal{F}\left\{O(\boldsymbol{x})\, P(\boldsymbol{x} - \boldsymbol{x}_n)\right\}\right|^2, \tag{3.20}$$

where Fraunhofer propagation has been used, though Fresnel or another suitable propagation method can be substituted.

It is important that the scan positions $\boldsymbol{x}_n$ are chosen such that adjacent scan position have a high degree of overlap in the illuminated area of the sample, typically between 60% - 70%. This overlap introduces redundancy into the dataset and makes the reconstruction process more robust [136]. In the literature, the exit surface wave $\psi_n(\boldsymbol{x}) = O(\boldsymbol{x})\, P(\boldsymbol{x} - \boldsymbol{x}_n)$ is often introduced and represents the wave field directly behind the object. The diffraction patterns I_n and scan grid $\boldsymbol{x}_n$ are used as inputs to the reconstruction algorithm.

3.6.3 The Ptychography Phase Retrieval Algorithm

Similar to the single diffraction pattern phase retrieval algorithms detailed in section 3.5.2, ptychography phase retrieval algorithms alternate between real and reciprocal space where constraints are enforced on an iteratively updated object and probe guess. The reciprocal space constraint is identical to Eqn. 3.16 and it is enforced with each recorded diffraction pattern in-

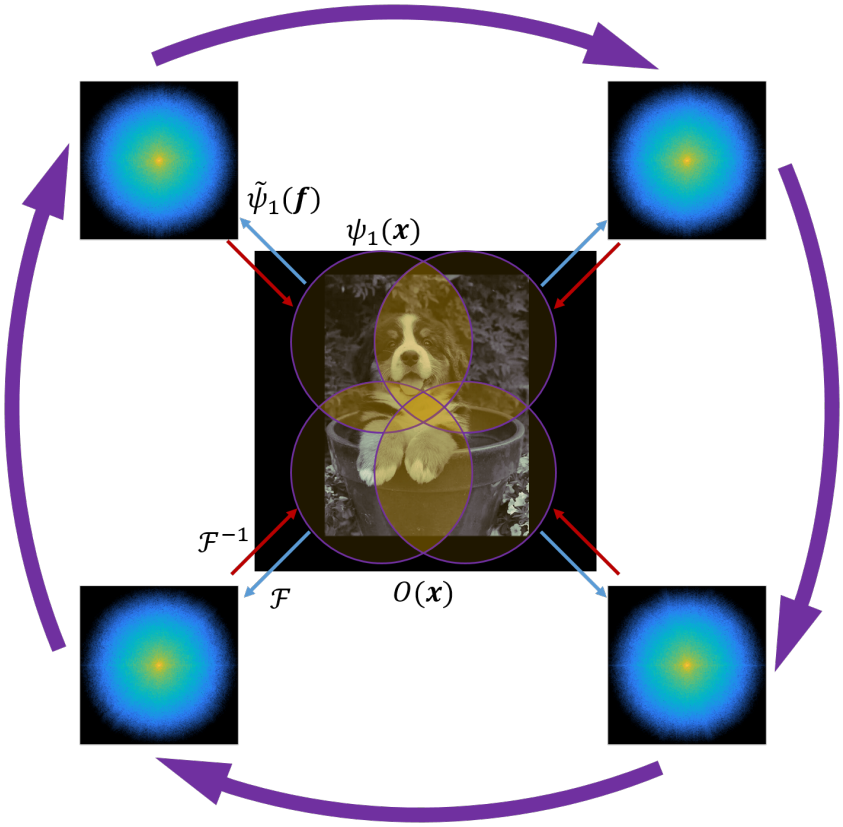

Figure 3.6: **Schematic of a Ptychography Algorithm**. The ptychography algorithm is summarized with a data set containing four diffraction patterns collected with a circular scan over four overlapping positions. The algorithm iterates of the different scan positions in the outer loop (purple arrows). At the n^{th} position, the exit surface wave $\psi_n(\boldsymbol{x}) = O(\boldsymbol{x})\, P(\boldsymbol{x} - \boldsymbol{x}_n)$ is calculated. An updated guess of the exit wave is calculated after applying the Fourier amplitude constraint by propagating $\psi_n(\boldsymbol{x})$ to the detector (red and blue arrows). From this, an updated guess at the object and probe is made. The algorithm then moves to position $n+1$ and repeats the process. However, the overlap between adjacent position means that the next position's update benefits from the previous positions. Figure is adapted from [167].

dividually. The object space update is less obvious. There are numerous algorithms available for ptychography, which mainly differ in their object update function and whether the different scan positions are processed serially or in parallel [136, 137, 139].

Work in this thesis is mainly based on the ePIE algorithm, which is a serialized gradient-descent based optimization method. Serialized versions of ptychography are observed to have faster convergence behavior, at the cost of being more susceptible to stagnation in local minima. This

stagnation is largely due to the serial nature of the algorithm; a parallel implementation is trying to globally optimize the entire image simultaneously, while serial versions optimize sub regions of the image sequentially. The serial ePIE algorithm is summarized here following [136], but many of its properties are generalizable to other ptychography reconstruction algorithms.

The set of measured intensities I_n, scan positions $\boldsymbol{x}_n$, and object and probe function initializations $O^{(0)}(\boldsymbol{x})$ and $P^{(0)}(\boldsymbol{x})$ are required as inputs to the reconstruction algorithm. The updated object $O^{(j+1)}(\boldsymbol{x})$ and probe $P^{(j+1)}(\boldsymbol{x})$ are then calculated with the following steps:

(1) For position n, calculate the ESW $\psi_n^{(j)}(\boldsymbol{x}) = O^{(j)}(\boldsymbol{x})P^{(j)}(\boldsymbol{x}-\boldsymbol{x}_n)$.

(2) Propagate the ESW to the detector to find $\tilde{\psi}_n^{(j)}(\boldsymbol{f}) = \mathcal{F}\left\{\psi_n^{(j)}(\boldsymbol{x})\right\}$.

(3) Apply the amplitude constraint by replacing the Fourier modulus $|\tilde{\psi}_n^{(j)}(\boldsymbol{f})|$ with the measured intensity amplitude $\sqrt{I_n}$.

$$\psi_n'^{(j)}(\boldsymbol{x}) = \mathcal{F}^{-1}\left\{\sqrt{I_n}\frac{\tilde{\psi}_n^{(j)}(\boldsymbol{f})}{|\tilde{\psi}_n^{(j)}(\boldsymbol{f})|}\right\}. \tag{3.21}$$

(4) Propagate the updated ESW back to the object plane to calculate $\psi_n'^{(j)}(\boldsymbol{x}) = \mathcal{F}^{-1}\left\{\tilde{\psi}_n'^{(j)}(\boldsymbol{f})\right\}$.

(5) Use the updated ESW to find $O^{(j+1)}(\boldsymbol{x})$ and $P^{(j+1)}(\boldsymbol{x})$ with update conditions

$$\begin{aligned} P^{(j+1)}(\boldsymbol{x}) &= P^{(j)}(\boldsymbol{x}) + \alpha\frac{O^{(j)*}(\boldsymbol{x}+\boldsymbol{x}_n)}{\left|O^{(j)}(\boldsymbol{x}+\boldsymbol{x}_n)\right|^2}\left(\psi'^{(j)}(\boldsymbol{x}) - \psi^{(j)}(\boldsymbol{x})\right), \\ O^{(j+1)}(\boldsymbol{x}) &= O^{(j)}(\boldsymbol{x}) + \alpha\frac{P^{(j)*}(\boldsymbol{x}-\boldsymbol{x}_n)}{\left|P^{(j)}(\boldsymbol{x}-\boldsymbol{x}_n)\right|^2}\left(\psi'^{(j)}(\boldsymbol{x}) - \psi^{(j)}(\boldsymbol{x})\right). \end{aligned} \tag{3.22}$$

(6) Move to scan position $\boldsymbol{x}_{n+1}$ and repeat steps (1)-(5). The shifted probes at $P^{(j)}(\boldsymbol{x}-\boldsymbol{x}_n)$ and $P^{(j)}(\boldsymbol{x}-\boldsymbol{x}_{n+1})$ should overlap and constrain the regions of the object present in both illumination positions.

(7) Continue iterating through all N positions to complete one full update iteration for the entire scanned object area.

The parameters α and β in Eqn. 3.22 are relaxation parameters similar to β in the HIO algorithm. Typically their values are set in the range $[0.9, 1]$ and control the step size in the

gradient optimization. To avoid the possibility of dividing by zero, the denominator in Eqn. 3.22 is converted to the maximum value of the object or probe function. An error metric is usually defined to monitor the algorithm progress, with a common choice being the RMS error between the measured diffraction amplitude and the algorithm's current guess for the diffraction amplitude.

Chapter 4

Spatial, Spectral, and Polarization Multiplexing in Ptychography

4.1 Introduction

Since its initial rediscovery, the scope of ptychography has been extended to simultaneously reconstruct several different incoherent object and/or probe modes with no increase in the data acquisition volume [168, 169]. An incoherent superposition of diffraction from multiple modes is recorded on a detector during a ptychography scan and computationally separated during reconstruction. This technique, known as multiple mode ptychography or ptychographic multiplexing, is reviewed below. Later, it is shown that by introducing spatial separation between mutually incoherent modes, the field of view of ptychography reconstructions can be expanded without sacrificing spatial resolution. Results discussed here are previously published in [170].

4.2 Multiple Mode Ptychography

Multiple mode ptychography was first derived to account for the complication of decoherence during the imaging process [169]. The high coherence requirements for CDI imposes strict constraints on the experimental setup, such as negligible vibrations of mechanical components, a stationary sample or sufficiently short ultrafast pulses from the source, and a highly monochromatic source. These competing requirements often lead to a reduction in the usable coherent flux in a given system. Thus, relaxing the coherence needs of a CDI algorithm directly leads to an easing of experimental design. Later, the idea of multiple mode ptychography was expanded to allow for spectrally sensitive objects and polychromatic illuminating probes [168].

Regardless of the particular source of decoherence the algorithm is attempting to compensate, the basic formulation of multiple mode ptychography remains the same. Namely, in a system with some type of decoherence – source stability, mechanical vibrations, or source polychromaticity – the measured diffraction pattern is treated as an incoherent sum of several mutually incoherent modes with

$$I_j\left(\boldsymbol{f}\right) = \left|\mathcal{F}\left\{\psi_1\left(\boldsymbol{x}-\boldsymbol{x}_j\right)\right\} + \mathcal{F}\left\{\psi_2\left(\boldsymbol{x}-\boldsymbol{x}_j\right)\right\} + \ldots + \mathcal{F}\left\{\psi_N\left(\boldsymbol{x}-\boldsymbol{x}_j\right)\right\}\right|^2, \tag{4.1}$$

where $I_j\left(\boldsymbol{f}\right)$ is the j^{th} measured intensity scatter pattern, ψ_n is the exit-surface wave corresponding to the n^{th} incoherent mode, N is the total number of incoherent modes modeled in the system. The multiple mode ptychography algorithm leverages differences in the diffraction produced from each mode – from either a mode-specific object response or probe profile, or differing scattering angles due to various wavelengths in the probe – to tease apart the contributions of each mode to the sum total recorded on the detector. An error metric E is defined that takes into account multiple incoherent modes and is minimized using a gradient descent optimization with

$$E = \sum_j \left[\left(\sum_n \left|\tilde{\psi}_{j,n}\left(\boldsymbol{f}\right)\right|\right) - \left|I_j\left(\boldsymbol{f}\right)\right|\right]^2, \tag{4.2}$$

where $\tilde{\psi}_{j,n}\left(\boldsymbol{f}\right) = \mathcal{F}\left\{\psi_n\left(\boldsymbol{x}-\boldsymbol{x}_j\right)\right\}$. This is similar to the error metric used for ePIE [136], but with an additional summation over all the incoherent modes. The object and probe update rules for multiple mode ptychography are similarly modified to take into account the presences of the multiple incoherent modes. The real space update condition for the $k+1$ iteration of the probe and object at the j^{th} scan position and n^{th} incoherent mode are given by

$$\begin{aligned} P_{n,j+1}^{k+1}\left(\boldsymbol{x}\right) &= P_{n,j}^{k}\left(\boldsymbol{x}\right) + \alpha\frac{O_n^{k\,*}\left(\boldsymbol{x}-\boldsymbol{x_j}\right)}{\left|O_n^k\left(\boldsymbol{x}-\boldsymbol{x_j}\right)\right|^2}\left(\psi_{n,j}^{k\prime}\left(\boldsymbol{x}\right) - \psi_{n,j}^{k}\left(\boldsymbol{x}\right)\right) \\ O_{n,j+1}^{k+1}\left(\boldsymbol{x}\right) &= O_{n,j}^{k}\left(\boldsymbol{x}\right) + \beta\frac{P_n^{k\,*}\left(\boldsymbol{x}+\boldsymbol{x_j}\right)}{\left|P_n^k\left(\boldsymbol{x}+\boldsymbol{x_j}\right)\right|^2}\left(\psi_{n,j}^{k\prime}\left(\boldsymbol{x}\right) - \psi_{n,j}^{k}\left(\boldsymbol{x}\right)\right), \end{aligned} \tag{4.3}$$

where $\psi'_{n,j}\left(\boldsymbol{x}\right)$ is the j^{th} Fourier amplitude updated exit-surface wave of the n^{th} mode. The Fourier amplitude update rule is also modified to take into account the incoherent sum of mode intensities

measured during an experiment. The modulus update rule is now given by

$$\psi_{n,j}^{k\prime}(\boldsymbol{x}) = \mathcal{F}^{-1}\left\{\frac{\sqrt{I_j(\boldsymbol{f})}}{\sqrt{\sum_n \left|\tilde{\psi}_{n,j}^{k}(\boldsymbol{f})\right|^2}}\tilde{\psi}_{n,j}^{k}(\boldsymbol{f})\right\}. \tag{4.4}$$

Eqns. 4.3 and 4.4 are applied sequentially as the scan positions and multiple modes are looped through, forming one complete iteration of the multiple mode ptychography algorithm. Like single mode ptychography, this algorithm can be formulated to run with either a parallel or serial update condition and similarly takes on the various advantages and setbacks associated with each. The multiple mode ptychography imaging modality has been successfully used to perform hyperspectral imaging with EUV light [171], to relax the monochromaticity requirement with both optical and EUV light [172, 173], measure the unique phase structure of vortex beams [174], characterize the coherence of X-ray beams generated from synchrotron sources [175], and investigate dynamic systems [176], among other applications [177].

4.3 Spatial Separation of Mutually Incoherent Probes

In the original formulations of multiple mode ptychography, the mutually incoherent modes were assumed to spatially overlap with one another on the sample. However, this spatial overlap is not required or imposed by the ptychography algorithm. With this in mind, multiple mode ptychography can be employed to image separate locations of a sample simultaneously, as long as the multiple illuminating probes are mutually incoherent with each other, i.e. non-interfering at the detector plane.

Imaging in this modality allows for a larger field of view in the reconstructed image with no loss in spatial resolution. The mutual incoherence of the probes can be obtained in a number of ways. The following sections detail proof-of-principle experiments where the incoherence is achieved using probes of different wavelengths (sec. 4.3.1), with orthogonal polarization states (sec. 4.3.2), and an ongoing experiment where the probes are delayed temporally (sec. 4.3.3).

4.3.1 Spectral Multiplexing with Spatially Separate Beams

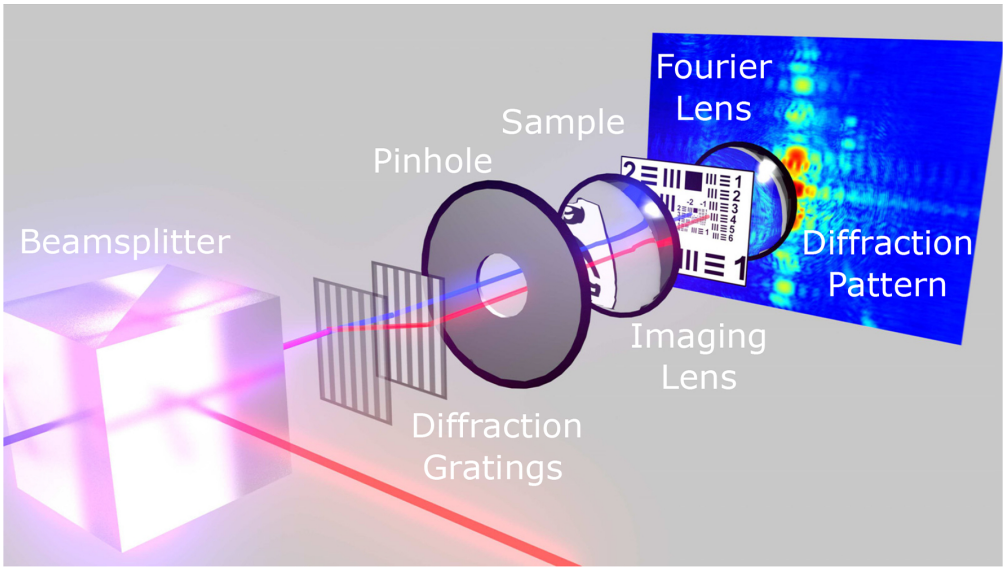

Figure 4.1: **Spatially Separated, Spectrally Multiplexed Ptychography Experiment Setup**. A schematic for the visible ptychography microscope that uses two illuminating probes of different wavelengths that are spatially separate. The different colored probes are combined with a beamsplitter and then spatially offset using a pair of diffraction gratings. The additional diffraction orders are blocked by a pinhole. The two unblocked beams propagate parallel to each other and are imaged onto a 1951 USAF test pattern sample. The diffracted light is focused onto a detector where the overlapping, non-interfering diffraction patterns are collected. Schematic is not to scale. Reproduced from [170].

In this initial proof-of-principle, a transmission-mode, visible ptychography microscope with two spatially and spectrally separate beams was constructed, as shown in Fig. 4.1. Two monochromatic, fiber-coupled laser diodes [Blue Sky Research, FTEC2 440-20, $\lambda = 420$ nm and FTEC2 658-60, $\lambda = 658$ nm] are combined using a beam-splitting cube [Thorlabs, BS013] causing both beams to propagate collinearly. The beams then pass through a pair of diffraction gratings [Rainbow Symphony, 01604, 500 lines/mm] which gives the beams a horizontal offset while keeping them parallel with each other. The additional diffraction orders are blocked by a 300 μm pinhole after the second diffraction grating. The beams are imaged onto the sample through an imaging system with a demagnification of M = 0.1. The sample used in this experiment is a negative 1951 USAF resolution test target [Thorlabs, R3L3S1N]. The diffracted light subsequently passed through a

Fourier transform lens with f = 2 cm, which focused the light on a CMOS detector [Mightex, SCN-B013-U].

Diffraction patterns were collected in 10 x 10 semi-random rectilinear scan grid, with approximately 60% overlap between adjacent positions. Multiple exposures were captured at each scan position with exposure times ranging from 0.05 ms - 750 ms and frames were combined to extend the dynamic range of the detector. The composite diffraction patterns were shifted to the center of the numeric grid using a center of mass of the two DC peaks of the constituent diffraction patterns, which were separated due to chromatic aberration in the transform lens. Using the multiple mode ptychography algorithm described in [168], and two objects corresponding to different areas of the sample were reconstructed for each probe wavelength, shown in Fig. 4.2.

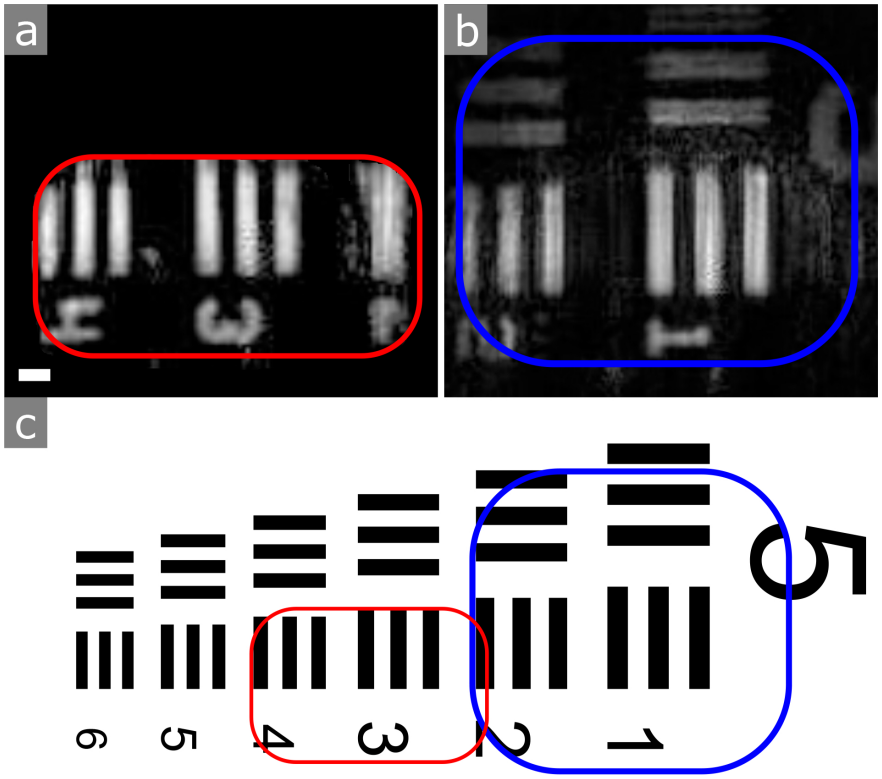

Figure 4.2: **Object Reconstructions from Spatially Separated, Spectrally Multiplexed Ptychography**. Reconstructed objects for the red (a) and blue (a) probe beams in the spectrally multiplexed ptychography experiment. Scale bar is 20 μm and the scale is equivalent in (a) and (b). (c) Relative locations of the imaged areas on a USAF Resolution Test Target. The two areas are separated by 175 μm, which is the same as the measured separation between the probes. Reproduced from [170].

To verify the accuracy of the image reconstructions, the two illuminating beams were directly imaged by translating the detector to the sample plane. The reconstructed objects in Fig. 4.2 correspond to areas on the sample separated by 175 ± 5 μm. This agrees with the directly-imaged probes on the detector, having a measured separation of 179 ± 5 μm. A further verification was performed by computationally propagating the reconstructed probes for each wavelength to the image plane of the imaging lens in the experiment. The resulting beams are show in Fig. 4.3. The blue probe had to be propagated further in order to reach the imaging plane. The difference between the two image planes of the different colored probes was numerically determined to be 550 ± 100 μm. This agrees with the calculated value of 420 ± 4 μm for chromatic aberration of the imaging lens for the two wavelengths used in the experiment.

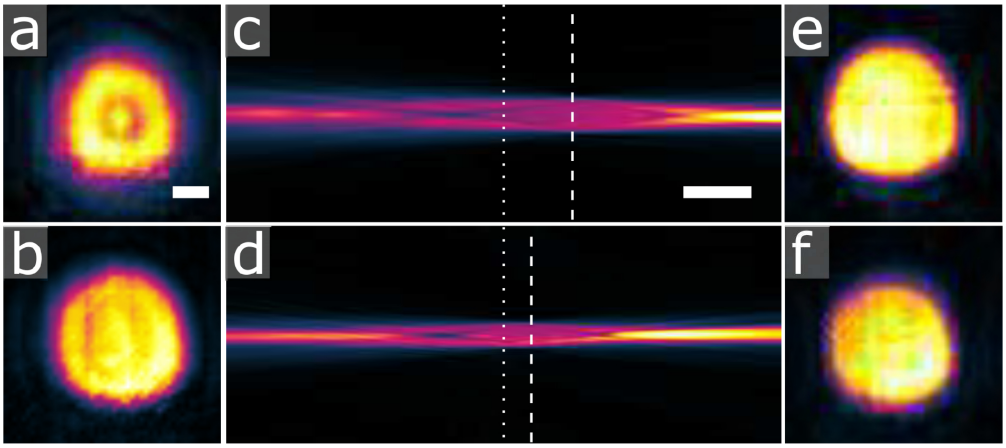

Figure 4.3: **Chromatic Aberration of Spectrally Separate Probes**. The amplitudes of the blue (a) and red (b) beam recovered from the multiple mode ptychography reconstruction. The propagation of the blue (c) and red(d) probes along the optical axis of the experiment. The white dotted lines indicate the location of the reconstructed probes, while the dashed white lines indicate the actual focal plane of the different colored probes. A transverse profile of the probe beams in the blue (e) and red (f) image plane, obtained from computation propagation of the reconstructed probes. The difference between the image planes of the different colored probes is consistent with chromatic aberration expected from the imaging lens in the system. The scale bar in (a) is 20 μm and is shared with (b), (e), and (f). The scan bar in (c) is 1 mm and is shared with (d). Reproduced from [170].

4.3.2 Polarization Multiplexing with Spatially Separate Beams

In the previous section, separate wavelengths were used to so that the there was no interference between the beams on the detector and a multiple mode ptychography algorithm could be used. However, this is not the only way to remove this interference; any mutually incoherent modes will suffice [169]. In this section, ptychographic multiplexing is demonstrated using orthogonally polarized probe modes. In this setup, depicted in Fig. 4.4, a single red ($\lambda = 658$ nm) was spatially split into two orthogonal polarization states using a beta barium borate (BBO) crystal [Eksma Optics, 9830; 2.7 mm thickness, $\theta = 23.4$, $\phi = 90$] before illuminating a two spatially separated portions of a negative USAF resolution test target [Thorlabs, R3L3S1N]. The scattered light was collected by a lens (f = 2 cm) placed 2 cm after the sample, which focused the light onto a CMOS detector.

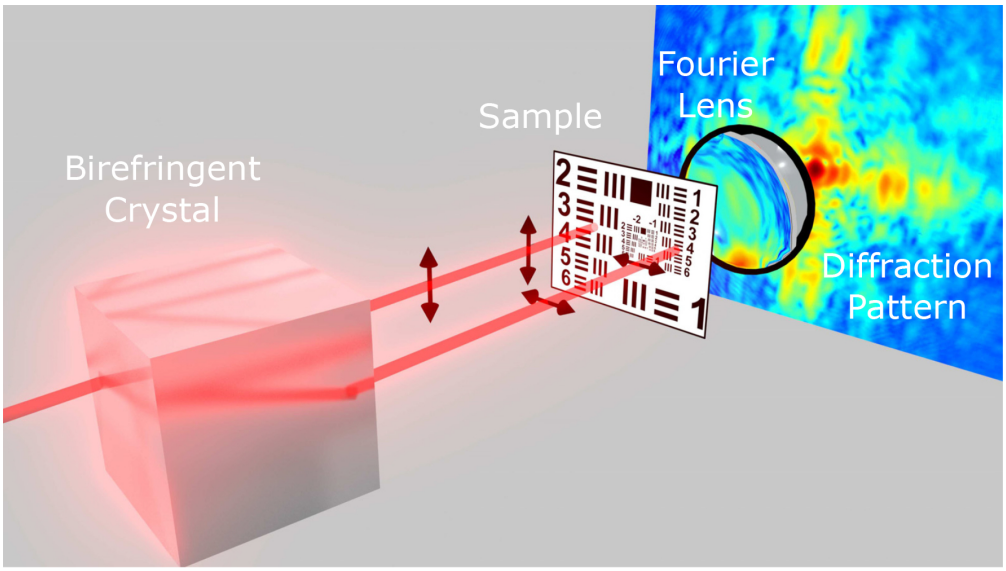

Figure 4.4: **Spatially Separated, Polarization Multiplexed Ptychography Experiment Setup**. A schematic depiction of the visible, transmission-mode ptychography experiment using two spatially separated probes with orthogonal polarization states. The beam from a single red ($\lambda = 658$ nm) laser diode is split into two orthogonally polarized beams using a birefringent crystal. The beams are then incident on a USAF resolution test target and the scattered light is collected by a Fourier transform lens that forms a diffraction pattern on a pixelated detector. Reproduced from [170].

By directly imaging the two beams at the sample plane, the separation between the two beams

was measured to be 216 ± 20 μm. The directly imaged beams are shown in Fig. 4.5. Without the spatial separation between the beams, the sample would produce identical diffraction patterns for both polarizations. In the case where a sample does not have a polarization-dependent optical response, the spatial separation between the beams allows the orthogonally polarized modes to be deconvolved without any ambiguity.

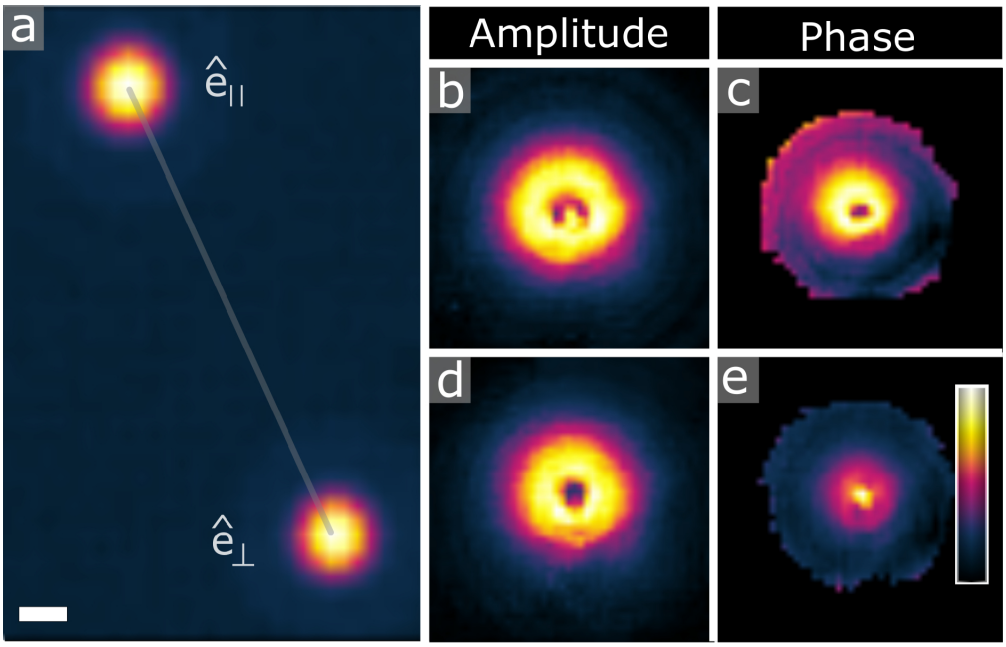

Figure 4.5: **Measured and Reconstructed Spatially Separated, Orthogonally Polarized Probes**. (a) A Direct image of the orthogonally polarized, spatially separated probes used in sample plane of the experiment. The separation between the beams is 216 ± 20 μm. (b-c) The reconstruction of the $\hat{e}_{||}$ polarized beam in both amplitude and phase. (d-e) The reconstruction of the $\hat{e}_{\perp}$ probe in amplitude and phase. The scale bar is 20 μm in (a) and the scale is equivalent in (a-e). Reproduced from [170].

A 64 position ptychography scan was taken with both beams incident on the sample. Data were collected and pre-processed using an approach identical to the one described in sec. 4.3.1. The successful reconstruction is shown in Fig. 4.6. The two reconstructed areas show that the parallel polarized probe scanned a region of group 6 and the perpendicular polarized probe scanned group 7 on the USAF resolution test pattern. Locating these areas on the sample shows that the separation between the two regions is 170 ± 20 μm, which is consistent with the separation measured in a

direct imaged of the beams at the sample plane.

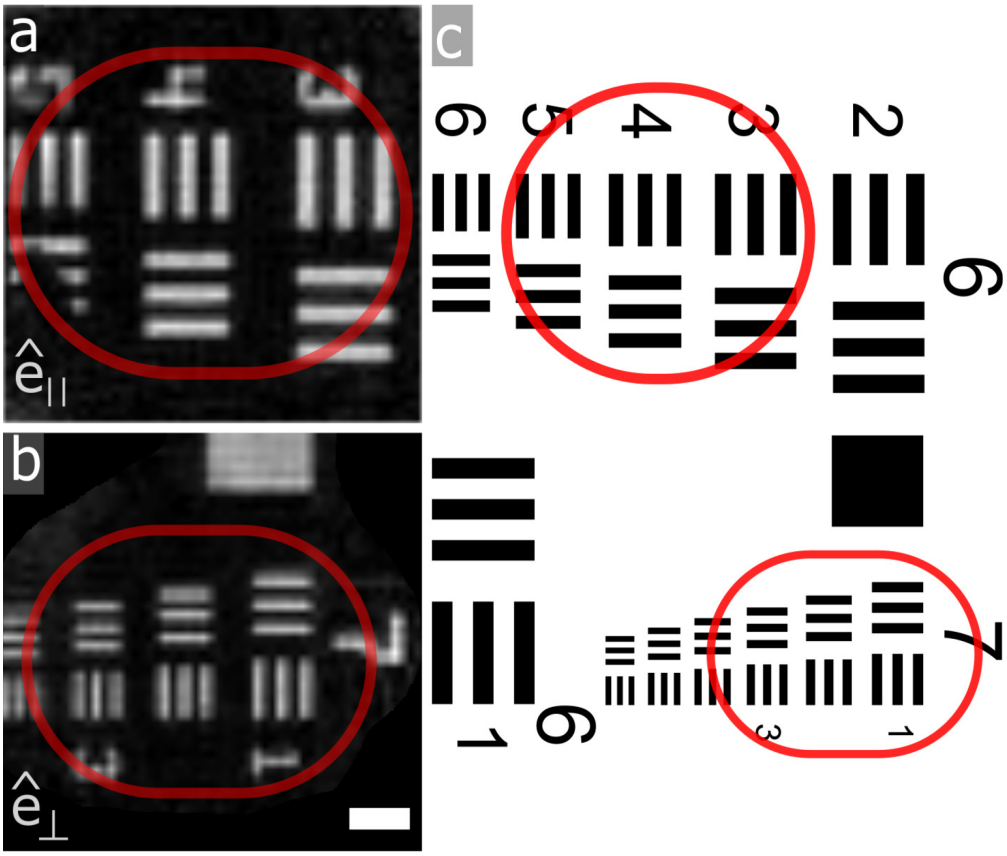

Figure 4.6: **Orthogonally Polarized Reconstructions with Spatially Separate Beams**. The left column shows the amplitude reconstructions for the parallel (a) and perpendicular (b) polarized beams. (c) The location of the relative position of the scanned region on the USAF resolution test target. The two areas are separated by 170 ± 20 μm, which corresponds to the measured separation between the two probes. The scale bare in (a) is 20 μm and is shared with (b). Reproduced from [170].

In Fig. 4.5(b), group 7, subgroup 5 of the USAF resolution test target is resolved, indicating an upper bound for the microscope resolution of 2.46 μm, which is equivalent to the Abbe resolution limit for this microscope system. This indicates that using multiple beams for ptychography has no adverse effect on the achievable spatial resolution of an multiplexed ptychographic imaging system.

4.3.3 Temporal Multiplexing with Spatially Separate Beams

When performing ptychography with a pulsed source, it is possible to temporally multiplex information from the interaction of the sample with several pulses into a single detector exposure that is much longer than the individual pulse length or repetition rate of the system. Because consecutive pulses in the pulse train are temporally isolated, they will never arrive at the detector at the same time, and thus cannot interference. If the detector is allowed to expose such that it will integrate over pulses, then the recorded diffraction pattern can be treated as an incoherent sum of the signals produced from each pulse. Hence, the model of ptychographic multiplexing can be applied to this system where each time delayed pulse is treated as a single mutually incoherent mode.

Configuring an ptychography imaging system to make use of temporal multiplexing unlocks the potential for studying spatially resolved system dynamics without increasing the data volume or acquisition time. Alternatively, if a sample of interest is static, then temporal multiplexing can be used to perform multiple mode ptychography with probes that are otherwise identical (i.e. spectrally, polarization, etc.).

Modern research continues to push the development of coherent high energy systems that use geometries with more than one beam [178, 179]. Combining these novel sources with spatially separated multiple mode ptychography, the benefits of imaging with higher energy sources - high resolution and chemical sensitivity - is possible with higher throughput. Leveraging the naturally pulsed nature of an HHG EUV source, a spatially separated, temporally multiplexed ptychography microscope has been constructed using two time-delayed EUV probes.

In this setup, a bright, phase-matched, fully spatially coherent HHG EUV beam centered at $\lambda = 56$ nm was generated using a custom built HHG source. Harmonics were generated by frequency doubling a pulse train with central wavelength of 790 nm, pulse duration of 45 fs, pulse energy of 8 mJ, and repetition rate of 1 kHz, and focusing the resulting 395 nm, 2 mJ pulses into a 150 μm diameter hollow-core waveguide filled with Ar at a backing pressure of 84 Torr. The HHG process

up converts the wavelength of the driving source into a spectrum of higher energy light, centered at the 7^{th} harmonic (22 eV). After the HHG process, the residual light at the fundamental frequency is absorbed using two 200 μm thick Al filters.

The EUV light is then directed in an imaging chamber where it reflects off of an off-axis toroidal mirror with a focal length of 27 cm and it begins to focus. As the light propagates, the beam is split using the edge of a D-mirror. The divided beams are directed on to two flat mirrors that redirect the beams on to two pinhole masks of diameters 30 μm and 50 μm to clean up the spatial mode and easily identify the different beams during reconstruction. The shaped beams are incident on the sample, which is placed approximately 1 cm after the pinhole mask. The scattered light then propagates 4.6 cm to a pixelated detector where the scatter from both beams is recorded simultaneously. A schematic of the imaging chamber is shown in Fig. 4.7.

The path length traversed by the two different beams differs by 0.3 mm, corresponding to a temporal delay of 10 ps between the two pulses. The pulse duration of the EUV light – limited by the driving laser pulse duration – is only tens of femtoseconds in length, so the pulses are well separated in time at the detector. This allows temporal multiplexing in this setup.

4.4 Discussion and Conclusion

A novel method to increase the throughput of a ptychographic imaging system was demonstrated. By spatially separating probes in a multiplexed ptychography scan, multiple areas of a sample are imaged simultaneously. This increase in throughput does not require a reduction in numerical aperture of either individual probe and therefore preserves the high spatial resolution offered by CDI and is applicable to any set of non-interfering probes. This has been explicitly demonstrated using two probes of different wavelengths and two orthogonally polarized probes of the same wavelength. A further demonstration using temporally offset coherent pulses is currently underway.

This technique is appealing for use with coherent EUV and X-ray sources. In particular, coherent EUV sources generated with HHG are a natural choice as the HHG process produces a

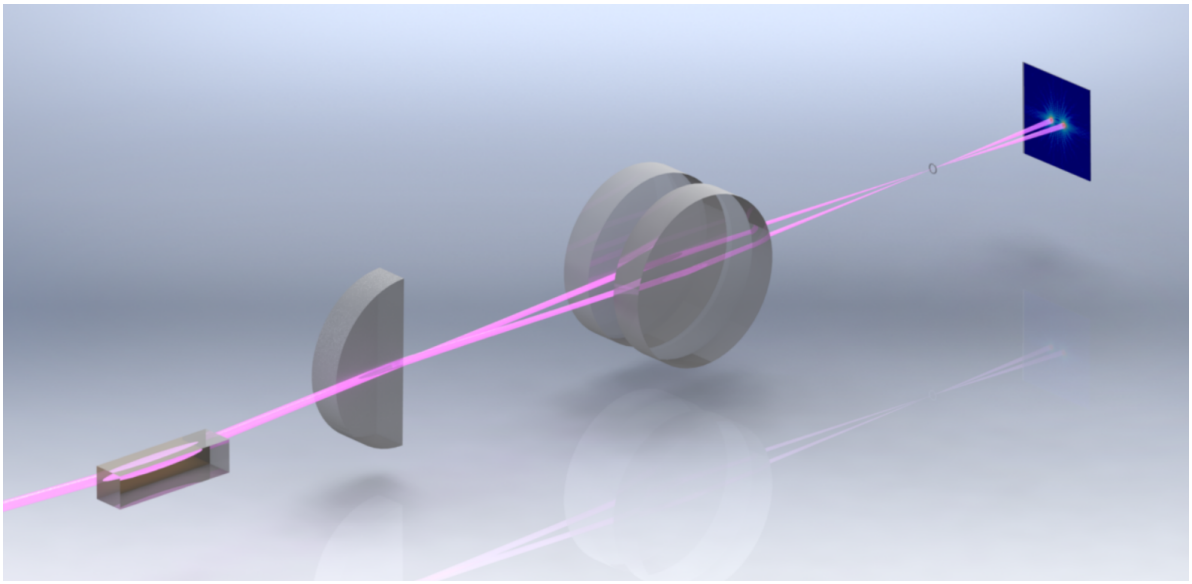

Figure 4.7: **Temporal Multiplexing Multiple Beam Ptychography Setup**. A schematic of the EUV multiple beam ptychography experiment with two temporally offset probes. A single EUV beam ($\lambda = 56.4$ nm) is generated via HHG and then focused by an off-axis toroidal mirror and split by partially reflecting off the edge of a D-mirror. The split beams propagate to two flat mirrors that redirect the beams onto a sample, with a controllable spatial separation. The scattered light from both beams is collected by pixelated detector simultaneously. The path length difference traversed by the different legs of the experiment is 0.3 mm, corresponding to a relative delay of 10 ps, allowing for temporal multiplexing in this setup.

discrete comb of spectrally distinct harmonics, which combine to form extremely sort pulses. With a few additional optics, existing EUV ptychographic imaging systems can be modified to spatially separate these harmonics, or temporally delay two or more pulses, allowing for spectral or temporal multiplexing, respectively.

With the need for simultaneous high resolution and large field of view imaging to fully investigate the relationship between microscopic order and macroscopic function, spatially separate multiple mode ptychography provides a possible path forward. Ideas developed during the proof-of-principle experiments described here are already implemented at the Spring-8 synchrotron source [180].

Chapter 5

Multiple Beam Ptychography with Mutually Coherent Beams

5.1 Introduction

This chapter addresses an extension to the mutually incoherent multiple beam ptychography algorithm discussion during chapter 4. A significant accomplishment of ptychography CDI is its shift of the Nyquist sampleing criteria that previously limited sample size in diffractive imaging systems [95]. It does this by shifting this constraint from the object under investigation to the beam used to probe the system and operating in an area-by-area scanning modality. This allows for an image field-of-view (FOV) that grows with the size of a scan, or number of scan positions. This comes at the cost of increased scan time and data acquisition required to form an image. It is this limited throughput that remains an obstacle for large field-of-view ptychographic imaging.

This chapter presents a diffraction-limited, large FOV ptychographic imaging technique that uses several mutually coherent, spatially separated illuminating probes to scan a sample. This increases the throughput of the microscope by a factor corresponding to the number of probes without increasing data acquisition time or volume. Using an optical transmission mode ptychography CDI microscope, two related but distinct methods are demonstrated. These experiments are carried out on the setup depicted in Fig. 5.1 with various pinhole sizes and separations in the pinhole array. Finally, an analysis of the image fidelity of the reconstructed objects using both multi-beam and single-beam ptychography is presented. These techniques are previously published in [181, 182].

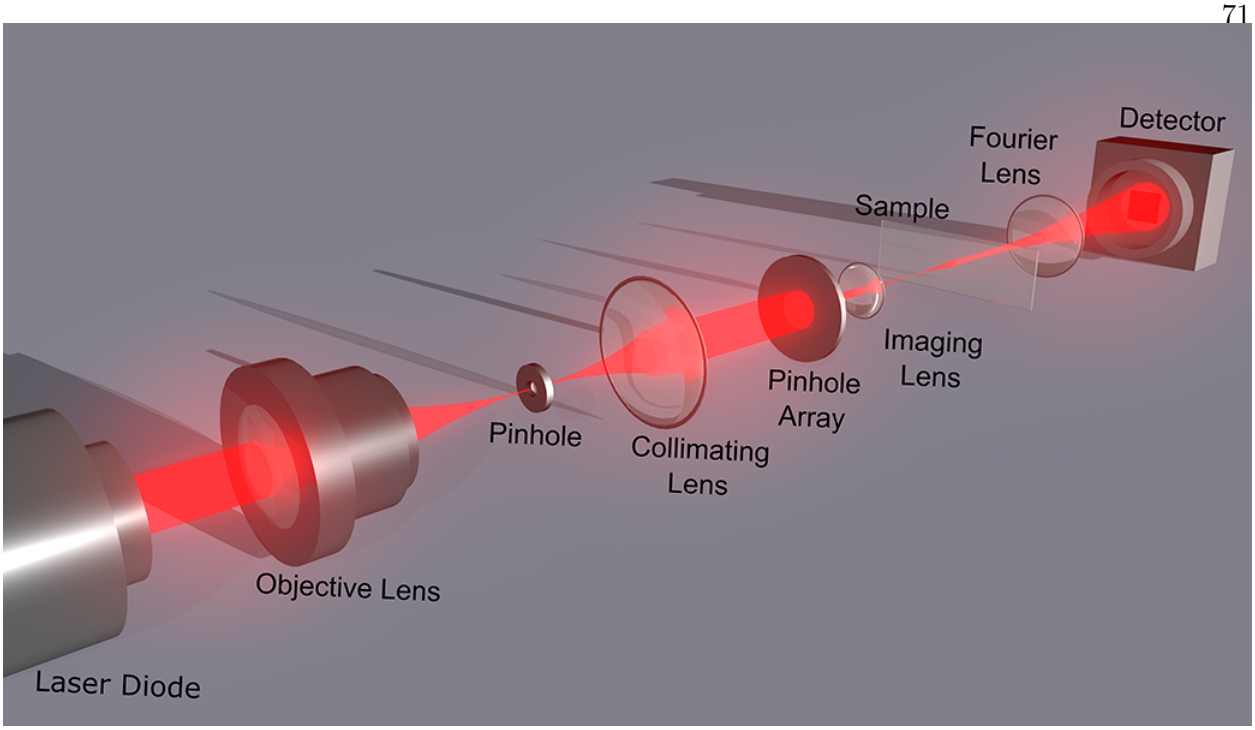

Figure 5.1: **The Experimental Schematic for Multiple Beam Ptychography**. A visible laser diode ($\lambda = 656$nm) is spatially filtered and collimated before it is sent onto a pinhole array. The exact specifications of the pinhole array vary depending on the technique, but it functions to generate multiple mutually coherent probes that are then imaged onto the sample via the imaging lens. A Fourier transform lens is used to propagate the exit wave to the far-field and produce a diffraction pattern that is then recorded by the detector.

5.2 Methods

In ptychography CDI, the illuminating probe is subject to an oversampling constraint [84, 183] that restricts its transverse size. Satisfying the oversampling constraint allows the resulting diffraction intensities to be Nyquist sampled by the detector. When a second illuminating probe is added to the system, interference terms between the two probes are introduced at the detector. Traditional ptychography algorithms interpret these two individual probes as a single illumination function, which greatly restricts the allowable size and separation of the probes on the sample, as the entire probe system must satisfy the oversampling condition.

It is possible to suppress this interference and effectively convert the measured signal to an incoherent sum of the diffraction from all the probes. This suppression can be achieved through

digital filtering of the data after acquisition, which we refer to as autocorrelation filtering in section 5.2.1. In a complementary approach, the experimental parameters can be tuned to naturally remove the interference from the measured signal, which we refer to as alias cloaking in section 5.2.2.

5.2.1 Autocorrelation Filtering

Consider a transmission ptychography experiment with two identical, mutually coherent beams with wavelength λ and finite support incident on an extended sample and separated by a center-to-center distance $\Delta\boldsymbol{x}$. Working in the projection approximation, the exit surface wave just after the sample is given by the sum of the contributions from each probe functions multiplied by the object transmission function, i.e.: $\psi(\boldsymbol{x}) = O(\boldsymbol{x}) P_1(\boldsymbol{x}) + O(\boldsymbol{x}) P_2(\boldsymbol{x} - \Delta\boldsymbol{x})$, where $\psi(\boldsymbol{x})$ is the exit surface wave, $O(\boldsymbol{x})$ is the object transmission function, and $P_n(\boldsymbol{x})$ is the n^{th} probe function. During a scan, a detector positioned in the far-field a distance z away from the sample, will record the intensity of the diffracted wave as

$$I(\boldsymbol{f}) = \left|\mathcal{F}\{\psi(\boldsymbol{x})\}\right|^2, \tag{5.1}$$

where $\mathcal{F}\{\}$ is the 2D Fourier transform operator. Using the form of $\psi(\boldsymbol{x})$ given above, the Fourier transform is computed with the convention $\tilde{G}(\boldsymbol{f}) \equiv \mathcal{F}\{G(\boldsymbol{x})\}$:

$$\begin{aligned}\mathcal{F}\{\psi(\boldsymbol{x})\} &= \mathcal{F}\{O(\boldsymbol{x}) P_1(\boldsymbol{x}) + O(\boldsymbol{x}) P_2(\boldsymbol{x} - \Delta\boldsymbol{x})\} \\ &= \tilde{O}(\boldsymbol{f}) \otimes \tilde{P}_1(\boldsymbol{f}) + \tilde{O}(\boldsymbol{f}) \otimes \left(\tilde{P}_2(\boldsymbol{f}) e^{2\pi i(\Delta\boldsymbol{x}\cdot\boldsymbol{f})}\right),\end{aligned} \tag{5.2}$$

where $\otimes$ is the 2D convolution operator. Combining Eqn. 5.1 and Eqn. 5.2 gives the expression for the detector intensity as

$$\begin{aligned}I(\boldsymbol{f}) = &\left|\tilde{O}(\boldsymbol{f}) \otimes \tilde{P}_1(\boldsymbol{f})\right|^2 + \left|\tilde{O}(\boldsymbol{f}) \otimes \left(\tilde{P}_2(\boldsymbol{f}) e^{2\pi i(\Delta\boldsymbol{x}\cdot\boldsymbol{f})}\right)\right|^2 \\ &+ 2\mathbb{R}\left[\tilde{O}(\boldsymbol{f}) \otimes \tilde{P}_1(\boldsymbol{f}) \times \tilde{O}(\boldsymbol{f}) \otimes \left(\tilde{P}_2(\boldsymbol{f}) e^{2\pi i(\Delta\boldsymbol{x}\cdot\boldsymbol{f})}\right)\right],\end{aligned} \tag{5.3}$$

where $\otimes$ is a 2D convolution and $\mathbb{R}[\,]$ indicates the real part of a complex quantity. Comparing Eqn. 5.3 and Eqn. 4.1, we notice that the only difference between the expressions is the third term in Eqn. 5.3. Thus, if this term is removed, the resulting intensity distribution is identically that of one produced by two mutually incoherent propagating beams.

Now, in a procedure similar to [184], a Fourier transform of the intensity given in Eqn. 5.3 is computed to isolate the final term in the expression. This gives the autocorrelation of the exit surface wave

$$\begin{aligned}\mathcal{A}(\boldsymbol{\eta}) =& \mathcal{F}\Big\{ \left|\tilde{O}(\boldsymbol{f}) \otimes \tilde{P}_1(\boldsymbol{f})\right|^2 + \left|\tilde{O}(\boldsymbol{f}) \otimes \left(\tilde{P}_2(\boldsymbol{f})\, e^{2\pi i(\Delta\boldsymbol{x}\cdot\boldsymbol{f})}\right)\right|^2 \\ &+ 2\mathbb{R}\left[\tilde{O}(\boldsymbol{f}) \otimes \tilde{P}_1(\boldsymbol{f}) \times \tilde{O}(\boldsymbol{f}) \otimes \left(\tilde{P}_2(\boldsymbol{f})\, e^{2\pi i(\Delta\boldsymbol{x}\cdot\boldsymbol{f})}\right)\right] \Big\},\end{aligned} \tag{5.4}$$

where $\mathcal{A}$ is the autocorrelation with variable η. Using the Fourier shift theorem and the convolution theorem, Eqn. 5.4 is written as

$$\begin{aligned}\mathcal{A}(\boldsymbol{\eta}) =& \left(\overline{O}(\boldsymbol{\eta})\,\overline{P}_1(\boldsymbol{\eta})\right) \otimes \left(\overline{O}^*(\boldsymbol{\eta})\,\overline{P}_1^*(\boldsymbol{\eta})\right) \\ &+ \left(\overline{O}(\boldsymbol{\eta})\,\overline{P}_2(\boldsymbol{\eta}-\Delta\boldsymbol{x})\right) \otimes \left(\overline{O}^*(\boldsymbol{\eta})\,\overline{P}_2^*(\boldsymbol{\eta}+\Delta\boldsymbol{x})\right) \\ &+ \left(\overline{O}(\boldsymbol{\eta})\,\overline{P}_1(\boldsymbol{\eta})\right) \otimes \left(\overline{O}^*(\boldsymbol{\eta})\,\overline{P}_2^*(\boldsymbol{\eta}+\Delta\boldsymbol{x})\right) \\ &+ \left(\overline{O}(\boldsymbol{\eta})\,\overline{P}_2(\boldsymbol{\eta}-\Delta\boldsymbol{x})\right) \otimes \left(\overline{O}^*(\boldsymbol{\eta})\,\overline{P}_1^*(\boldsymbol{\eta})\right)\end{aligned} \tag{5.5}$$

where $\overline{G}(\boldsymbol{\eta}) = \mathcal{F}\left\{\tilde{G}(\boldsymbol{f})\right\}$. The first two terms in Eqn. 5.5 contain information pertaining to the autocorrelation of each term of the exit surface wave $\psi(\boldsymbol{x})$ and are referred to as the "DC" terms as they are centered at $\boldsymbol{\eta} = 0$. The last two terms are cross-terms and can be though of as the cross-correlation of the different contributions of $\psi(\boldsymbol{x})$ from the two probes. These terms are centered at $\boldsymbol{\eta} = \pm\Delta\boldsymbol{x}$ and are referred to as the "AC" terms. Because the probe functions $P_1(\boldsymbol{x})$ and $P_2(\boldsymbol{x})$ have finite support, each term in Eqn. 5.5 is also of finite extent, with a width equal to the sum of the widths of the contributing probe functions for each term. This results in distinct autocorrelation and cross-correlation peaks when data is viewed in this space.

Taking only the DC terms from Eqn. 5.5 and performing an inverse Fourier transform gives the filtered intensity:

$$\begin{aligned}I_{\mathcal{A}}(\boldsymbol{f}) =& \mathcal{F}^{-1}\Big\{ \left(\overline{O}(\boldsymbol{\eta})\,\overline{P}_1(\boldsymbol{\eta})\right) \otimes \left(\overline{O}^*(\boldsymbol{\eta})\,\overline{P}_1^*(\boldsymbol{\eta})\right) \\ &+ \left(\overline{O}(\boldsymbol{\eta})\,\overline{P}_2(\boldsymbol{\eta}-\Delta\boldsymbol{x})\right) \otimes \left(\overline{O}^*(\boldsymbol{\eta})\,\overline{P}_2^*(\boldsymbol{\eta}+\Delta\boldsymbol{x})\right) \Big\},\end{aligned} \tag{5.6}$$

where $I_{\mathcal{A}}(\boldsymbol{f})$ is the autocorrelation filtered intensity. This expression further simplifies to

$$I_{\mathcal{A}}(\boldsymbol{f}) = \left|\tilde{O}(\boldsymbol{f}) \otimes \tilde{P}_1(\boldsymbol{f})\right|^2 + \left|\tilde{O}(\boldsymbol{f}) \otimes \left(\tilde{P}_2(\boldsymbol{f})\, e^{2\pi i(\Delta\boldsymbol{x}\cdot\boldsymbol{f})}\right)\right|^2, \tag{5.7}$$

which is now equivalent to an intensity measurement produced by two mutually incoherent, non-interfering beams. The mathematical procedure described by Eqn. 5.1 - 5.7 is depicted in Fig. 5.2.

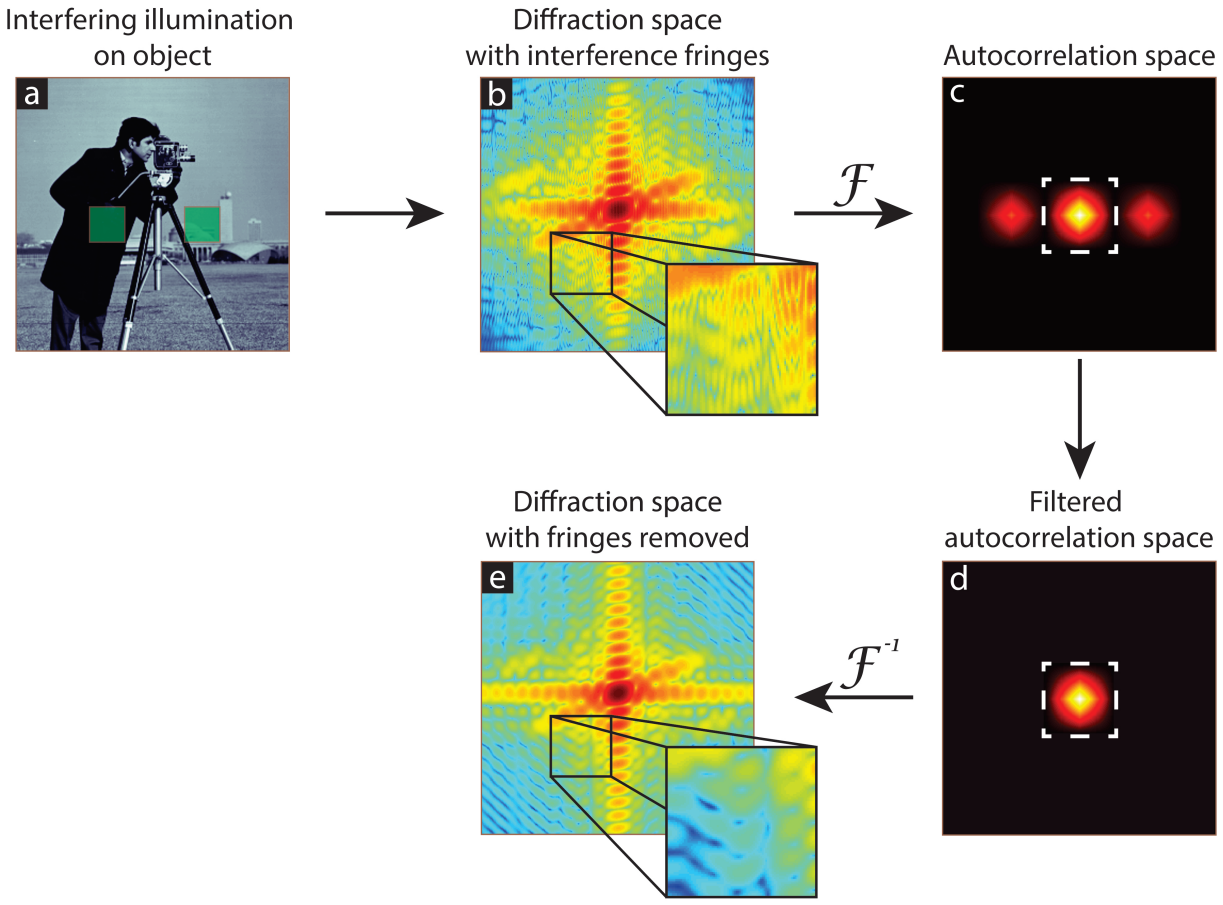

Figure 5.2: **The Process of Autocorrelation Filtering**. (a) Two coherent probes (green squares) are incident on an object. (b) The resulting field propagates to a detector located in the far field, recording a diffraction pattern that contains high frequency interference from the interaction of the exit surface wave of each probe. (c) Fourier transforming the signal intensity brings it into autocorrelation space, where the (d) incoherent sum of the exit surface waves (DC peak) can be filtered from the interference terms (AC peaks), provided the system satisfies Eqn 5.9. (e) Inverse transforming the filtered signal yields an incoherent sum of the diffraction from each probe which can then be used for image reconstruction. Reproduced from [181].

Diffraction intensity measurements treated with this filtering method can now be used directly with any of the existing multiple mode ptychography reconstruction algorithms to retrieve images

pertaining to the regions of the sample scanned by each probe. This filtering procedure is referred to as "autocorrelation filtering".

As long as the AC and DC peaks do not overlap in autocorrelation space, filtering is possible. This is a condition on both the size of peaks and the separation between them. First, consider that that the AC peaks must be sufficiently offset from the DC peaks such that there is no overlap between them. This means the magnitude of the separation between the probes, $|\Delta \boldsymbol{x}|$, must be larger than the full width of the DC peak. The autocorrelation of a function with finite support is twice the width of the function itself. Defining the characteristic probe width in the object plane, D, we have the condition

$$|\Delta \boldsymbol{x}| \geq 2D. \tag{5.8}$$

where $\Delta \boldsymbol{x}$ is the probe separation. This constraint alone is not sufficient as it does not consider the size of the AC peaks themselves. Namely, in order for the AC and DC peaks to be separated, the extent of the probes must be sufficiently small. The spatial extent of autocorrelation space is determined by experimental parameters and geometry and is defined as $\mathbb{X} = \frac{\lambda z}{p}$ where λ is the wavelength of the illumination, z is the propagation distance between the detector and the sample plane, and p is the detector pixel pitch. The ratio of this extent to the beam diameter is an alternate way to express the oversampling ratio previously described in Eqn. **??**, $\sigma = \mathbb{X}/D$. The AC and DC peaks must all fit within the autocorrelation space without overlap, all of which have width $2D$. The optimal way to ensure there is no overlap while maximizing the size of the illumination is to require that $\sigma = 4$. This is in contrast to most CDI techniques which require the looser constraint that $\sigma = 2$ to properly sample the diffraction amplitude [183, 185].

Furthermore, as the separation of the beams is increased, the interference is pushed to a higher spatial frequency. Referring to Eqn. 5.5, this has the effect of moving the AC peaks in autocorrelation space. Eventually this frequency will exceed the sampling rate of the detector (i.e. the detector pixel size) and the interference signal will alias. This can cause the AC and DC peaks to overlap once again, preventing the isolation of the DC terms. However, if the separation is

further increased, the interference will alias back to an acceptable frequency and autocorrelation filtering is again permitted. The effects of aliasing gives rise to repeated regions values of $|\Delta \boldsymbol{x}|$ where autocorrelation filtering is permitted. These regions are shown in Fig. 5.3.

The full condition on the beam separation must include the effect of aliasing on the recorded diffraction intensity. Taking this into account, the condition is best expressed with the dimensionless inequality

$$2 \leq \mathrm{mod}\left(\frac{\Delta x}{D}, \sigma\right) \leq \sigma - 2 \tag{5.9}$$

where mod ( ) is the modulus operator.

5.2.2 Alias Cloaking

Referring to Fig. 5.3, it is observed that there is a decrease in the intensity of the interference fringes as the probe separation is increased. This effect is explored through a study of a normalized error which compares the diffraction intensity pattern produced by a two beam system that is allowed to interfere with an equivalent system that does not include interference. This error is defined as

$$\mathcal{E}_{rms} = \sqrt{\frac{1}{M}\sum_{m}\left[S_I\left(\Delta L\right) - S_N\left(\Delta L\right)\right]^2}, \tag{5.10}$$

where $\mathcal{E}_{rms}$ is the root-mean-squared error, M is the total number of elements within a signal, S_I is the signal with interference fringes, S_N is the equivalent signal without interference, and ΔL is a normalized probe separation such that $\Delta L = \Delta x / D$.

As the probe separation increases, the overall trend of $\mathcal{E}_{rms}$ is to decrease. This is due to the aliasing of inter-beam interference which suppresses the fringe intensity. Once the beam separation increases past a critical point, the period of the interference is less than the extent of a detector pixel. In this scenario, the interference is measured as a single value corresponding to the average of the fringe within the pixel. As ΔL tends towards infinity, this average value becomes more uniform across the detector, eventually becoming a constant background added to the signal measured by each pixel. As the interference is averaged away, the diffraction pattern approaches

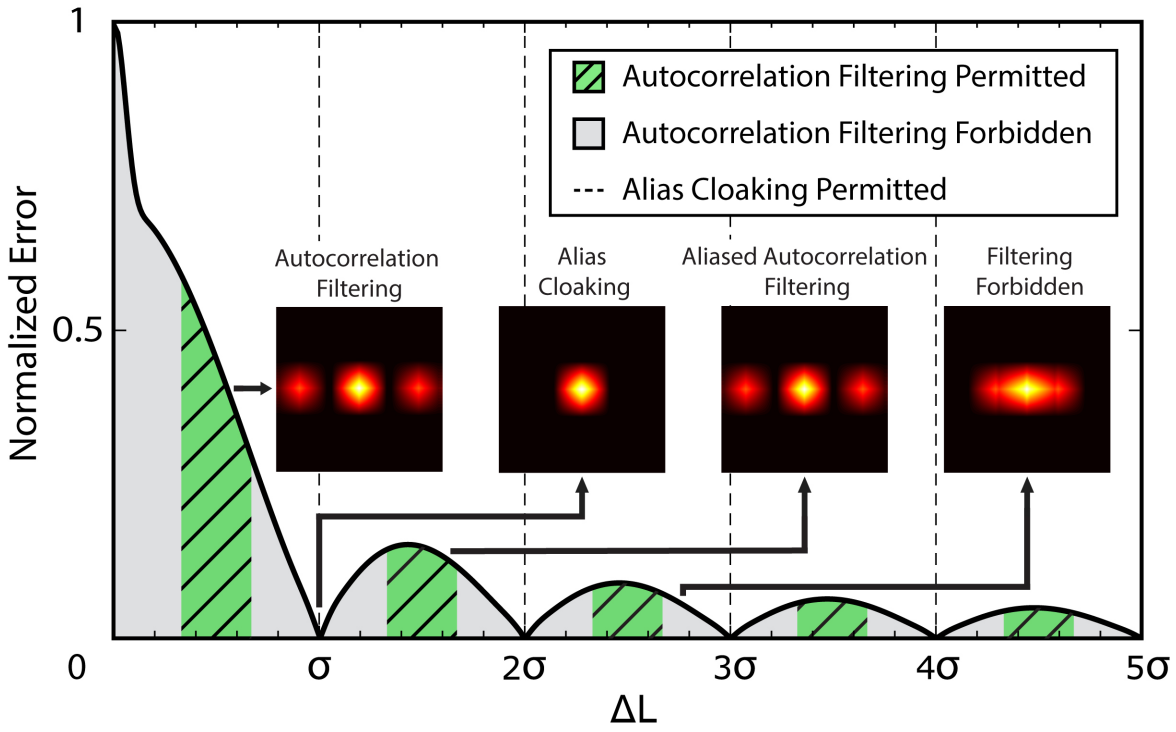

Figure 5.3: **The Effect of Aliasing on Autocorrelation Filtering**. The difference between an intensity pattern produced by mutually incoherent (non-interfering) and mutually coherent probes is plotted as a function of normalized probe separation $\Delta L = \Delta x/D$. The striped, green regions correspond to probe separations where autocorrelation filtering is permitted. Grey regions indication those where filtering is forbidden, noting regions where the AC and DC peaks overlap in autocorrelation space. Note that there are many repeating regions where filtering is permitted, this is due to the effect of aliasing on the interference frequency as the probe separation increases. There are regions where the difference falls to zero. These occur at values of the probe separation with the spatial frequency of the interference precisely matches the sampling rate of the detector. In these cases, the interference is measured as a uniform background and is removed from the measured due to the experimental configuration. These points are where alias cloaking is permitted. The small inserts depict the layout of autocorrelation space for various vlaues of ΔL . Reproduced from [181].

the non-interfering case, resulting in the overall trend in the normalized error.

As ΔL is increased, there are points in Fig. 5.3 where the error naturally drops to zero. These points occur when the detector pixel size is equal to an integer number of interference fringe periods. When this occurs, there is no difference in the measured average fringe value between pixels across the detector and the inference appears as a uniform background. Here, the aliasing has naturally removed or "cloaked" the interference and the diffraction appears identical to that

produced by an incoherent beam system. This process is called alias cloaking. Data collected in this configuration is immediately ready for reconstruction with a multi-mode ptychography algorithm without additional filtering.

The critical beam separations where alias cloaking occurs are completely determined by the experimental geometry. Referring to Eqn. 5.3 and recalling the geometric relation between frequency and detector coordinates, $\boldsymbol{f} = \boldsymbol{x}/\lambda z$ [36], the interference on the detector occurs with some mean frequency $f_I = \Delta x/\lambda z$. The diffracted wave is sampled on the detector with a frequency $f_s = 1/p$. The alias cloaking condition is satisfied when f_I is an integer multiple of f_s. Setting these quantities equal and solving for the beam separation gives the critical probe separation

$$\Delta x_c = \frac{N\lambda z}{p}, \tag{5.11}$$

where N is an integer.

Due to the finite size of the detector pixels, the visibility of the interference at frequencies in the vicinity of f_I are also suppressed. As ΔL becomes larger, the slope of the error surrounding the minima decreases, meaning the system becomes more resilient to misalignment as the beam separation is increased. Fig. 5.3 can be further extended to show that at large values of ΔL, the error introduced by the interference is naturally suppressed at all values of Δx and restrictions on the system parameters to obtain alias cloaking are greatly relaxed.

5.3 Experimental Results

The schematic of the visible-wavelength transmission-mode ptychographic microscope is shown in Fig. 5.1. Although the two methods described above require a slightly different apparatus, they share common elements to produce and shape the beam, as described here. A fiber-coupled laser diode [Blue Sky Research FTEC2 658-60, = 656 nm] propagates through a spatial filter [Newport, 900: with a 5 m pinhole 900PH-5 and M-10X objective] to clean up the laser mode. The filtered beam is then collimated by a lens with focal length f = 5 cm. At this point the setup must be optimized for the different techniques and samples, as described for each experiment below.

5.3.1 Autocorrelation Filtering

This section demonstrates the feasibility of configuring a ptychographic CDI microscope to use the autocorrelation filtering method described in section 5.2.1. Using the setup described in Fig. 5.1, the beam is transmitted through a pinhole mask consisting of three pinholes in an L-shape formation, fabricated with anodized aluminum foil [Thorlabs, BKF12] in which three pinholes were punched with a pushpin [Staples, 32014]. The pinholes ranged in diameter from 90 - 175 μm, with center-to-center separations of approximately 0.75 mm. The pinhole array is imaged onto a sample using an imaging lens with focal length f = 10 cm; the imaging system has magnification M = 1. The light is scattered though a Negative United States Air Force (NUSAF) resolution test chart [ThorLabs, R3L3S1N] and is captured by a Fourier transform lens with focal length f = 2 cm, which focuses the scattered light onto a CMOS detector [Mightex, SCN-B013-U]. A schematic of the experiment is shown in Fig. 5.4(a). Given these system parameters, the oversampling of each individual beam ranged from 10–15, with the parameter ΔL falling between 7.8 - 11.8, satisfying Eqn. 5.9 without any aliasing in the signal.

Data were recorded at 121 scan positions in an 11x11 rectilinear grid with random offsets of 20% to avoid periodic artifacts [158]. At each position, multiple exposures were captured with exposure times ranging from 0.05 ms to 750 ms. The resulting images were combined, increasing the dynamic range of the detector from 68 dB to 100 dB [186]. Complex valued images for the object and probe associated with each of the three beams were reconstructed with a modified version of the multimode ptychography algorithm described in [168]. The reconstructed objects and probes are shown in Fig. 5.4. The probes and objects are displayed in complex amplitude with amplitude mapped as brightness and phase as hue. The three reconstructed regions correspond to three different areas of the USAF test pattern.

To further study the capabilities of autocorrelation filtering, the microscope was adjusted such that the frequency of interference between the beams was aliased on the detector. This aliasing property allowed for a larger beam separation. This experiment is schematically depicted

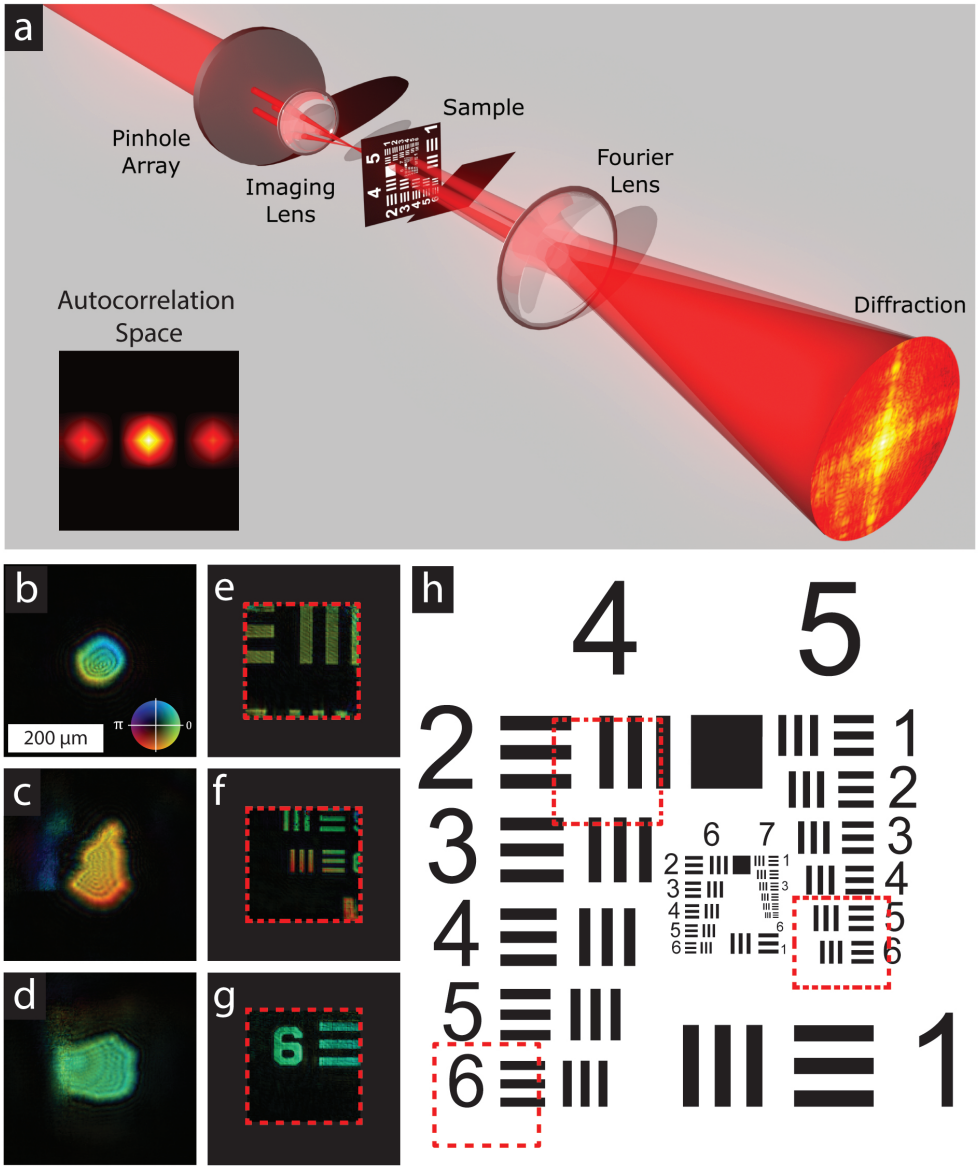

Figure 5.4: **Experimental Results for Autocorrelation Filtering**. (a) The experimental setup used to test the autocorrelation filtering technique, the small inset displays an example of autocorrelation space for the pinhole array used during this experiment. (b-c) The complex amplitude of the reconstructed probes recovered from the multimode ptychographic reconstruction after autocorrelation filtering, where brightness is amplitude and hue represents phase. (e-f) The complex amplitude of the reconstructed image of the NUSAF test chart sample. (h) A diagram of groups 4-7 of a USAF resolution test chart. The dashed lines show the relative positions of each reconstructed area in (e-f). The recovered probes and objects are paired by row. The scale bar of 200 μm and color wheel shown in (b) are common for (c-g). Reproduced from [181].

in Fig. 5.5(a). A new pinhole mask was fabricated, consisting of two circular pinholes, each with

a diameter equal to 0.4 mm, separated by a center-to-center distance of 3.7 mm. Due to the large probe separations in this experiment, the transform lens was replaced with an aspherical lens [Thorlabs AL2520-B] of equivalent parameters to reduce the spherical aberrations on the recorded diffraction data.

The imaging system was removed from the previous experiment in favor of placing the pinhole mask in close proximity to the sample to simplify the experimental setup. The sample consists of a transverse slice of nymphaea of aqustio stem mounted on a microscope slide and preserved in cedar wood oil [Amscope PS25]. With these parameters, the system had an individual beam oversampling of $\sigma = 6.3$ and normalized probe separation $\Delta L = 9.3$. These parameters place this experimental geometry in the second allowed filtering region in Fig. 5.3, meaning the interference has aliased to to a lower frequency.

A 64-position ptychography scan was recorded arranged in an 8x8 rectilinear grid, with 20% random offsets between adjacent scan positions. Data were processed identically to the previous experiment, where autocorrelation filtering was applied to remove the interference terms and reconstructed using a multimode ptychography algorithm [168]. The reconstructed amplitudes of each object and probe are shown in Fig. 5.5(b-c).

5.3.2 Alias Cloaking

Alias cloaking is demonstrated experimentally to validate the method outlined in section 5.2.2. The setup for this experiment uses the laser system depicted in Fig. 5.1, with the pinhole array and imaging system shown in Fig 5.6(c). The pinhole array consists of three circular apertures arranged in a linear pattern, each with a diameter of 1.26 mm and a center-to-center separation of 2.50 mm. These system parameters give an individual beam oversampling of $\sigma \approx 2$ and satisfies the critical beam separation given in Eqn. 5.11 with $N = 1$. Referring the Fig. 5.3, note that the system is sitting in the first null with $\Delta L = \sigma$. Due to the large peripheral error for surrounding values of ΔL, this configuration is the least ideal experimental setup to perform alias cloaking as it is most sensitive to misalignment.

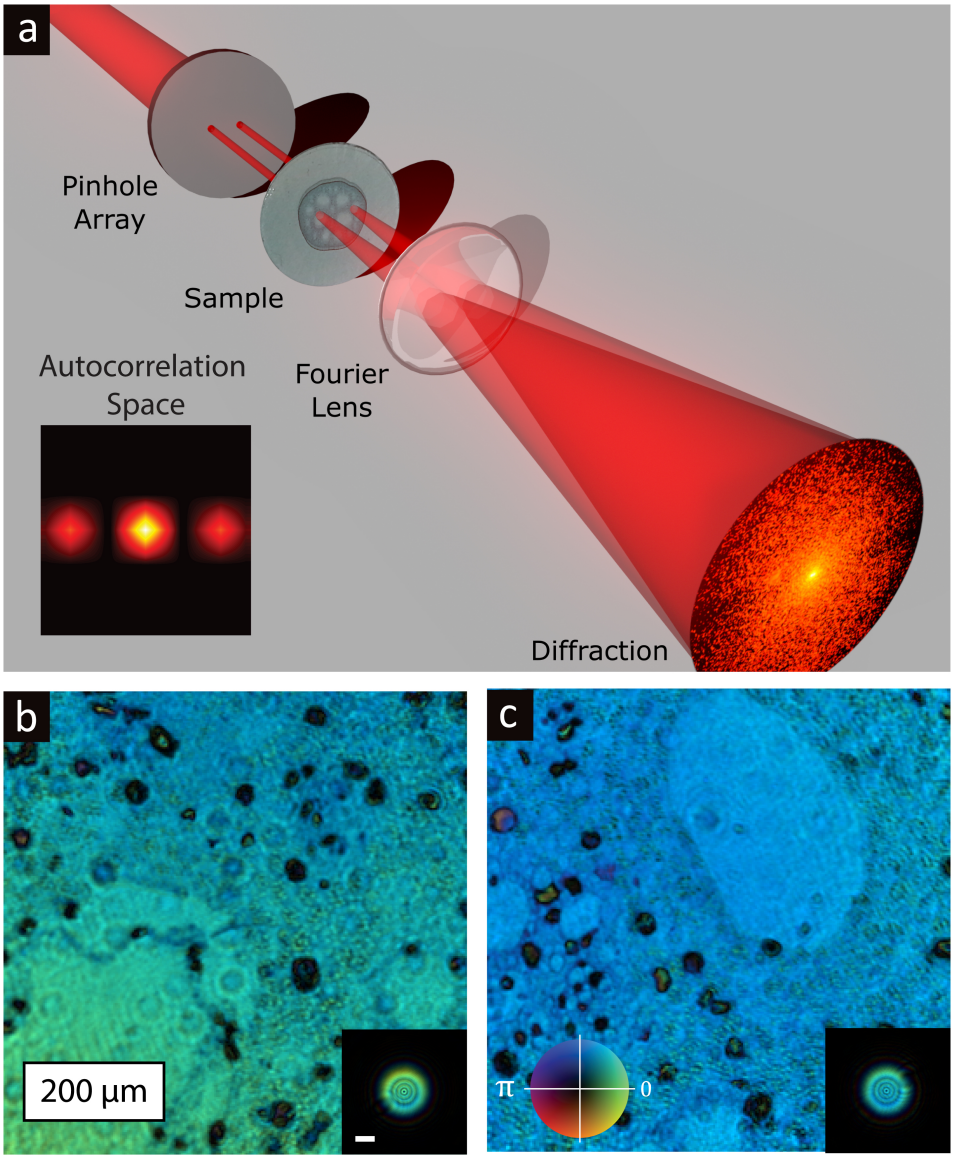

Figure 5.5: **Experimental Results for Aliased Autocorrelation Filtering**. (a) The experimental schematic for aliased autocorrelation filtering, the small inset displays an example of autocorrelation space for the pinhole array used during this experiment. (b-c) The reconstructed complex amplitudes of the nymphaea of aqustio sample and the illuminating probes. The scale bars represent 200 μm in the object field-of-view and probe inset field-of-view respectively. The scale bars and color scheme are equivalent for both b and c. In these images brightness indicates the amplitude and hue corresponds to phase. Reproduced from [181].

A ptychography scan was recorded using a test sample consisting of a thin transverse slice of a rabbit testicle mounted on a microscope slide and preserved in cedar wood oil [AmScope, PS25].

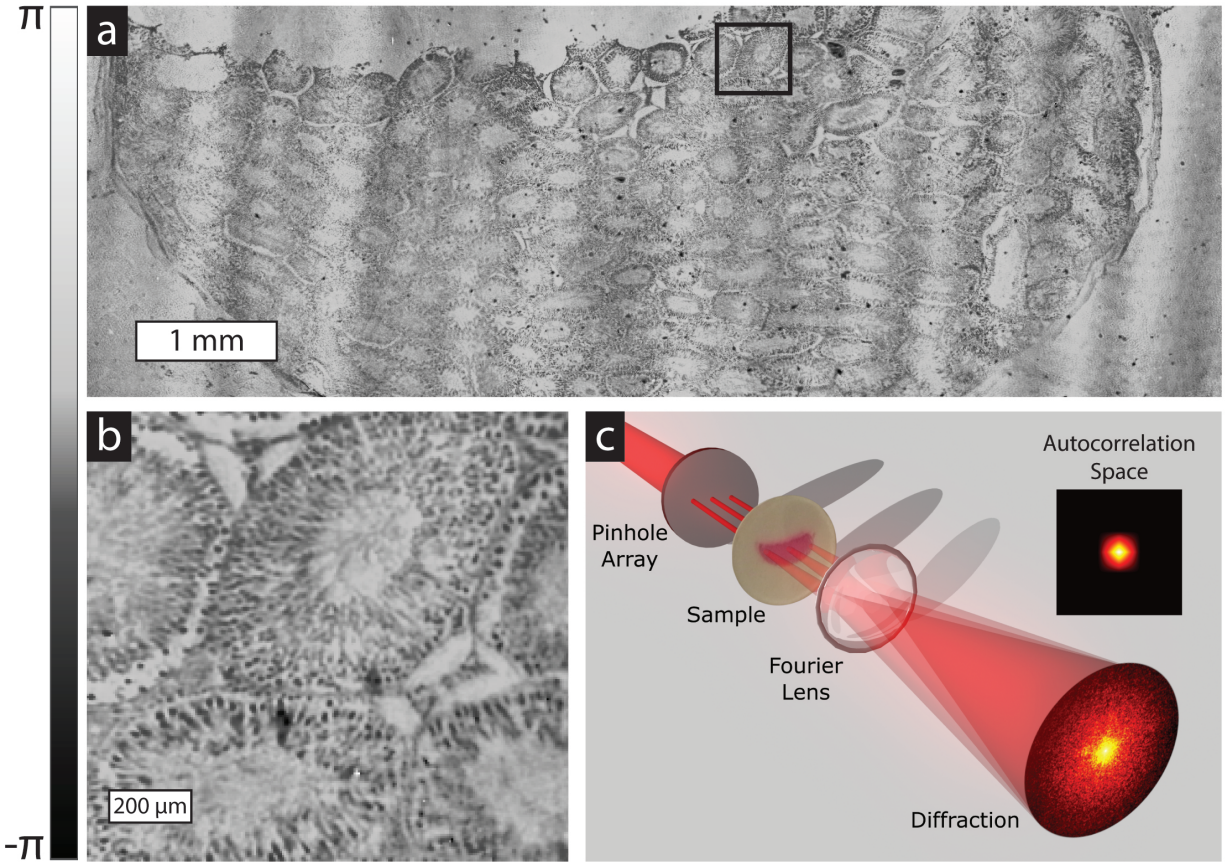

Figure 5.6: **Experimental Results for Aliased Autocorrelation Filtering**. (a) Large FOV phase reconstruction of a cross-sectional slice of a rabbit testicle obtained using alias cloaking ptychography. (a) is composed of reconstructed objects from three identical beams simultaneously incident on the sample, each imaging one third of the specimen. (b) An enhanced region shown by the black square outline in (a). (c) Experimental apparatus used to obtain the reconstructions shown in (a, b), where the small inset displays an example of autocorrelation space for the pinhole array used during this experiment. Notice the cross-correlation peaks are naturally suppressed. Scale bars are 1 mm (a) and 200 um (b). Reproduced from [181].

The scan consisted of 784 scan positions arranged in a 28 x 28 square grid with a step size of 1/6 the beam radius, modulated with a 20% random offset. The large number of scan positions, coupled with the scan position step size and beam diameter, lead to overlapping fields of view in the reconstructed objects. Because the diffraction-limited resolution of each reconstruction is independent of the collective probe system, each object retains a high spatial resolution.

The three reconstructed images were manually registered. Once registered, the images were

averaged together using a cosine smoothing image stitching algorithm. This algorithm weights image pixels more heavily the further they are from their respective image edge. This stitching algorithm is used to combat the fall off in reconstruction quality near the edge of a scan area. This is due to the decreased level of overlap near the periphery of a ptychography scan region. The single large field-of-view, high-resolution image is shown in Fig. 5.6(a). The total reconstructed area is 21.5 mm^2. Fig. 5.6(b) shows an enlarged region given by the black square outline in Figure 5.6(a).

In the original reconstruction, a quadratic phase was present in all three reconstructed objects. The presence of this phase indicates a slight bow in the sample. This curvature was verified by placing the sample in an interferometer [Zygo GPI XP]. Phase data measured in the interferometer is show in Fig. 5.7 along with a cubic fit. The fit demonstrates a second-order phase across the sample. For viewing purposes, this phase was removed from Fig. 5.6(a, b).

5.3.3 Image Quality Analysis

Previous work on multimode ptychography algorithms show that multiplexing data has no detectable effect on reconstructed image resolution of the complex object transmission function [168]. To investigate the effect of alias cloaking on the system resolution, reconstructions of equivalent fields of view of the sample obtained using alias cloaking and single beam ptychography are analyzed. The two reconstructions are show in Fig. 5.8 (c, d). A short glance shows that the reconstructions look nearly identical, except for a low frequency oscillation present in the multi-beam reconstruction. This modulation is due to a persistent back reflection, present in all the diffraction patterns taken during the scan. Thus modulation is not an artifact due to multiple beam techniques.

To compare the two reconstructions, the phase retrieval transfer function is calculated [69, 187, 188]. The function is defined as

$$\mathrm{PRTF}\left(f_r\right) = \left\langle \frac{\left\langle \sum_n \left| \left\langle \psi_n^{rec}\left(\boldsymbol{x}_j\right)\right\rangle_i \right| \right\rangle_j}{\left\langle \sqrt{I^{meas}\left(\boldsymbol{x}_j\right)} \right\rangle_j} \right\rangle_{\varphi}, \tag{5.12}$$

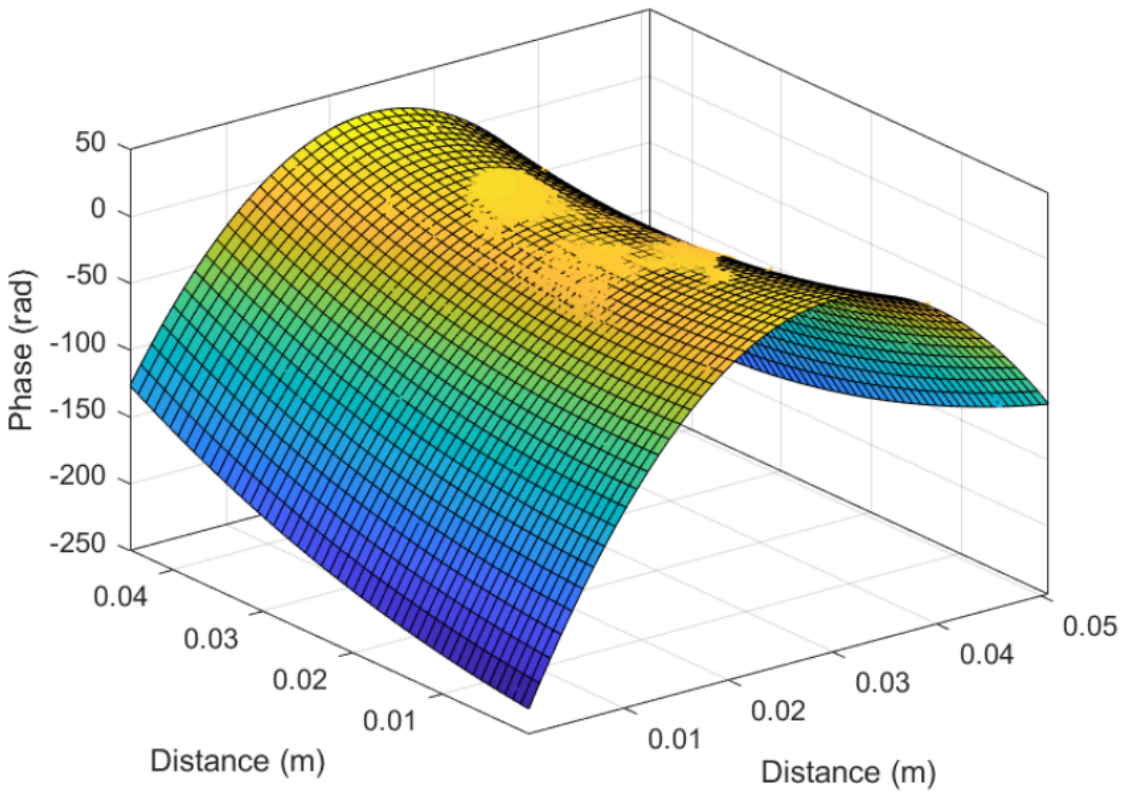

Figure 5.7: **Laser Interferometry of Rabbit Cell Sample**. Phase data measured with a laser interferometer on the rabbit cell sample used for alias cloaking experiments. Data are displayed with a cubic fit. The fit displays a quadric phase present in the sample. This phase indicates a curvature in the sample.

where $\psi_n^{rec}(\boldsymbol{x}_j)$ is the j^{th} reconstructed diffraction pattern generated by the n^{th} probe, $I^{meas}(\boldsymbol{x}_j)$ is the intensity measurement corresponding to the j^{th} scan position, $\langle\rangle_m$ corresponds to an average over parameter m, with i indicating an average over independent reconstructions, n is the individual reconstructed probe, j is the scan positions, and φ is the azimuthal angle of the diffraction pattern. This calculation used 100 independent ptychography reconstructions produced with 500 iterations each. The phase retrieval transfer function for the single and multiple beam reconstructions are shown in Fig. 5.9.

An estimate for the resolution is found by locating the spatial frequency corresponding to the point where the phase retrieval transfer function falls below 0.5 [188]. The location of this point

provides an estimated spatial resolution of 2.85 μm for the multiple beam case and 2.70 μm for the single beam case. The Abbe diffraction-limited resolution of the microscope is calculated at 2.48 μm.

The two imaging modalities are further compared by examining their azimuthally averaged power spectral densities. The power spectral density used here is a measure of the azimuthally averaged power as a function of spatial frequency, defined as

$$\mathrm{PSD}\left(f_r\right) = \left\langle \left|\mathcal{F}\left\{\mathrm{I}\left(\boldsymbol{x}\right)\right\}\right|^2 \right\rangle_{\varphi}, \tag{5.13}$$

where $\mathrm{PSD}\left(f_r\right)$ is the azimuthally averaged power spectral density and $\mathrm{I}\left(\boldsymbol{x}\right)$ is the image of interest. The power spectral densities and the multiple and single beam reconstruction used in this analysis are shown in Fig. 5.8 (a, c, d). The two spectra are nearly identical, with the average ratio between them being 0.98.

It is expected that the maximum number of allowable beams for use in multiple beam ptychography is limited by the finite dynamic range of the detector, as is the case for multiplex holography [189]. The exact relation between reconstruction quality, number of beams, and detector dynamic range is currently unknown, but provides an interesting subject for further analysis of multiple beam ptychographic imaging systems.

5.4 Discussion and Conclusion

The throughput of a ptychographic imaging system is a key factor that limits the applicability of this powerful imaging technique. The diffraction-limited, high-throughput imaging with inherent phase contrast obtained with CDI is of great interest in the field of bio-imaging and material characterization, where large scale properties are inherently linked to the behavior and characterization of local order, interactions, and phenomena. In this work, a proof-of-principle demonstration of two novel techniques allowing for the use of multiple coherent illuminating probes to simultaneously image multiple areas of a sample was provided. These techniques provide a method for removing the interference between the coherent probes, allowing the data to be processed using a multiple

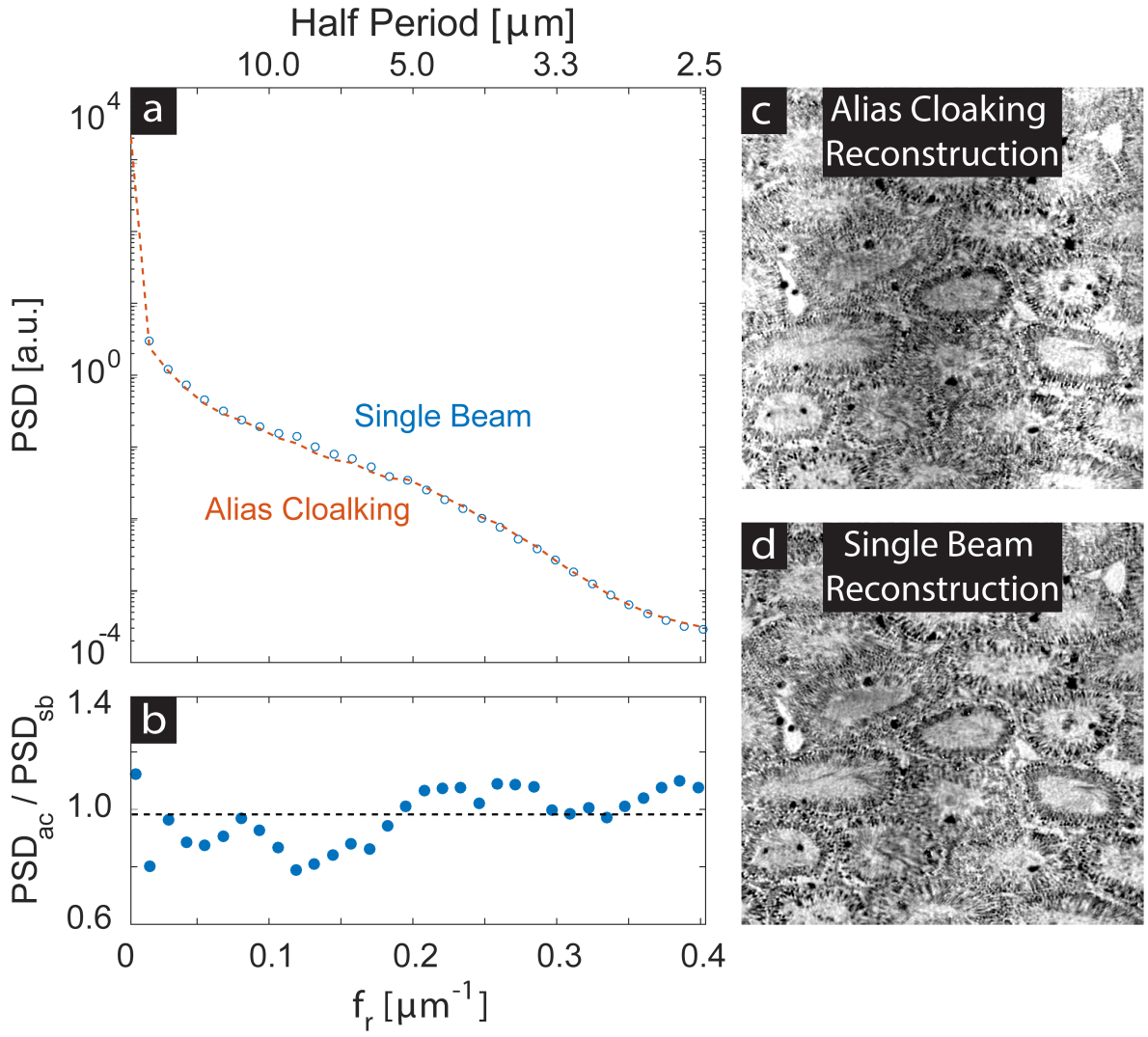

Figure 5.8: **Comparison of Power Spectral Density in Between Multiple Beam and Single Beam Ptychography**. (a) The azimuthally averaged power spectral density of two phase map reconstructions. One obtained while using an alias cloaking experimental geometry (c) and one obtained using conventional single beam ptychography (d). The field-of-view and scales are equivalent in (c-d). (b) displays the ratio of the power spectral density shown in (a) a function of spatial frequency. The mean value of this ratio is 0.98. The similarity of the PSD for the two different imaging modalities indicates that the two imaging techniques produce similar results. Reproduced from [181].

mode ptychography algorithm.

Multiple beam ptychography provides large field-of-view, high-throughput imaging while minimizing the required data acquisition. This imaging technique is implemented by controlling the

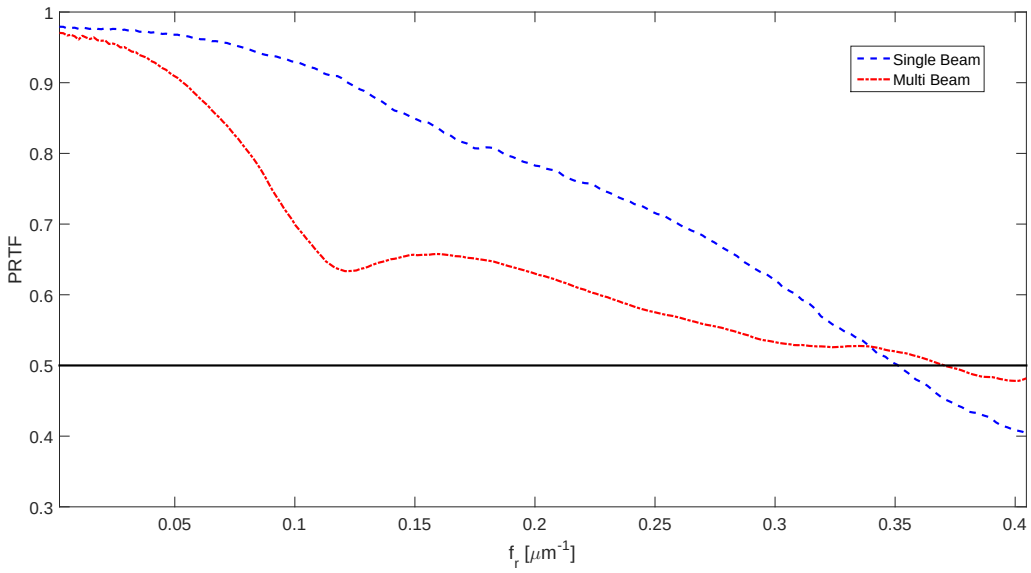

Figure 5.9: **Comparison of Single and Multiple Beam Ptychography Resolution**. The phase retrieval transfer function of the single and multiple beam ptychography reconstructions of equivalent fields of view, shown as a function of spatial frequency. A value of 0.5 is used as a cutoff value to determine the resolution of a reconstruction. In this analysis, the multiple beam reconstruction has a slightly higher cutoff frequency, indicating a higher resolution than the single beam image.

relative placement of the illuminating probes and can be applied in either data post-processing through autocorrelation filtering, or experimentally through alias cloaking. High fidelity reconstructions are obtained when samples were simultaneously illuminated by either two or three coherent probe beams. This technique could be applied in the X-ray and EUV spectral ranges, where large field-of-view images with nanometer spatial resolution provide key insight into the relationship between microscopic order and macroscopic material properties.

Chapter 6

Spectroscopic X-ray Imaging of the Allende Meteorite

6.1 Introduction

The last decade of intense focus and research has seen ptychography mature in a well established technique for nanoscale microscopy [190–193]. Applications of X-ray ptychography include two and three dimensional investigations of biological systems [194, 195] and integrated circuit structure [196, 197], where a lateral resolution of tens of nanometers is regularly obtainable. Recent developments have extended soft X-ray imaging toward a diffraction limited lateral resolution of 5 nm [198, 199].

Scanning transmission X-ray microscopy (STXM) is a valuable tool when spatially resolved, spectrally sensitive information is required. This technique involves tightly focusing an X-ray beam and raster scanning a sample, where a bucket detector records the localized X-ray absorption of the illuminated areas. In this configuration, an image is built up pixel by pixel, with the resulting image resolution limited by the focal spot size of the X-ray beam. Combining STXM with soft X-ray absorption spectroscopy, affords a system that can map the chemical-specific composition of oxygen, nitrogen, carbon, and transition metals like iron, manganese, and nickel in for biological and material systems [200].

In this chapter, STXM and X-ray ptychography spectromicroscopy are used to investigate an Allende meteorite grain. Complex X-ray transmission images of a meteorite grain are obtained with spatial resolution of 15 nm, an improvement of more than an order of magnitude over previous studies [201]. The high resolution images and spectral information are used to infer mineral

composition of the grain and potential formation processes of the meteorite. Results and methods presented here are part of a correlative microscopy study of the Allende meteorite with electron and X-ray imaging, previously published in [202].

6.2 Methods

6.2.1 Allende Meteorite

The Allende meteorite is a CV3 carbonaceous chondrite that fell in Chihuahua, Mexico on February 8, 1969. Breaking down during its entry into Earth's atmosphere, fragments of the meteorite were spread over an area approximately 8 km by 50 km, one of the largest strewnfields known on Earth. Hundreds of meteorite fragments were collected ranging in size from approximately 1 g to 110 kg; overall 2 - 3 tons of meteoric stone was collected, making it one of the most abundant sources of meteoric samples for study [203]. Due to the timing of its arrival and abundance, Allende was well studied as many laboratory facilities had been established to receive samples from the Apollo program which was expected to return with the first samples of the lunar surface in just a few months. Consequently, the Allende meteorite is colloquially referred to as "the best-studied meteorite in history" [204].

The meteorite is a heterogeneous aggregation of calcium and aluminum rich inclusions and millimeter-sized chondrules, set in a fine-grained matrix of micro- to sub-micrometer sized oxides, suflides, silicates, and metals. The chondrules are small stony spherules which formed as molten droplets in space before being accreted into a larger body and are among the oldest matter observed on Earth, predating the Earth itself by 30 million years. These chondrules contain valuable information about conditions during the early formation of the solar system [205]. The chemical diversity and nanometer sized petrographical features make the meteorite an interesting sample for X-ray spectromicroscopy.

6.2.2 Sample Preparation

In this study, unsorted Allende meteorite fragments were added to an agate mortar and immersed in ethanol, then pounded by an agate pestle into sub-micrometer grains. The resulting suspension was sonicated for 2 minutes to further disperse the particles. The solution was then drop cast using a pipette onto a carbon film 200 mesh Cu transmission electron microscope (TEM) grid. Samples were then air dried for 24 hours before data acquisition.

6.2.3 X-ray Imaging Data Acquisition

Ptychography and STXM data were recorded at the COherent Scattering and MICroscopy (COSMIC) beamline – beamline 7.0.1 at the Advanced Light Source (ALS) at Lawrence Berkeley National Lab (LBNL). COSMIC has a tunable, coherent soft X-ray source, suppling monochromatic light with energy ranging from 250 eV to 2500 eV, spanning the carbon and sulfur K-edges. X-rays were focused using a Fresnel zone plate with outer zone width of 45 nm, giving a total coherent flux of 10^9 photons/s at the sample position. The beamline endstation, known as Nanosurveyor 2, incorporates the sample area hardware of an FEI CM200 series TEM to leverage the existing design of a TEM for a high stability sample manipulation [198]. The design uses a standard FEI CompuStage sample manipulator where the sample is secured with a Hummingbird 3 mm half-grid tip. This common sample mounting scheme allows for easy transfer of sample between X-ray and electron microscope for correlative study. The design preserves much of the function of a standard TEM, meaning any sample manipulator for the CM200 series CompuStage can be used in the Nanosurveyor 2. This allows for tomographic, cryo-biased, and other in-situ experiments to be performed in this setup.

Once the sample was mounted and inserted into the sample chamber, it was pumped down to 1 x 10^{-6} torr. Diffracted X-ray light was recorded with a novel fast charge-coupled device developed at LBNL. The device was configured withe a 50 frames/s frame rate, 15 bit dynamic range, a 12 bit analogue-to-digital converter, and a 512 x 512 pixel chip with 26 μm pixels. During the experiment,

the on-chip binning was set to 2. All diffraction data were collected without a beamstop. The X-ray imaging system is schematically shown in Fig. 6.1.

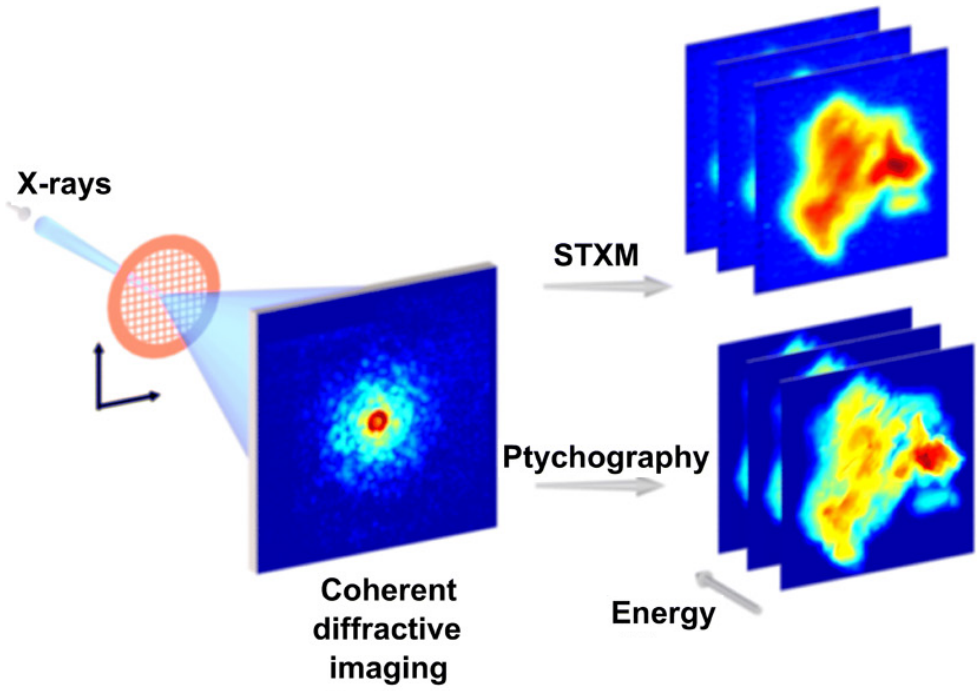

Figure 6.1: **X-ray Imaging Scheme at COSMIC**. Allende meteorite grains deposited on a TEM grid was mounted in the COSMIC soft X-ray beamline for ptychographic and spectromicroscopic studies. The beamline incorporates a FEI CM200 CompuStage for sample mounting and manipulation. This scheme allows for easy sample transfer for correlative electron microscopy studies. Ptychography and STXM datasets are collected in a transmission mode, where X-ray light ranging from 707 - 1551 eV was used to probe the sample. High energy resolution spectroscopic image stacks were captured using STXM at the Fe L_3 edge (707 eV), Ni $L_{2/3}$ edge (865/848 eV), Mg K edge (1302 eV), and Al K edge (1551 eV). Ptychography data were collected 5 eV before and on resonance of the absorption edges. Modified from [202]

STXM data were recorded by raster scanning a region of the sample in an 80 x 80 square scan grid with a 40 μm step size and a 10 ms dwell time per point. The resulting image had a 3.2 μm by 3.2 μm field of view. X-ray absorption spectra can be collected over a specified spectral range at a single location, along a line with a specified direction, or throughout the entire image field of view. Line scans were initially performed to calibrate the desired photo energies corresponding to an absorption edge for a specific element, then image stacks were recorded with the energies

varying across the absorption feature. STXM absorption spectroscopy were recorded at the Fe L_3 edge (707 eV), Ni $L_{2/3}$ edge (865/848 eV), Mg K edge (1302 eV), and Al K edge (1551 eV). The energy resolution varied within the scan, beginning with a 1 eV step size -15 eV before the edge, moving to 0.25 eV with $\pm$5 eV of the absorption resonance, then back to a 1 eV step size until the energy of the X-rays was 15 eV above the edge. STXM energy stack would take between 30 to 60 minutes to record depending on the absorption edge width.

Ptychography data were collected using a double exposure mode. Dwell times of 15 ms and 150 ms were used to enhance the dynamic range of the recorded diffraction patterns. Square scan grids of 80 x 80 or 100 x 100 positions with a step size of 30 nm cover a field of view of 3.2 - 5.8 μm^2. With these scan parameters and experimental geometry, the reconstructed pixel size was 8 nm/pixel. Each ptychography dataset consisted of 6,400 - 10,000 diffraction patterns of 256 x 256 pixels. Ptychography scans were collected both 5 eV before and on resonance a the Fe L_3 edge, Ni $L_{2/3}$ edge, Mg K edge, and Al K edge. These dataset provide a differential measurement, at each absorption feature, allowing the element to be easily isolated in the sample.

6.3 STXM Data Analysis

STXM absorption spectroscopy was used to provide local chemical information in the meteorite grain. A STXM image stack recorded at different X-ray energies was processed using the MANTiS software to calculate and isolate the composition of the meteorite [206]. The spectral range of a STXM energy stack was chosen to span different atomic resonances, then converted to optical density by normalizing to a fully transmitting regions in the acquired field of view. Hot pixel were replaced by the average of the six neighboring pixels and the background was subtracted. After this, the image stack was aligned iteratively using center of mass and common line alignment methods. Spectra in the 3D image stack were decomposed using principle component analysis (PCA) and k-means clustering to group clusters with similar spectra. Last, singular value decomposition was used to produce chemical maps and corresponding absorption spectra. The recorded spectrum and corresponding STXM images for the Fe L_3 edge are shown in Fig. 6.2.

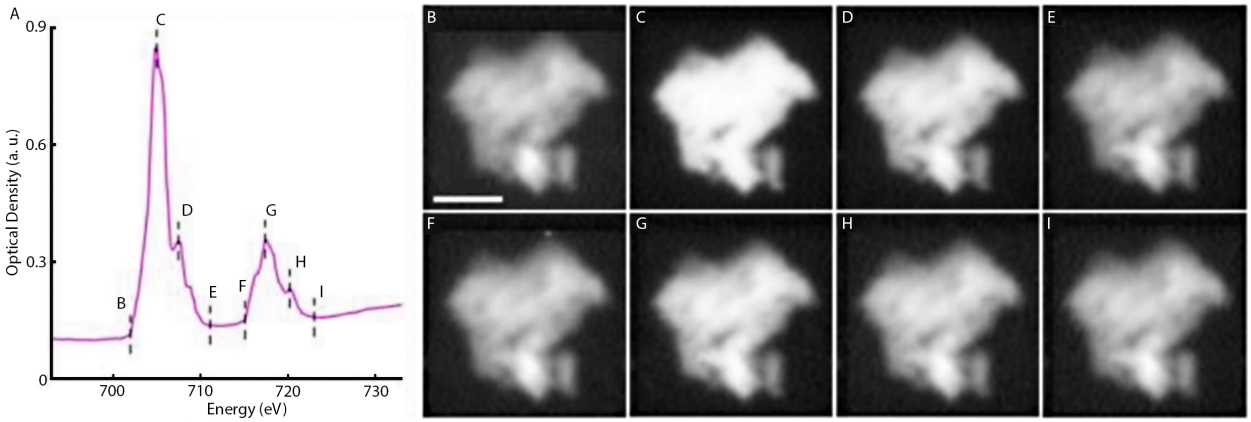

Figure 6.2: **Fe STXM Spectromicroscopy**. (a) The Fe X-ray absorption spectrum generated from STXM energy scans across the Fe L_3 edge. (b-i) The corresponding STXM images at various point along the spectrum (dashed lines in (a)). A drastic change in the absorption throughout the meteorite grain is seen in the on resonance image (c) as Fe is distributed throughout the grain. Adapted from [202].

PCA generated spectra for the four major elements in the grain are shown in Fig. 6.3. The Al K edge spectrum agreed well with previously published spectrum of Al_2O_3 [207] and the Mg K edge spectrum was consistent with those of magnesium silicates [208]. Similarly, the extracted Ni $L_{2/3}$ edge is similar to those of synthetic nickel sulfide and pure nickel [209, 210]. Two unique spectra for Fe were found from PCA (Fig. 6.3 (b)). These spectra closely match previously published reference spectra of iron sulfide and iron silicate, corresponding to different oxidation states of Fe [211]. The recovered iron silicate spectra is shown in Fig. 6.3 (b), solid purple line and iron sulfide is displayed in Fig 6.3 (b), dashed yellow line. The two major absorption peaks in the Fe L-edge are labeled L_{3a} and L_{3b}.

6.4 Ptychography Data Analysis

Ptychography images of the Allende meteorite were initially reconstructed at COSMIC using the distributed GPU-based ptychographic solver SHARP provided by the ALS [212]. The high-speed data transfer and collective computing power granted by the ALS GPU-cluster allowed for near-real time feedback during data collection, but came at the expense of carefully pre-processing

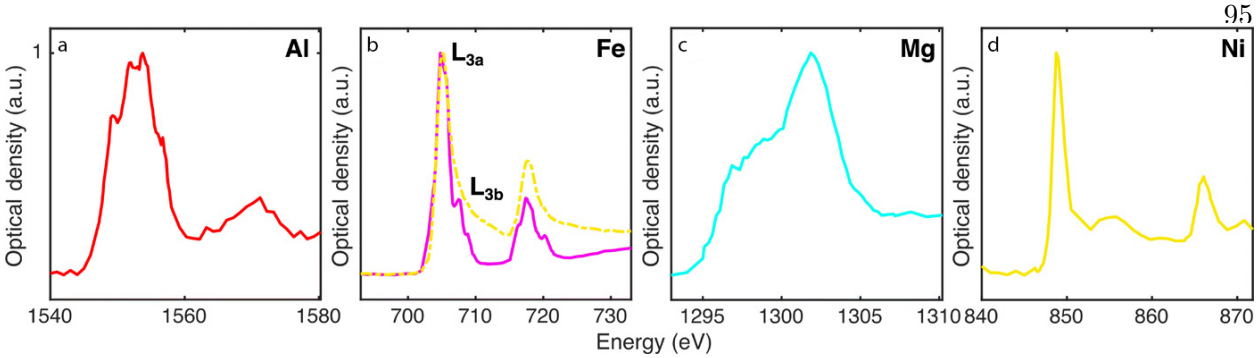

Figure 6.3: **STXM Absorption Spectra**. Absorption spectra generated from STXM energy scans across absorption edges of (a) Al, (b) Fe, (c) Mg, and (d) Ni. Each spectra reveals the unique spectral fingerprint left by each element present in the meteorite grain. The relative peak intensities between the Fe L_{3a} and L_{3b} suggest that Fe^{2+} is the predominant chemical species of Fe in the sample. Adapted from [202].

data to remove artifacts and tuning algorithm parameters to maximize reconstruction quality. Each ptychography dataset was reprocessed to account for beamline intensity fluctuations and to remove background noise on the detector. Images were then reconstructed using a parallel ptychography algorithm with an update condition derived from the hybrid projection-reflection algorithm [213]. Reconstructions of each dataset ran for 5,000 iterations, with the probe update turned on after iteration 5 and continuing for the remaining iterations.

High fidelity, complex images were reconstructed on and below the absorption resonance for Al, Fe, Mg, and Ni; the four main elements composing the meteorite grain. Fig. 6.4 shows the reconstructed amplitude images of the four elements on (a-d) and pre- (e-h) edge. By dividing the on-edge and pre-edge absorption images, the spatial dispersion of each element is revealed with both high contrast and spatial resolution, shown in Fig. 6.5. The spatial resolution of the reconstructed images was estimated using a 10 - 90 knife edge test. The test is shown in Fig. 6.6, giving a lateral resolution of approximately 20 nm. The resolution varies across the different images as the image resolution is energy dependent.

The quantitative information available from ptychography CDI comes in the form of the reconstructed amplitude and phase of the complex transmission or reflection function of a sample. In general, this function is dependent on not only material properties, such as the complex refractive

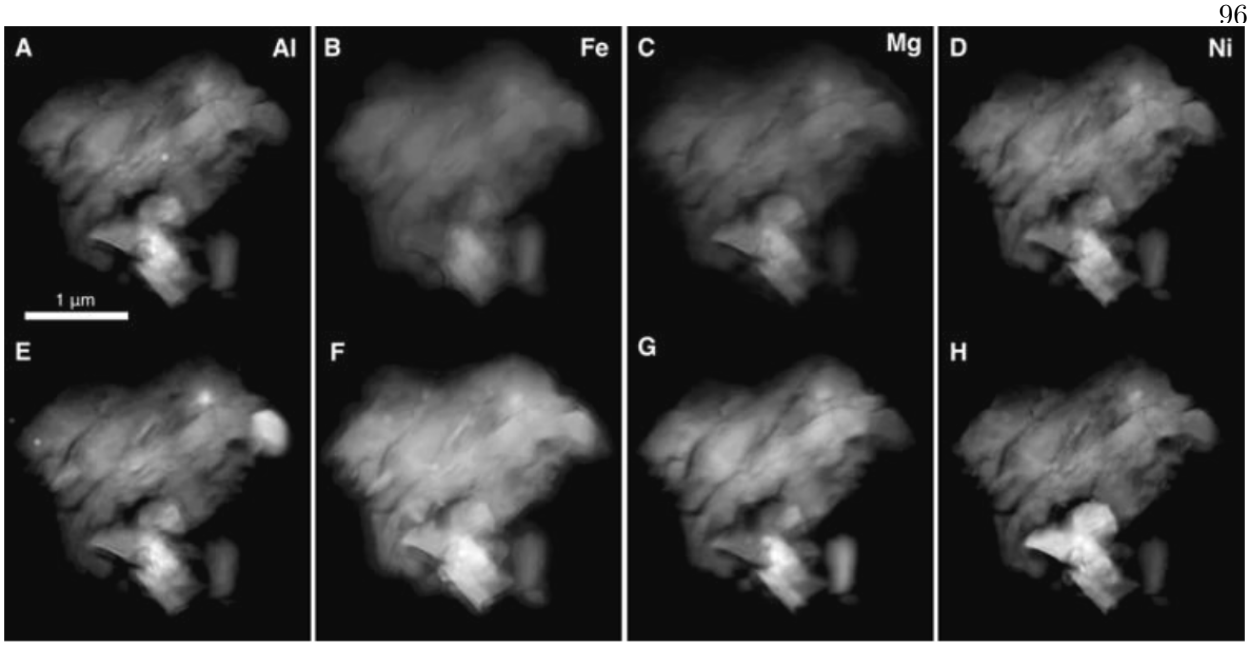

Figure 6.4: **Ptychography Amplitude Reconstructions Near Al, Fe, Mg, and Ni Absorption Edges**. Amplitude reconstructions from ptychography data obtained across the absorption edges of the four main elements in the meteorite grain. (a-d) Pre-edge images at energies 1,545.5 eV, 700 eV, 1,295 eV, 842 eV, respectively. (e-h) On-edge images at energies: 1,551 eV, 707 eV, 1,302 eV, 848 eV. Reproduced from [202].

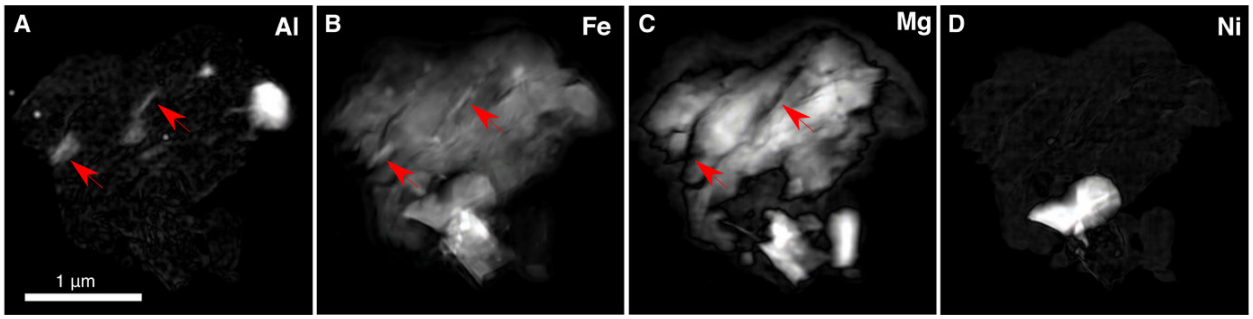

Figure 6.5: **X-ray Ptychography Absorption Contrast**. The four major elements composing the Allende meteorite grain are localized with high contrast and spatial resolution by dividing the pre-edge and on-edge amplitude images at the Al, Fe, Mg, and Ni edges shown in 6.4. The red arrows in (a-c) indicate the locations of Al melt pockets in the meteorite grain. This high contrast viewing method highlights the presence of Fe in these pockets as well as the absence of Mg. Reproduced from [202].

index n, but also sample material thickness and density. To eliminate this sample ambiguity, the scattering quotient of the complex transmission function is examined [214–216]. The scattering quotient is defined as $f_q \equiv \frac{\ln|T(\boldsymbol{x};E)|}{\phi(\boldsymbol{x};E)} = \frac{\sum_i N_i(\boldsymbol{x})\beta_i(E)}{\sum_i N_i(\boldsymbol{x})\delta_i(E)}$. Here, $|T(\boldsymbol{x};E)|$ and $\phi(\boldsymbol{x};E)$ are the complex

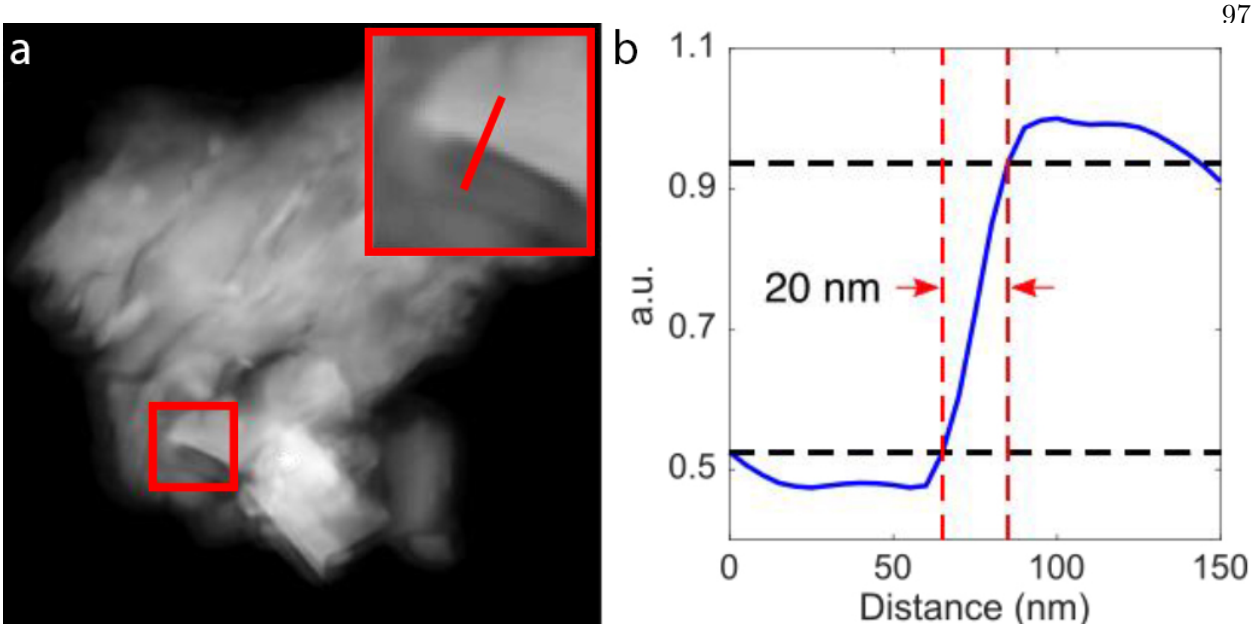

Figure 6.6: **Spatial Resolution of Ptychography Reconstructions**. Knife-edge resolution test of ptychographic absorption reconstruction at the Fe L_3 edge. Spatial resolution is quantified at 20nm using the 10-90 criterion. Adapted from [202].

transmission function amplitude ($0 \leqslant |T(\boldsymbol{x}; E)| \leqslant 1$) and phase retardation ($\phi(\boldsymbol{x}; E) \leqslant 0$) produced via ptychographic reconstruction at photon energy E and spatial location $\boldsymbol{x}$, N_i is the atomic number density of the i^{th} element in the sample, and δ and β are the real and imaginary parts of the complex refractive index, $n = 1 - \delta + i\beta$.

Referring to the relation between the complex transmission function and the complex refractive index in section 1.3, the scattering quotient is independent of effects due to sample thickness variation [216, 217]. This feature makes the scattering quotient uniquely well suited for studying heterogeneous materials where it is difficult to tease apart changes due to thickness variations from those due to a changing material composition. In the case of two dimensional images, the corresponding pixel values of the scattering quotient maps are averages along projections through the sample. Viewed in this way, the scattering quotient offers a novel contrast mechanism sensitive only to sample composition changes [218, 219].

Scattering quotient maps for the on and pre-edge ptychography reconstructions were calculated for Al, Fe, Mg, and Ni. Fig 6.7 shows this alternate contrast mechanism to visualize sample

composition independent of variations in sample thickness.

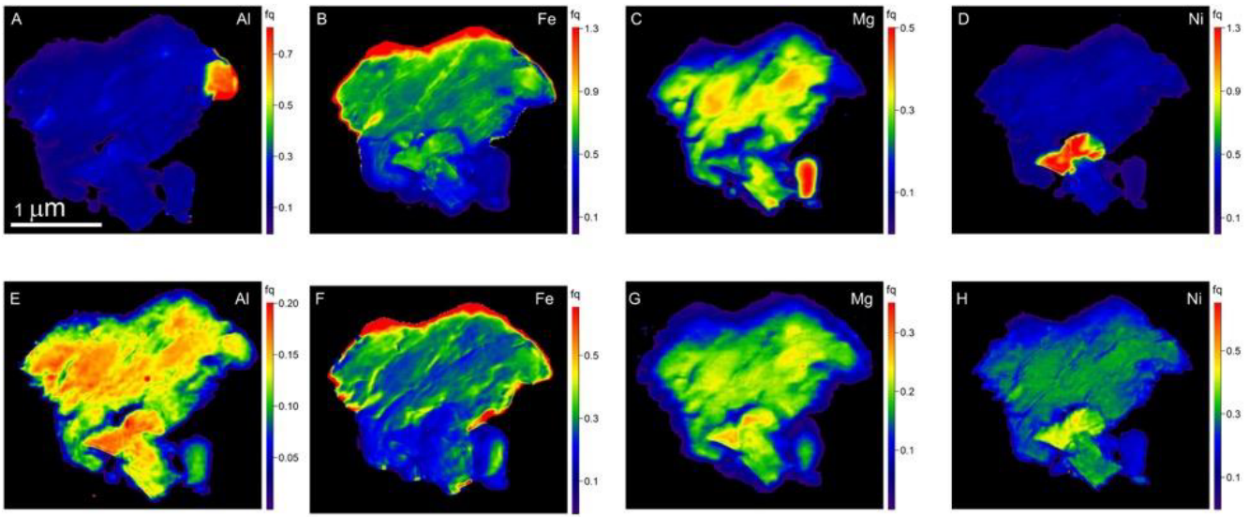

Figure 6.7: **Scattering Quotient Maps of Ptychography Reconstructions**. Novel contrast is gained by calculating the scattering quotient map from the meteorite grain ptychography reconstructions. (a-d) Scattering quotient images calculated from on-edge reconstruction. (e-h) Quotient maps calculated from pre-edge data. Reproduced from [202].

6.5 Discussion and Conclusion

Specific, local chemical and elemental composition information is extracted from the X-ray images. From this information, specific mineral phases of the meteorite grain can be inferred with 20 nm spatial resolution. X-ray absorption spectra extracted from the meteorite grain for Al, Mg, and Ni are consistent with with previous measurements of their respective mineral phases in the literature. Two dominant spectra were recovered from the Fe X-ray absorption analysis, corresponding to iron sulfide and iron silicate. In the case of iron silicates, the relative intensity of the Fe L_{3a} edge spectra are directly related to the redox state of Fe in the meteorite grain. Specifically, the relative intensity of the L_{3a} peak decreases linearly relative to the L_{3b} peak as the ratio of $Fe^{3+}/\sum Fe$ decreases [220]. Since L_{3a} has a higher peak intensity than L_{3b}, it is concluded that the the majority of Fe in iron silicate is in the reduced form Fe^{2+}. This narrows the potential mineral candidates present in the grain.

X-ray ptychography images provide high resolution textural information that provide insight

to the processes acting on the Allende parent body during and after accretion. In particular, shock veins indicate that the meteorite, at some point, experienced impact-induced heating, melting, and cracking [221]. The observation of nanoscopic Fe and Al veins in the larger silicate matrix provides strong evidence of melts from impact shocks or heat-induced metamorphism [222, 223]. The absence of Mg from these veins (Fig. 6.5(c)) indicates that no melting of phases including Mg occurred.

Information extracted about the Allende meteorite agrees well with previous studies using lower resolution techniques [224, 225]. However, the finer details offered by these advanced X-ray microscopy techniques allow for the study of fine-grained matrix material and the observation of melt channels unobservable at coarser resolutions. In particular, the Allende meteorite is classified as shock stage 1, or unshocked, but its parent body must have undergone impact events during accretion and later to eject meteorites. The nanoscale melt channel observed here may provide evidence of these impacts and future studies can constrain the timing and pressures of these events (i.e. pre-accretion vs. post-accretion).

High resolution X-ray ptychography and STXM absorption microscopy were used to study a piece of the Allende CV3 carbonaceous chondrite meteorite. The multidimensional data provides local chemical and textural information on the heterogeneous composition of the meteorite grain. Work presented here is part of a larger correlative microscopy project where additional insight is gained by imaging the same meteorite grain with using TEM. Further information is derived from ptychography data using a newly-developed semi-quantitative analysis method to convert scattering quotient maps to two-element ratio maps given a fixed amount of a third element [202, 226].

Chapter 7

Conclusions and Future Work

7.1 Summary

In the last decade, coherent diffractive imaging (chapter 3) has grown into a mature, general-purpose imaging method of coherent EUV and X-ray light sources (chapter 2). In particular, the robust reconstruction methods of ptychography CDI leverages the redundancy in many overlapping diffraction measurements to produce a high quality, complex transmittance or reflectance map of a sample. This thesis described work to expand the capabilities and improve the performance of coherent diffractive imaging techniques for both tabletop EUV and facility-scale X-ray sources.

By using multiple, illuminating probes (chapter 4), the throughput of a ptychography CDI system is dramatically increased. Furthermore, using spatially separated beams with orthogonal modes allows for spectral, and polarization resolved imaging, with all wavelengths and polarizations resolved in a single scan. Additionally, temporal multiplexing will enable the simultaneous measurement of multiple frames of a nanoscale dynamic system.

The ideas of multiple beam ptychography can be expanded to make use of mutually coherent probes (chapter 5). In this modality, aliasing is strategically used to remove the need for mutually incoherent probes for multiple beam ptychography. Thus easing the experimental requirements for high throughput, large field of view ptychography CDI.

A high resolution ptychography CDI microscope was recently commissioned at the Advanced Light Source (chapter 6). This microscope combines decades of engineering from electron microscopy with a high brightness synchrotron light source to create a ptychography CDI system ca-

pable of spectromicroscopy with nanometer resolution. This microscope is used to spectroscopically image a granule from the Allende meteorite with unprecedented resolution. The multidimensional data provides local chemical and textural information of the heterogeneous meteorite sample.

7.2 Future Work

Work presented in this thesis represents first steps toward efficient, versatile ptychography CDI microscopy. Techniques and principles outline in this work can be readily combined with existing methods to build more flexible imaging systems suitable for a wide range of samples and length scales.

Ongoing research in algorithm development stands to improve the performance of multiple beam ptychography. Recently, an algorithm was proposed that will enable CDI on the attosecond time scale [227]. This algorithm provides a leap in the performance of multiple mode ptychography algorithms, which directly translates to the performance of the multiple beam ptychography technique. An improved performance allows for a larger number of simultaneous probes, increasing the throughput during data acquisition. Furthermore, development of HHG and X-ray sources resulting in more than one beam is ongoing which is immediately useful for a multiple beam ptychography imaging system [178, 179].

As the stability and performance of short wavelength coherent source continues, the performance of CDI systems will advanced with them. In particular, the resolution of these imaging systems is increased by using shorter wavelength illumination or increasing the NA. For certain spectromicroscopy applications, imaging with a particular wavelength to observe an absorption feature is necessary. Thus, if smaller features want to be studied, the NA of the microscope must be increased. This can present significant engineering challenges as the CDI systems become increasingly and necessarily compact. Nevertheless, the highest wavelength-to-resolution CDI system was recently demonstrated using as 13nm HHG source [71], where sub-wavelength resolution was reported by increasing the NA of an EUV ptychography CDI microscope. The combination of high NA imaging with CDI techniques has the potential to provide tabletop EUV coherent microscopes

capable of resolving nanometer-scale features with unprecedented temporal resolution.

Finally, a challenging but exciting frontier in nanoscale imaging comes in the form of correlative, real-time CDI. Many natural systems are comprised of heterogeneous structures with a hierarchical organization. Despite advancements in imaging technology, there is no one technique capable of characterizing a sample so that the macroscopic properties are fully understood in terms of microscopic structure and function. Instead, a hybrid imaging approach that incorporates EUV and X-ray, electron, and visible imaging modalities can leverage the advantages of each system in a complimentary manner. For example, visible microscopy is used to scan a large field of view at lower resolution to determine areas of interest for higher resolution electron or X-ray imaging. This process is further streamlined if a system capable of these three imaging modalities share a common sample holder that can quickly switch between the desired imaging modality without the need of a sample transfer.

Still, system throughput of X-ray and EUV imaging is largely limited by camera readout rates, where a ptychography scan consisting of less than one minute of exposure time can take thirty minutes or more to collect because of the detector readout. Fortunately, coming advancements in X-ray and EUV CMOS technology coupled with advancements in distributed GPU reconstruction algorithms [142, 228, 229] pave the way toward video-rate full-field nano-imaging.

Bibliography

[1] William J Croft. Under the microscope: a brief history of microscopy, volume 5. World Scientific, 2006.

[2] Christina Karlsson Rosenthal, A Heinrichs, N Gray, N Rusk, N Blow, and K Baumann. Milestones in light microscopy. Nature Cell Biol, 11:S6–S7, 2009.

[3] Robert Hooke. Micrographia: or some physiological descriptions of minute bodies made by magnifying glasses, with observations and inquiries thereupon. Courier Corporation, 2003.

[4] Ernst Abbe. Beiträge zur theorie des mikroskops und der mikroskopischen wahrnehmung. Archiv für mikroskopische Anatomie, 9(1):413–468, 1873.

[5] Eric Betzig, A Lewis, A Harootunian, M Isaacson, and E Kratschmer. Near field scanning optical microscopy (nsom): development and biophysical applications. Biophysical journal, 49(1):269–279, 1986.

[6] Stefan W Hell and Jan Wichmann. Breaking the diffraction resolution limit by stimulated emission: stimulated-emission-depletion fluorescence microscopy. Optics letters, 19(11):780–782, 1994.

[7] Michael J Rust, Mark Bates, and Xiaowei Zhuang. Sub-diffraction-limit imaging by stochastic optical reconstruction microscopy (storm). Nature methods, 3(10):793–796, 2006.

[8] Jeff Squier and Michiel Müller. High resolution nonlinear microscopy: A review of sources and methods for achieving optimal imaging. Review of Scientific Instruments, 72(7):2855–2867, 2001.

[9] Agnes Bogner, P-H Jouneau, Gilbert Thollet, D Basset, and Catherine Gauthier. A history of scanning electron microscopy developments: Towards wet-stem imaging. Micron, 38(4): 390–401, 2007.

[10] Knut W Urban. Is science prepared for atomic-resolution electron microscopy? Nature materials, 8(4):260–262, 2009.

[11] Wilhelm Conrad Röntgen. On a new kind of rays. Science, 3(59):227–231, 1896.

[12] John David Jackson. Classical electrodynamics. John Wiley & Sons, 2007.

[13] Peter K Spiegel. The first clinical x-ray made in america–100 years. AJR. American journal of roentgenology, 164(1):241–243, 1995.

[14] William Henry Bragg and William Lawrence Bragg. X rays and crystal structure. G. Bell, 1924.

[15] Reginald William James. The optical principles of the diffraction of x-rays. 1954.

[16] Arthur Holly Compton, Samuel King Allison, et al. X-rays in theory and experiment. 1935.

[17] Edwin M McMillan. The synchrotron - a proposed high energy particle accelerator. Physical Review, 68(5-6):143, 1945.

[18] A McPherson, G Gibson, H Jara, U Johann, Ting S Luk, IA McIntyre, Keith Boyer, and Charles K Rhodes. Studies of multiphoton production of vacuum-ultraviolet radiation in the rare gases. JOSA B, 4(4):595–601, 1987.

[19] Andy Rundquist, Charles G Durfee, Zenghu Chang, Catherine Herne, Sterling Backus, Margaret M Murnane, and Henry C Kapteyn. Phase-matched generation of coherent soft x-rays. Science, 280(5368):1412–1415, 1998.

[20] Randy A Bartels, Ariel Paul, Hans Green, Henry C Kapteyn, Margaret M Murnane, Sterling Backus, Ivan P Christov, Yanwei Liu, David Attwood, and Chris Jacobsen. Generation of spatially coherent light at extreme ultraviolet wavelengths. Science, 297(5580):376–378, 2002.

[21] Tenio Popmintchev, Ming-Chang Chen, Alon Bahabad, Michael Gerrity, Pavel Sidorenko, Oren Cohen, Ivan P Christov, Margaret M Murnane, and Henry C Kapteyn. Phase matching of high harmonic generation in the soft and hard x-ray regions of the spectrum. Proceedings of the National Academy of Sciences, 106(26):10516–10521, 2009.

[22] Tenio Popmintchev, Ming-Chang Chen, Dimitar Popmintchev, Paul Arpin, Susannah Brown, Skirmantas Ališauskas, Giedrius Andriukaitis, Tadas Balčiunas, Oliver D Mücke, Audrius Pugzlys, Andrius Baltuska, Bonggu Shim, Samuel E Schrauth, Alexander Gaeta, Carlos Hernndez-Garca, Luis Plaja, Andreas Becker, Agnieszka Jaron-Becker, Margaret M Murnane, and Henry C Kapteyn. Bright coherent ultrahigh harmonics in the kev x-ray regime from mid-infrared femtosecond lasers. Science, 336(6086):1287–1291, 2012.

[23] David Attwood and Anne Sakdinawat. X-rays and extreme ultraviolet radiation: principles and applications. Cambridge university press, 2017.

[24] Gene E Ice, John D Budai, and Judy WL Pang. The race to x-ray microbeam and nanobeam science. Science, 334(6060):1234–1239, 2011.

[25] Anatoly Snigirev, Victor Kohn, Irina Snigireva, and Bruno Lengeler. A compound refractive lens for focusing high-energy x-rays. Nature, 384(6604):49–51, 1996.

[26] Alexey Bosak, Irina Snigireva, Kirill S Napolskii, and Anatoly Snigirev. High-resolution transmission x-ray microscopy: A new tool for mesoscopic materials. Advanced Materials, 22 (30):3256–3259, 2010.

[27] Albert V Baez. Fresnel zone plate for optical image formation using extreme ultraviolet and soft x radiation. JOSA, 51(4):405–412, 1961.

[28] Weilun Chao, Jihoon Kim, Senajith Rekawa, Peter Fischer, and Erik H Anderson. Demonstration of 12 nm resolution fresnel zone plate lens based soft x-ray microscopy. Optics Express, 17(20):17669–17677, 2009.

[29] Ray Conley, Chian Liu, Jun Qian, Cameron M Kewish, Albert T Macrander, Hanfei Yan, Hyon Chol Kang, Jörg Maser, and G Brian Stephenson. Wedged multilayer laue lens. Review of Scientific Instruments, 79(5):053104, 2008.

[30] M Prasciolu, AFG Leontowich, J Krzywinski, A Andrejczuk, HN Chapman, and S Bajt. Fabrication of wedged multilayer laue lenses. Optical Materials Express, 5(4):748–755, 2015.

[31] Paul Kirkpatrick and Albert Vincio Baez. Formation of optical images by x-rays. JOSA, 38 (9):766–774, 1948.

[32] C Jacobsen, S Williams, E Anderson, MT Browne, CJ Buckley, D Kern, J Kirz, M Rivers, and X Zhang. Diffraction-limited imaging in a scanning transmission x-ray microscope. Optics Communications, 86(3-4):351–364, 1991.

[33] Anne Sakdinawat and David Attwood. Nanoscale x-ray imaging. Nature photonics, 4(12): 840, 2010.

[34] Xiaojing Huang, Huijie Miao, Jan Steinbrener, Johanna Nelson, David Shapiro, Andrew Stewart, Joshua Turner, and Chris Jacobsen. Signal-to-noise and radiation exposure considerations in conventional and diffraction x-ray microscopy. Optics Express, 17(16):13541–13553, 2009.

[35] Jianwei Miao, Tetsuya Ishikawa, Ian K Robinson, and Margaret M Murnane. Beyond crystallography: Diffractive imaging using coherent x-ray light sources. Science, 348(6234):530–535, 2015.

[36] Joseph W Goodman. Introduction to Fourier optics. Roberts and Company Publishers, 2005.

[37] Max Born and Emil Wolf. Principles of optics: electromagnetic theory of propagation, interference and diffraction of light. Elsevier, 2013.

[38] David Paganin. Coherent X-ray optics. Number 6. Oxford University Press on Demand, 2006.

[39] John Maxwell Cowley. Diffraction physics. Elsevier, 1995.

[40] Friso Van der Veen and Franz Pfeiffer. Coherent x-ray scattering. Journal of Physics: Condensed Matter, 16(28):5003, 2004.

[41] Dennis F Gardner, Bosheng Zhang, Matthew D Seaberg, Leigh S Martin, Daniel E Adams, Farhad Salmassi, Eric Gullikson, Henry Kapteyn, and Margaret Murnane. High numerical aperture reflection mode coherent diffraction microscopy using off-axis apertured illumination. Optics express, 20(17):19050–19059, 2012.

[42] Matthew D Seaberg, Bosheng Zhang, Dennis F Gardner, Elisabeth R Shanblatt, Margaret M Murnane, Henry C Kapteyn, and Daniel E Adams. Tabletop nanometer extreme ultraviolet imaging in an extended reflection mode using coherent fresnel ptychography. Optica, 1(1): 39–44, 2014.

[43] Christina L Porter, Michael Tanksalvala, Michael Gerrity, Galen Miley, Xiaoshi Zhang, Charles Bevis, Elisabeth Shanblatt, Robert Karl, Margaret M Murnane, Daniel E Adams, et al. General-purpose, wide field-of-view reflection imaging with a tabletop 13 nm light source. Optica, 4(12):1552–1557, 2017.

[44] Burton L Henke, Eric M Gullikson, and John C Davis. X-ray interactions: photoabsorption, scattering, transmission and reflection e= 50-30,000 ev, z= 1-92. Atomic data and nuclear data tables, 54(2), 1993.

[45] Jens Als-Nielsen and Des McMorrow. Elements of modern X-ray physics. John Wiley & Sons, 2011.

[46] Pierre Thibault, Martin Dierolf, Andreas Menzel, Oliver Bunk, Christian David, and Franz Pfeiffer. High-resolution scanning x-ray diffraction microscopy. Science, 321(5887):379–382, 2008.

[47] JM Rodenburg and RHT Bates. The theory of super-resolution electron microscopy via wigner-distribution deconvolution. Philosophical Transactions of the Royal Society of London. Series A: Physical and Engineering Sciences, 339(1655):521–553, 1992.

[48] Esther HR Tsai, Ivan Usov, Ana Diaz, Andreas Menzel, and Manuel Guizar-Sicairos. X-ray ptychography with extended depth of field. Optics express, 24(25):29089–29108, 2016.

[49] Frits Zernike. Phase contrast, a new method for the microscopic observation of transparent objects. Physica, 9(7):686–698, 1942.

[50] VP Nayyar and NK Verma. Two-point resolution of gaussian aperture operating in partially coherent light using various resolution criteria. Applied optics, 17(14):2176–2180, 1978.

[51] CJ Milne, TJ Penfold, and M Chergui. Recent experimental and theoretical developments in time-resolved x-ray spectroscopies. Coordination Chemistry Reviews, 277:44–68, 2014.

[52] Ernest D Courant, M Stanley Livingston, and Hartland S Snyder. The strong-focusing synchrotona new high energy accelerator. Physical Review, 88(5):1190, 1952.

[53] FR Elder, AM Gurewitsch, RV Langmuir, and HC Pollock. Radiation from electrons in a synchrotron. Physical Review, 71(11):829, 1947.

[54] TK Sham and Mark L Rivers. A brief overview of synchrotron radiation. Reviews in mineralogy and geochemistry, 49(1):117–147, 2002.

[55] The Advanced Light Source.

[56] Herman Winick, George Brown, Klaus Halbach, and John Harris. Wiggler and undulator magnets. Physics Today, 34(5):50–63, 1981.

[57] M Ferray, Anne L'Huillier, XF Li, LA Lompre, G Mainfray, and C Manus. Multiple-harmonic conversion of 1064 nm radiation in rare gases. Journal of Physics B: Atomic, Molecular and Optical Physics, 21(3):L31, 1988.

[58] Tingting Fan, Patrik Grychtol, Ronny Knut, Carlos Hernández-García, Daniel D Hickstein, Dmitriy Zusin, Christian Gentry, Franklin J Dollar, Christopher A Mancuso, Craig W Hogle, et al. Bright circularly polarized soft x-ray high harmonics for x-ray magnetic circular dichroism. Proceedings of the National Academy of Sciences, 112(46):14206–14211, 2015.

[59] Cong Chen, Zhensheng Tao, Carlos Hernández-García, Piotr Matyba, Adra Carr, Ronny Knut, Ofer Kfir, Dimitry Zusin, Christian Gentry, Patrik Grychtol, et al. Tomographic reconstruction of circularly polarized high-harmonic fields: 3d attosecond metrology. Science Advances, 2(2):e1501333, 2016.

[60] Daniel D Hickstein, Franklin J Dollar, Patrik Grychtol, Jennifer L Ellis, Ronny Knut, Carlos Hernández-García, Dmitriy Zusin, Christian Gentry, Justin M Shaw, Tingting Fan, et al. Non-collinear generation of angularly isolated circularly polarized high harmonics. Nature Photonics, 9(11):743–750, 2015.

[61] Phoebe Tengdin, Wenjing You, Cong Chen, Xun Shi, Dmitriy Zusin, Yingchao Zhang, Christian Gentry, Adam Blonsky, Mark Keller, Peter M Oppeneer, Henry C Kapteyn, Zhensheng Tao, and Margaret M Murnane. Critical behavior within 20 fs drives the out-of-equilibrium laser-induced magnetic phase transition in nickel. Science advances, 4(3):eaap9744, 2018.

[62] Phoebe Tengdin, Christian Gentry, Adam Blonsky, Dmitriy Zusin, Michael Gerrity, Lukas Hellbrück, Moritz Hofherr, Justin Shaw, Yaroslav Kvashnin, Erna K Delczeg-Czirjak, Monika Arora, Hans Nembach, Tom J Silva, Stefan Mathias, Martin Aeschlimann, Danny Kapteyn, Henry C Thonig, Konstantinos Koumpouras, Olle Eriksson, and Margaret M Murnane. Direct light–induced spin transfer between different elements in a spintronic heusler material via femtosecond laser excitation. Science advances, 6(3):eaaz1100, 2020.

[63] Yingchao Zhang, Xun Shi, Wenjing You, Zhensheng Tao, Yigui Zhong, Fairoja Cheenicode Kabeer, Pablo Maldonado, Peter M Oppeneer, Michael Bauer, Kai Rossnagel, Henry Kapteyn, and Margaret Murnane. Coherent modulation of the electron temperature and electron–phonon couplings in a 2d material. Proceedings of the National Academy of Sciences, 117(16):8788–8793, 2020.

[64] Xun Shi, Wenjing You, Yingchao Zhang, Zhensheng Tao, Peter M Oppeneer, Xianxin Wu, Ronny Thomale, Kai Rossnagel, Michael Bauer, Henry Kapteyn, and Margaret Murnane. Ultrafast electron calorimetry uncovers a new long-lived metastable state in 1t-tase2 mediated by mode-selective electron-phonon coupling. Science advances, 5(3):eaav4449, 2019.

[65] Wenjing You, Phoebe Tengdin, Cong Chen, Xun Shi, Dmitriy Zusin, Yingchao Zhang, Christian Gentry, Adam Blonsky, Mark Keller, Peter M Oppeneer, Henry Kapteyn, Zhensheng Tao, and Margaret Murnane. Revealing the nature of the ultrafast magnetic phase transition in ni by correlating extreme ultraviolet magneto-optic and photoemission spectroscopies. Physical Review Letters, 121(7):077204, 2018.

[66] Zhensheng Tao, Cong Chen, Tibor Szilvási, Mark Keller, Manos Mavrikakis, Henry Kapteyn, and Margaret Murnane. Direct time-domain observation of attosecond final-state lifetimes in photoemission from solids. Science, 353(6294):62–67, 2016.

[67] Kathleen M Hoogeboom-Pot, Jorge N Hernandez-Charpak, Xiaokun Gu, Travis D Frazer, Erik H Anderson, Weilun Chao, Roger W Falcone, Ronggui Yang, Margaret M Murnane, Henry C Kapteyn, et al. A new regime of nanoscale thermal transport: Collective diffusion increases dissipation efficiency. Proceedings of the National Academy of Sciences, 112(16): 4846–4851, 2015.

[68] Travis D Frazer, Joshua L Knobloch, Kathleen M Hoogeboom-Pot, Damiano Nardi, Weilun Chao, Roger W Falcone, Margaret M Murnane, Henry C Kapteyn, and Jorge N Hernandez-Charpak. Engineering nanoscale thermal transport: Size-and spacing-dependent cooling of nanostructures. Physical Review Applied, 11(2):024042, 2019.

[69] Bosheng Zhang, Dennis F. Gardner, Matthew D. Seaberg, Elisabeth R. Shanblatt, Henry C. Kapteyn, Margaret M. Murnane, and Daniel E. Adams. High contrast 3D imaging of surfaces near the wavelength limit using tabletop EUV ptychography. Ultramicroscopy, 158:98–104, 2015.

[70] Elisabeth R Shanblatt, Christina L Porter, Dennis F Gardner, Giulia F Mancini, Robert M Karl Jr, Michael D Tanksalvala, Charles S Bevis, Victor H Vartanian, Henry C Kapteyn, Daniel E Adams, et al. Quantitative chemically specific coherent diffractive imaging of reactions at buried interfaces with few nanometer precision. Nano letters, 16(9):5444–5450, 2016.

[71] Dennis F Gardner, Michael Tanksalvala, Elisabeth R Shanblatt, Xiaoshi Zhang, Benjamin R Galloway, Christina L Porter, Robert Karl Jr, Charles Bevis, Daniel E Adams, Henry C Kapteyn, et al. Subwavelength coherent imaging of periodic samples using a 13.5 nm tabletop high-harmonic light source. Nature Photonics, 11(4):259–263, 2017.

[72] Jeffrey L Krause, Kenneth J Schafer, and Kenneth C Kulander. High-order harmonic generation from atoms and ions in the high intensity regime. Physical Review Letters, 68(24): 3535, 1992.

[73] Maciej Lewenstein, Ph Balcou, M Yu Ivanov, Anne Lhuillier, and Paul B Corkum. Theory of high-harmonic generation by low-frequency laser fields. Physical Review A, 49(3):2117, 1994.

[74] Paul B Corkum. Plasma perspective on strong field multiphoton ionization. Physical review letters, 71(13):1994, 1993.

[75] Tenio Popmintchev, Ming-Chang Chen, Paul Arpin, Margaret M Murnane, and Henry C Kapteyn. The attosecond nonlinear optics of bright coherent x-ray generation. Nature Photonics, 4(12):822–832, 2010.

[76] Georges Ndabashimiye, Shambhu Ghimire, Mengxi Wu, Dana A Browne, Kenneth J Schafer, Mette B Gaarde, and David A Reis. Solid-state harmonics beyond the atomic limit. Nature, 534(7608):520–523, 2016.

[77] U Teubner and Paul Gibbon. High-order harmonics from laser-irradiated plasma surfaces. Reviews of Modern Physics, 81(2):445, 2009.

[78] J Zhou, J Peatross, MM Murnane, HC Kapteyn, and IP Christov. Enhanced high-harmonic generation using 25 fs laser pulses. Physical Review Letters, 76(5):752, 1996.

[79] Charles G Durfee III, Andy R Rundquist, Sterling Backus, Catherine Herne, Margaret M Murnane, and Henry C Kapteyn. Phase matching of high-order harmonics in hollow waveguides. Physical Review Letters, 83(11):2187, 1999.

[80] Andrew R. Rundquist. Phase-matched generation of coherent, ultrafast x-rays using high harmonics. PhD thesis, 1998.

[81] Ariel Paul, Emily A Gibson, Xiaoshi Zhang, Amy Lytle, Tenio Popmintchev, Xibin Zhou, Margaret M Murnane, Ivan P Christov, and Henry C Kapteyn. Phase-matching techniques for coherent soft x-ray generation. IEEE Journal of Quantum Electronics, 42(1):14–26, 2005.

[82] M-C Chen, P Arpin, T Popmintchev, M Gerrity, B Zhang, M Seaberg, D Popmintchev, MM Murnane, and HC Kapteyn. Bright, coherent, ultrafast soft x-ray harmonics spanning the water window from a tabletop light source. Physical Review Letters, 105(17):173901, 2010.

[83] Enrique AJ Marcatili and RA Schmeltzer. Hollow metallic and dielectric waveguides for long distance optical transmission and lasers. Bell System Technical Journal, 43(4):1783–1809, 1964.

[84] Jianwei Miao, David Sayre, and HN Chapman. Phase retrieval from the magnitude of the fourier transforms of nonperiodic objects. JOSA A, 15(6):1662–1669, 1998.

[85] IK Robinson, JL Libbert, IA Vartanyants, JA Pitney, DM Smilgies, DL Abernathy, and G Grübel. Coherent x-ray diffraction imaging of silicon oxide growth. Physical Review B, 60 (14):9965, 1999.

[86] Mark A Pfeifer, Garth J Williams, Ivan A Vartanyants, Ross Harder, and Ian K Robinson. Three-dimensional mapping of a deformation field inside a nanocrystal. Nature, 442(7098): 63–66, 2006.

[87] Ian K Robinson, Ivan A Vartanyants, GJ Williams, MA Pfeifer, and JA Pitney. Reconstruction of the shapes of gold nanocrystals using coherent x-ray diffraction. Physical review letters, 87(19):195505, 2001.

[88] GJ Williams, MA Pfeifer, IA Vartanyants, and IK Robinson. Three-dimensional imaging of microstructure in au nanocrystals. Physical review letters, 90(17):175501, 2003.

[89] Brian Abbey, Garth J Williams, Mark A Pfeifer, Jesse N Clark, Corey T Putkunz, Angela Torrance, Ian McNulty, TM Levin, Andrew G Peele, and Keith A Nugent. Quantitative coherent diffractive imaging of an integrated circuit at a spatial resolution of 20 nm. Applied Physics Letters, 93(21):214101, 2008.

[90] Mirko Holler, Manuel Guizar-Sicairos, Esther HR Tsai, Roberto Dinapoli, Elisabeth Müller, Oliver Bunk, Jörg Raabe, and Gabriel Aeppli. High-resolution non-destructive three-dimensional imaging of integrated circuits. Nature, 543(7645):402–406, 2017.

[91] Martin Dierolf, Andreas Menzel, Pierre Thibault, Philipp Schneider, Cameron M Kewish, Roger Wepf, Oliver Bunk, and Franz Pfeiffer. Ptychographic x-ray computed tomography at the nanoscale. Nature, 467(7314):436–439, 2010.

[92] Peter D Baksh, Michal Ostrčil, Magdalena Miszczak, Charles Pooley, Richard T Chapman, Adam S Wyatt, Emma Springate, John E Chad, Katrin Deinhardt, Jeremy G Frey, et al. Quantitative and correlative extreme ultraviolet coherent imaging of mouse hippocampal neurons at high resolution. Science Advances, 6(18):eaaz3025, 2020.

[93] Henry N Chapman and Keith A Nugent. Coherent lensless x-ray imaging. Nature photonics, 4(12):833–839, 2010.

[94] Eugene Hecht. Optics. Pearson Education India, 2002.

[95] J. C. H. Spence, U. Weierstall, and M. Howells. Coherence and sampling requirements for diffractive imaging. Ultramicroscopy, 101(2-4):149–52, nov 2004. ISSN 0304-3991. doi: 10.1016/j.ultramic.2004.05.005.

[96] Joseph W Goodman. Statistical optics. John Wiley & Sons, 2015.

[97] Claude Elwood Shannon. Communication in the presence of noise. Proceedings of the IRE, 37(1):10–21, 1949.

[98] Eric Stade. Fourier analysis, volume 109. John Wiley & Sons, 2011.

[99] David Sayre. Some implications of a theorem due to shannon. Acta Crystallographica, 5(6): 843–843, 1952.

[100] D Sayre. Prospects for long-wavelength x-ray microscopy and diffraction. In Imaging Processes and Coherence in Physics, pages 229–235. Springer, 1980.

[101] Jianwei Miao, Pambos Charalambous, Janos Kirz, and David Sayre. Extending the methodology of x-ray crystallography to allow imaging of micrometre-sized non-crystalline specimens. Nature, 400(6742):342–344, 1999.

[102] Jianwei Miao and D Sayre. On possible extensions of x-ray crystallography through diffraction-pattern oversampling. Acta Crystallographica Section A: Foundations of Crystallography, 56(6):596–605, 2000.

[103] Jianwei Miao, Tetsuya Ishikawa, Erik H Anderson, and Keith O Hodgson. Phase retrieval of diffraction patterns from noncrystalline samples using the oversampling method. Physical Review B, 67(17):174104, 2003.

[104] Veit Elser. Phase retrieval by iterated projections. JOSA A, 20(1):40–55, 2003.

[105] D Russell Luke, James V Burke, and Richard G Lyon. Optical wavefront reconstruction: Theory and numerical methods. SIAM review, 44(2):169–224, 2002.

[106] Stefano Marchesini. Invited article: A unified evaluation of iterative projection algorithms for phase retrieval. Review of scientific instruments, 78(1):011301, 2007.

[107] James R Fienup. Phase retrieval algorithms: a comparison. Applied optics, 21(15):2758–2769, 1982.

[108] Heinz H Bauschke, Patrick L Combettes, and D Russell Luke. Phase retrieval, error reduction algorithm, and fienup variants: a view from convex optimization. JOSA A, 19(7):1334–1345, 2002.

[109] Ralph W Gerchberg. A practical algorithm for the determination of phase from image and diffraction plane pictures. Optik, 35:237–246, 1972.

[110] R Bates. Fourier phase problems are uniquely solvable in mute than one dimension. i: Underlying theory. Optik (Stuttgart), 61(247-262):5, 1982.

[111] James R Fienup. Reconstruction of an object from the modulus of its fourier transform. Optics letters, 3(1):27–29, 1978.

[112] Stefano Marchesini, H He, Henry N Chapman, Stefan P Hau-Riege, Aleksandr Noy, Malcolm R Howells, Uwe Weierstall, and John CH Spence. X-ray image reconstruction from a diffraction pattern alone. Physical Review B, 68(14):140101, 2003.

[113] Brian Abbey, Keith A Nugent, Garth J Williams, Jesse N Clark, Andrew G Peele, Mark A Pfeifer, Martin De Jonge, and Ian McNulty. Keyhole coherent diffractive imaging. Nature Physics, 4(5):394–398, 2008.

[114] Bosheng Zhang, Matthew D Seaberg, Daniel E Adams, Dennis F Gardner, Elisabeth R Shanblatt, Justin M Shaw, Weilun Chao, Eric M Gullikson, Farhad Salmassi, Henry C Kapteyn, et al. Full field tabletop euv coherent diffractive imaging in a transmission geometry. Optics Express, 21(19):21970–21980, 2013.

[115] Tetsuo Harada, Junki Kishimoto, Takeo Watanabe, Hiroo Kinoshita, and Dong Gun Lee. Mask observation results using a coherent extreme ultraviolet scattering microscope at newsubaru. Journal of Vacuum Science & Technology B: Microelectronics and Nanometer Structures Processing, Measurement, and Phenomena, 27(6):3203–3207, 2009.

[116] Dennis F Gardner, Bosheng Zhang, Matthew D Seaberg, Leigh S Martin, Daniel E Adams, Farhad Salmassi, Eric Gullikson, Henry Kapteyn, and Margaret Murnane. High numerical aperture reflection mode coherent diffraction microscopy using off-axis apertured illumination. Optics express, 20(17):19050–19059, 2012.

[117] D Russell Luke. Relaxed averaged alternating reflections for diffraction imaging. Inverse problems, 21(1):37, 2004.

[118] Stefano Marchesini. Phase retrieval and saddle-point optimization. JOSA A, 24(10):3289–3296, 2007.

[119] Ferréol Soulez, Éric Thiébaut, Antony Schutz, André Ferrari, Frédéric Courbin, and Michael Unser. Proximity operators for phase retrieval. Applied optics, 55(26):7412–7421, 2016.

[120] JR Fienup and CC Wackerman. Phase-retrieval stagnation problems and solutions. JOSA A, 3(11):1897–1907, 1986.

[121] John M Rodenburg. Ptychography and related diffractive imaging methods. Advances in imaging and electron physics, 150:87–184, 2008.

[122] JM Rodenburg. Ptychography: early history and 3d scattering effects. In Short-Wavelength Imaging and Spectroscopy Sources, volume 8678, page 867809. International Society for Optics and Photonics, 2012.

[123] Walter Hoppe. Beugung im inhomogenen primärstrahlwellenfeld. i. prinzip einer phasenmessung von elektronenbeungungsinterferenzen. Acta Crystallographica Section A: Crystal Physics, Diffraction, Theoretical and General Crystallography, 25(4):495–501, 1969.

[124] Reiner Hegerl and W Hoppe. Dynamische theorie der kristallstrukturanalyse durch elektronenbeugung im inhomogenen primärstrahlwellenfeld. Berichte der Bunsengesellschaft für physikalische Chemie, 74(11):1148–1154, 1970.

[125] R Hegerl and W Hoppe. Phase evaluation in generalized diffraction (ptychography). Proc. Fifth Eur. Cong. Electron Microscopy, pages 628–629, 1972.

[126] W Hoppe et al. Trace structure analysis, ptychography, phase tomography. Ultramicroscopy, 10(3):187–198, 1982.

[127] PD Nellist, BC McCallum, and John M Rodenburg. Resolution beyond the'information limit'in transmission electron microscopy. Nature, 374(6523):630–632, 1995.

[128] RHT Bates and JM Rodenburg. Sub-ångström transmission microscopy: a fourier transform algorithm for microdiffraction plane intensity information. Ultramicroscopy, 31(3):303–307, 1989.

[129] BC McCallum and JM Rodenburg. Two-dimensional demonstration of wigner phase-retrieval microscopy in the stem configuration. Ultramicroscopy, 45(3-4):371–380, 1992.

[130] JM Rodenburg, BC McCallum, and PD Nellist. Experimental tests on double-resolution coherent imaging via stem. Ultramicroscopy, 48(3):304–314, 1993.

[131] Henry N Chapman. Phase-retrieval x-ray microscopy by wigner-distribution deconvolution. Ultramicroscopy, 66(3-4):153–172, 1996.

[132] Henry N Chapman. Phase-retrieval x-ray microscopy by wigner-distribution deconvolution: signal processing. Scanning Microscopy, 11:67–80, 1997.

[133] Helen Mary Louise Faulkner and JM Rodenburg. Movable aperture lensless transmission microscopy: a novel phase retrieval algorithm. Physical review letters, 93(2):023903, 2004.

[134] Manuel Guizar-Sicairos and James R Fienup. Phase retrieval with transverse translation diversity: a nonlinear optimization approach. Optics express, 16(10):7264–7278, 2008.

[135] John M Rodenburg and Helen ML Faulkner. A phase retrieval algorithm for shifting illumination. Applied physics letters, 85(20):4795–4797, 2004.

[136] Andrew M Maiden and John M Rodenburg. An improved ptychographical phase retrieval algorithm for diffractive imaging. Ultramicroscopy, 109(10):1256–1262, 2009.

[137] Pierre Thibault, Martin Dierolf, Oliver Bunk, Andreas Menzel, and Franz Pfeiffer. Probe retrieval in ptychographic coherent diffractive imaging. Ultramicroscopy, 109(4):338–343, 2009.

[138] Pierre Thibault, Martin Dierolf, Andreas Menzel, Oliver Bunk, Christian David, and Franz Pfeiffer. High-resolution scanning x-ray diffraction microscopy. Science, 321(5887):379–382, 2008.

[139] P Thibault and M Guizar-Sicairos. Maximum-likelihood refinement for coherent diffractive imaging. New Journal of Physics, 14(6):063004, 2012.

[140] Andrew Maiden, Daniel Johnson, and Peng Li. Further improvements to the ptychographical iterative engine. Optica, 4(7):736–745, 2017.

[141] Peng Li and Andrew M Maiden. Ten implementations of ptychography. Journal of microscopy, 269(3):187–194, 2018.

[142] Stefano Marchesini, Hari Krishnan, Benedikt J Daurer, David A Shapiro, Talita Perciano, James A Sethian, and Filipe RNC Maia. Sharp: a distributed gpu-based ptychographic solver. Journal of applied crystallography, 49(4):1245–1252, 2016.

[143] Hanfei Yan. Ptychographic phase retrieval by proximal algorithms. New Journal of Physics, 22(2):023035, 2020.

[144] Xiaojing Huang, Hanfei Yan, Ross Harder, Yeukuang Hwu, Ian K Robinson, and Yong S Chu. Optimization of overlap uniformness for ptychography. Optics Express, 22(10):12634–12644, 2014.

[145] AM Maiden, MJ Humphry, MC Sarahan, B Kraus, and JM Rodenburg. An annealing algorithm to correct positioning errors in ptychography. Ultramicroscopy, 120:64–72, 2012.

[146] Fucai Zhang, Isaac Peterson, Joan Vila-Comamala, Ana Diaz, Felisa Berenguer, Richard Bean, Bo Chen, Andreas Menzel, Ian K Robinson, and John M Rodenburg. Translation position determination in ptychographic coherent diffraction imaging. Optics express, 21 (11):13592–13606, 2013.

[147] Philipp M Pelz, Manuel Guizar-Sicairos, Pierre Thibault, Ian Johnson, Mirko Holler, and Andreas Menzel. On-the-fly scans for x-ray ptychography. Applied Physics Letters, 105(25): 251101, 2014.

[148] Xiaojing Huang, Kenneth Lauer, Jesse N Clark, Weihe Xu, Evgeny Nazaretski, Ross Harder, Ian K Robinson, and Yong S Chu. Fly-scan ptychography. Scientific reports, 5:9074, 2015.

[149] Jesse N Clark, Xiaojing Huang, Ross J Harder, and Ian K Robinson. Continuous scanning mode for ptychography. Optics letters, 39(20):6066–6069, 2014.

[150] Michal Odstrčil, Mirko Holler, and Manuel Guizar-Sicairos. Arbitrary-path fly-scan ptychography. Optics express, 26(10):12585–12593, 2018.

[151] Junjing Deng, Curt Preissner, Jeffrey A Klug, Sheikh Mashrafi, Christian Roehrig, Yi Jiang, Yudong Yao, Michael Wojcik, Max D Wyman, David Vine, et al. The velociprobe: An ultrafast hard x-ray nanoprobe for high-resolution ptychographic imaging. Review of Scientific Instruments, 90(8):083701, 2019.

[152] Pavel Sidorenko and Oren Cohen. Single-shot ptychography. Optica, 3(1):9–14, 2016.

[153] Xingchen Pan, Cheng Liu, and Jianqiang Zhu. Single shot ptychographical iterative engine based on multi-beam illumination. Applied Physics Letters, 103(17):171105, 2013.

[154] Haigang Liu, Zijian Xu, Xiangzhi Zhang, Yanqing Wu, Zhi Guo, and Renzhong Tai. Effects of missing low-frequency information on ptychographic and plane-wave coherent diffraction imaging. Applied Optics, 52(11):2416–2427, 2013.

[155] Andrew M Maiden, Martin J Humphry, Fucai Zhang, and John M Rodenburg. Superresolution imaging via ptychography. JOSA A, 28(4):604–612, 2011.

[156] DJ Batey, TB Edo, C Rau, U Wagner, ZD Pešić, TA Waigh, and JM Rodenburg. Reciprocal-space up-sampling from real-space oversampling in x-ray ptychography. Physical Review A, 89(4):043812, 2014.

[157] TB Edo, DJ Batey, AM Maiden, C Rau, U Wagner, ZD Pešić, TA Waigh, and JM Rodenburg. Sampling in x-ray ptychography. Physical Review A, 87(5):053850, 2013.

[158] Martin Dierolf, Pierre Thibault, Andreas Menzel, Cameron M Kewish, Konstantins Jefimovs, Ilme Schlichting, Konstanze Von Koenig, Oliver Bunk, and Franz Pfeiffer. Ptychographic coherent diffractive imaging of weakly scattering specimens. New Journal of Physics, 12(3): 035017, 2010.

[159] Ana Diaz, Pavel Trtik, Manuel Guizar-Sicairos, Andreas Menzel, Pierre Thibault, and Oliver Bunk. Quantitative x-ray phase nanotomography. Physical Review B, 85(2):020104, 2012.

[160] Mirko Holler, Ana Diaz, Manuel Guizar-Sicairos, Petri Karvinen, Elina Färm, Emma Härkönen, Mikko Ritala, Andreas Menzel, Joerg Raabe, and Oliver Bunk. X-ray ptychographic computed tomography at 16 nm isotropic 3d resolution. Scientific reports, 4(1):1–5, 2014.

[161] Andrew M Maiden, Martin J Humphry, and JM Rodenburg. Ptychographic transmission microscopy in three dimensions using a multi-slice approach. JOSA A, 29(8):1606–1614, 2012.

[162] TM Godden, R Suman, MJ Humphry, JM Rodenburg, and AM Maiden. Ptychographic microscope for three-dimensional imaging. Optics express, 22(10):12513–12523, 2014.

[163] Akihiro Suzuki, Shin Furutaku, Kei Shimomura, Kazuto Yamauchi, Yoshiki Kohmura, Tetsuya Ishikawa, and Yukio Takahashi. High-resolution multislice x-ray ptychography of extended thick objects. Physical review letters, 112(5):053903, 2014.

[164] Peng Li and Andrew Maiden. Multi-slice ptychographic tomography. Scientific reports, 8(1): 1–10, 2018.

[165] Kei Shimomura, Makoto Hirose, Takaya Higashino, and Yukio Takahashi. Three-dimensional iterative multislice reconstruction for ptychographic x-ray computed tomography. Optics Express, 26(24):31199–31208, 2018.

[166] Tetsuo Harada, Masato Nakasuji, Yutaka Nagata, Takeo Watanabe, and Hiroo Kinoshita. Phase imaging of extreme-ultraviolet mask using coherent extreme-ultraviolet scatterometry microscope. Japanese Journal of Applied Physics, 52(6S):06GB02, 2013.

[167] JM Rodenburg, AC Hurst, AG Cullis, BR Dobson, F Pfeiffer, O Bunk, C David, K Jefimovs, and I Johnson. Hard-x-ray lensless imaging of extended objects. Physical review letters, 98 (3):034801, 2007.

[168] Darren J Batey, Daniel Claus, and John M Rodenburg. Information multiplexing in ptychography. Ultramicroscopy, 138:13–21, 2014.

[169] Pierre Thibault and Andreas Menzel. Reconstructing state mixtures from diffraction measurements. Nature, 494(7435):68–71, 2013.

[170] Robert Karl, Charles Bevis, Raymond Lopez-Rios, Jonathan Reichanadter, Dennis Gardner, Christina Porter, Elisabeth Shanblatt, Michael Tanksalvala, Giulia F Mancini, Margaret Murnane, et al. Spatial, spectral, and polarization multiplexed ptychography. Optics express, 23(23):30250–30258, 2015.

[171] Bosheng Zhang, Dennis F Gardner, Matthew H Seaberg, Elisabeth R Shanblatt, Christina L Porter, Robert Karl, Christopher A Mancuso, Henry C Kapteyn, Margaret M Murnane, and Daniel E Adams. Ptychographic hyperspectral spectromicroscopy with an extreme ultraviolet high harmonic comb. Optics express, 24(16):18745–18754, 2016.

[172] B Enders, M Dierolf, P Cloetens, M Stockmar, F Pfeiffer, and P Thibault. Ptychography with broad-bandwidth radiation. Applied Physics Letters, 104(17):171104, 2014.

[173] Peter D Baksh, Michal Odstrčil, Hyun-Su Kim, Stuart A Boden, Jeremy G Frey, and William S Brocklesby. Wide-field broadband extreme ultraviolet transmission ptychography using a high-harmonic source. Optics Letters, 41(7):1317–1320, 2016.

[174] Y Esashi, C-T Liao, B Wang, N Brooks, KM Dorney, C Hernández-García, H Kapteyn, D Adams, and M Murnane. Ptychographic amplitude and phase reconstruction of bichromatic vortex beams. Optics Express, 26(26):34007–34015, 2018.

[175] Alexander Björling, Sebastian Kalbfleisch, Maik Kahnt, Simone Sala, Karolis Parfeniukas, Ulrich Vogt, Dina Carbone, and Ulf Johansson. Ptychographic characterization of a coherent nanofocused x-ray beam. Optics Express, 28(4):5069–5076, 2020.

[176] Jesse N Clark, Xiaojing Huang, Ross J Harder, and Ian K Robinson. Dynamic imaging using ptychography. Physical review letters, 112(11):113901, 2014.

[177] Xiaowen Shi, Nicolas Burdet, Darren Batey, and Ian Robinson. Multi-modal ptychography: Recent developments and applications. Applied Sciences, 8(7):1054, 2018.

[178] Jennifer L Ellis, Kevin M Dorney, Daniel D Hickstein, Nathan J Brooks, Christian Gentry, Carlos Hernández-García, Dmitriy Zusin, Justin M Shaw, Quynh L Nguyen, Christopher A Mancuso, et al. High harmonics with spatially varying ellipticity. Optica, 5(4):479–485, 2018.

[179] Juliane Rönsch-Schulenburg, Bart Faatz, Katja Honkavaara, Marion Kuhlmann, Siegfried Schreiber, Rolf Treusch, and Mathias Vogt. Experience with multi-beam and multi-beamline fel-operation. In Proc. 8th Int. Particle Accelerator Conf.(IPAC17), pages 2621–2624, 2017.

[180] Makoto Hirose, Takaya Higashino, Nozomu Ishiguro, and Yukio Takahashi. Multibeam ptychography with synchrotron hard x-rays. Optics Express, 28(2):1216–1224, 2020.

[181] C. S. Bevis, R. Karl, J. Reichanadter, D.F. Gardner, C. Porter, E. Shanblatt, M. Tanksalvala, G.F. Mancini, H. Kapteyn, M. Murnane, and D. Adams. Multiple beam ptychography for large field-of-view, high throughput, quantitative phase contrast imaging. Ultramicroscopy, 184:164–171, 2018. ISSN 18792723. doi: 10.1016/j.ultramic.2017.08.018.

[182] R. M. Karl, D. E. Adams, C. S. Bevis, H. C. Kapteyn, and M. M. Murnane. Coherent diffractive imaging with spaced-apart beams, March 6 2018. US Patent 9,911,207.

[183] R Bates. Fourier phase problems are uniquely solvable in mute than one dimension. i: Underlying theory. Optik, 61(247-262):5, 1982.

[184] Ben Leshem, Rui Xu, Yehonatan Dallal, Jianwei Miao, Boaz Nadler, Dan Oron, Nirit Dudovich, and Oren Raz. Direct single-shot phase retrieval from the diffraction pattern of separated objects. Nature Communications, 7:10820, 2016. doi: 10.1038/ncomms10820. URL http://www.nature.com/doifinder/10.1038/ncomms10820.

[185] Jianwei Miao and David Sayre. On possible extensions of x-ray crystallography through diffraction-pattern oversampling. Acta Crystallographica Section A: Foundations of Crystallography, 56(6):596–605, 2000.

[186] Mark A Robertson, Sean Borman, and Robert L Stevenson. Estimation-theoretic approach to dynamic range enhancement using multiple exposures. Journal of Electronic Imaging, 12 (2):219–229, 2003.

[187] RN Wilke, M Priebe, M Bartels, K Giewekemeyer, A Diaz, P Karvinen, and T Salditt. Hard x-ray imaging of bacterial cells: nano-diffraction and ptychographic reconstruction. Optics express, 20(17):19232–19254, 2012.

[188] Jose A Rodriguez, Rui Xu, C-C Chen, Zhifeng Huang, Huaidong Jiang, Allan L Chen, Kevin S Raines, Alan Pryor Jr, Daewoong Nam, Lutz Wiegart, et al. Three-dimensional coherent x-ray diffractive imaging of whole frozen-hydrated cells. IUCrJ, 2(5):575–583, 2015.

[189] Jose A Dominguez-Caballero, Nick Loomis, George Barbastathis, and Jerry Milgram. Techniques based on digital multiplexing holography for three-dimensional object tracking. In Conference on Lasers and Electro-Optics, page JThD84. Optical Society of America, 2007.

[190] Adam P Hitchcock. Soft x-ray spectromicroscopy and ptychography. Journal of Electron Spectroscopy and Related Phenomena, 200:49–63, 2015.

[191] Jianwei Miao, Tetsuya Ishikawa, Ian K Robinson, and Margaret M Murnane. Beyond crystallography: Diffractive imaging using coherent x-ray light sources. Science, 348(6234):530–535, 2015.

[192] Franz Pfeiffer. X-ray ptychography. Nature Photonics, 12(1):9–17, 2018.

[193] Roger Falcone, Chris Jacobsen, Janos Kirz, Stefano Marchesini, David Shapiro, and John Spence. New directions in x-ray microscopy. Contemporary Physics, 52(4):293–318, 2011.

[194] Martin Dierolf, Andreas Menzel, Pierre Thibault, Philipp Schneider, Cameron M Kewish, Roger Wepf, Oliver Bunk, and Franz Pfeiffer. Ptychographic x-ray computed tomography at the nanoscale. Nature, 467(7314):436–439, 2010.

[195] Junjing Deng, David J Vine, Si Chen, Qiaoling Jin, Youssef SG Nashed, Tom Peterka, Stefan Vogt, and Chris Jacobsen. X-ray ptychographic and fluorescence microscopy of frozen-hydrated cells using continuous scanning. Scientific Reports, 7(1):1–10, 2017.

[196] Junjing Deng, Young Pyo Hong, Si Chen, Youssef SG Nashed, Tom Peterka, Anthony JF Levi, John Damoulakis, Sayan Saha, Travis Eiles, and Chris Jacobsen. Nanoscale x-ray imaging of circuit features without wafer etching. Physical Review B, 95(10):104111, 2017.

[197] Mirko Holler, Manuel Guizar-Sicairos, Esther HR Tsai, Roberto Dinapoli, Elisabeth Müller, Oliver Bunk, Jörg Raabe, and Gabriel Aeppli. High-resolution non-destructive three-dimensional imaging of integrated circuits. Nature, 543(7645):402–406, 2017.

[198] David A Shapiro, Rich Celestre, Peter Denes, Maryam Farmand, John Joseph, ALD Kilcoyne, Stefano Marchesini, Howard Padmore, Singanallur V Venkatakrishnan, Tony Warwick, et al. Ptychographic imaging of nano-materials at the advanced light source with the nanosurveyor instrument. In J. Phys. Conf. Ser, volume 849, page 012028, 2017.

[199] Richard Celestre, Kasra Nowrouzi, David A Shapiro, Peter Denes, John M Joseph, Andreas Schmid, and Howard A Padmore. Nanosurveyor 2: A compact instrument for nanotomography at the advanced light source. In J. Phys. Conf. Ser, volume 849, page 012047, 2017.

[200] Jürgen Thieme, Ian McNult, Stefan Vogt, Paterson, and David. X-ray spectromicroscopya tool for environmental sciences, 2007.

[201] Romy D Hanna and Richard A Ketcham. X-ray computed tomography of planetary materials: A primer and review of recent studies. Geochemistry, 77(4):547–572, 2017.

[202] Yuan Hung Lo, Chen-Ting Liao, Jihan Zhou, Arjun Rana, Charles S Bevis, Guan Gui, Bjoern Enders, Kevin M Cannon, Young-Sang Yu, Richard Celestre, et al. Multimodal x-ray and electron microscopy of the allende meteorite. Science advances, 5(9):eaax3009, 2019.

[203] Roy S Clarke Jr, Eugene Jarosewich, Brian Mason, Joseph Nelen, Manuel Gomez, and Jack R Hyde. Allende, mexico, meteorite shower. Smithsonian Contributions to the Earth Sciences, 1971.

[204] Chi Ma, John R Beckett, and George R Rossman. Allendeite (sc4zr3o12) and hexamolybdenum (mo, ru, fe), two new minerals from an ultrarefractory inclusion from the allende meteorite. American Mineralogist, 99(4):654–666, 2014.

[205] Yuri Amelin and Alexander Krot. Pb isotopic age of the allende chondrules. Meteoritics & Planetary Science, 42(7-8):1321–1335, 2007.

[206] Mirna Lerotic, Rachel Mak, Sue Wirick, Florian Meirer, and Chris Jacobsen. Mantis: a program for the analysis of x-ray spectromicroscopy data. Journal of synchrotron radiation, 21(5):1206–1212, 2014.

[207] JC Sanchez-Lopez, A Caballero, and A Fernandez. Characterisation of passivated aluminium nanopowders: An xps and tem/eels study. Journal of the European Ceramic Society, 18(9): 1195–1200, 1998.

[208] Toshihiro Yoshimura, Yusuke Tamenori, Nozomu Iwasaki, Hiroshi Hasegawa, Atsushi Suzuki, and Hodaka Kawahata. Magnesium k-edge xanes spectroscopy of geological standards. Journal of synchrotron radiation, 20(5):734–740, 2013.

[209] YK Chang, KP Lin, WF Pong, M-H Tsai, HH Hseih, JY Pieh, PK Tseng, JF Lee, and LS Hsu. Charge transfer and hybridization effects in ni 3 al and ni 3 ga studies by x-ray-absorption spectroscopy and theoretical calculations. Journal of Applied Physics, 87(3):1312–1317, 2000.

[210] Binhong He, Minjie Zhou, Zhaohui Hou, Gangyong Li, and Yafei Kuang. Facile synthesis of ni 3 s 2/rgo nanosheets composite on nickel foam as efficient electrocatalyst for hydrogen evolution reaction in alkaline media. Journal of Materials Research, 33(5):519–527, 2018.

[211] Andrew J Westphal, Anna L Butterworth, John A Tomsick, and Zack Gainsforth. Measurement of the oxidation state of fe in the ism using x-ray absorption spectroscopy. The Astrophysical Journal, 872(1):66, 2019.

[212] Stefano Marchesini, Hari Krishnan, Benedikt J Daurer, David A Shapiro, Talita Perciano, James A Sethian, and Filipe RNC Maia. Sharp: a distributed gpu-based ptychographic solver. Journal of applied crystallography, 49(4):1245–1252, 2016.

[213] Heinz H Bauschke, Patrick L Combettes, and D Russell Luke. Hybrid projection–reflection method for phase retrieval. JOSA A, 20(6):1025–1034, 2003.

[214] MWM Jones, AG Peele, and GA van Riessen. Application of a complex constraint for biological samples in coherent diffractive imaging. Optics express, 21(25):30275–30281, 2013.

[215] Jesse N Clark, CT Putkunz, Mark A Pfeifer, AG Peele, GJ Williams, B Chen, Keith Alexander Nugent, C Hall, Wilfred Fullagar, S Kim, et al. Use of a complex constraint in coherent diffractive imaging. Optics Express, 18(3):1981–1993, 2010.

[216] Michael WM Jones, Kirstin Elgass, Mark D Junker, Mac B Luu, Michael T Ryan, Andrew G Peele, and Grant A Van Riessen. Mapping biological composition through quantitative phase and absorption x-ray ptychography. Scientific reports, 4:6796, 2014.

[217] MWM Jones, KD Elgass, MD Junker, MD De Jonge, and GA Van Riessen. Molar concentration from sequential 2-d water-window x-ray ptychography and x-ray fluorescence in hydrated cells. Scientific reports, 6:24280, 2016.

[218] Hanfei Yan, Evgeny Nazaretski, Kenneth Lauer, Xiaojing Huang, Ulrich Wagner, Christoph Rau, Mohammed Yusuf, Ian Robinson, Sebastian Kalbfleisch, Li Li, et al. Multimodality hard-x-ray imaging of a chromosome with nanoscale spatial resolution. Scientific Reports, 6: 20112, 2016.

[219] Hanfei Yan, Yong S Chu, Jörg Maser, Evgeny Nazaretski, Jungdae Kim, Hyon Chol Kang, Jeffrey J Lombardo, and Wilson KS Chiu. Quantitative x-ray phase imaging at the nanoscale by multilayer laue lenses. Scientific reports, 3:1307, 2013.

[220] Franck Bourdelle, Karim Benzerara, Olivier Beyssac, Julie Cosmidis, Daniel R Neuville, Gordon E Brown, and Erwan Paineau. Quantification of the ferric/ferrous iron ratio in silicates by scanning transmission x-ray microscopy at the fe l 2, 3 edges. Contributions to Mineralogy and Petrology, 166(2):423–434, 2013.

[221] Thomas G Sharp and Paul S DeCarli. Shock effects in meteorites. Meteorites and the early solar system II, 943:653–677, 2006.

[222] Dieter Stöffler, Klaus Keil, and Scott Edward RD. Shock metamorphism of ordinary chondrites. Geochimica et Cosmochimica Acta, 55(12):3845–3867, 1991.

[223] JI Goldstein, ERD Scott, and NL Chabot. Iron meteorites: Crystallization, thermal history, parent bodies, and origin. Geochemistry, 69(4):293–325, 2009.

[224] Ursula B Marvin, JA Wood, and JS Dickey Jr. Ca-al rich phases in the allende meteorite. Earth and Planetary Science Letters, 7(4):346–350, 1970.

[225] Lawrence Grossman. Petrography and mineral chemistry of ca-rich inclusions in the allende meteorite. Geochimica et Cosmochimica Acta, 39(4):433–454, 1975.

[226] Chen-Ting Liao, Yuan Hung Lo, Jihan Zhou, Arjun Rana, Charles S Bevis, Guan Gui, Bjoern Enders, Kevin Cannon, David Shapiro, Chris Bennett, et al. Squarrel: Scattering quotient analysis to retrieve the ratio of elements in x-ray ptychography. Microscopy and Microanalysis, 25(S2):112–113, 2019.

[227] Arjun Rana, Jianhua Zhang, Minh Pham, Andrew Yuan, Yuan Hung Lo, Huaidong Jiang, Stanley J Osher, and Jianwei Miao. Potential of attosecond coherent diffractive imaging. Physical Review Letters, 125(8):086101, 2020.

[228] Zhihua Dong, Yao-Lung L Fang, Xiaojing Huang, Hanfei Yan, Sungsoo Ha, Wei Xu, Yong S Chu, Stuart I Campbell, and Meifeng Lin. High-performance multi-mode ptychography reconstruction on distributed gpus. In 2018 New York Scientific Data Summit (NYSDS), pages 1–5. IEEE, 2018.

[229] Saugat Kandel, S Maddali, Marc Allain, Stephan O Hruszkewycz, Chris Jacobsen, and Youssef SG Nashed. Using automatic differentiation as a general framework for ptychographic reconstruction. Optics express, 27(13):18653–18672, 2019.